TÉCNICO LISBOA

Integrated Modeling of the Equilibrium Reconstruction in Tokamaks

Ana Margarida Jorge dos Santos

Thesis to obtain the Master of Science Degree in

Engineering Physics

Supervisor: Prof. Rui Miguel Dias Alves Coelho

Examination Committee

Chairperson: Prof. Luís Paulo Da Mota Capitão Lemos Alves
Supervisor: Prof. Rui Miguel Dias Alves Coelho
Member of the Committee: Prof. Blaise Faugeras

July of 2021

Acknowledgments

I would like to start by thanking my supervisor Prof. Rui Coelho, who was essential to the formulation of the thesis and its methodology. The discussions on the various results in this work, were also very helpful. I would also like to thank the opportunity to work in and learn more about the reconstruction of equilibrium of fusion plasmas.

I would like to acknowledge the valuable contributions from Dr. Wolfgang Zwingmann on the occasional subtle details of the EQUAL code, Dr. Ernesto Lerche on how to set up and run the CYRANO and StixRedist codes, Prof. Thomas Johnsson for providing the HCD workflow, and on useful information regarding Faraday rotation diagnostic at JET exchanged with Dr. Gabor Szepesi. I would finally acknowledge the support from EUROfusion by having access to JET data and to the Gateway and WPCD modeling tools.

Finalmente gostaria de agradecer à minha família e amigos pelo apoio e ajuda durante todo o meu percurso académico.

Resumo

A reconstrução do equilíbrio MHD é fundamental para o estudo de plasmas de fusão. É necessária para a análise de dados de diagnósticos, estudo da estabilidade, transporte, confinamento controlo entre outras. Neste trabalho o equilíbrio de uma descarga do JET aquecida por ICRH e NBI é estudada. O equilíbrio é reconstruído com níveis crescentes de informação usando o código EQUAL. Começando por usar apenas os diagnósticos magnéticos, seguidamente adicionando a pressão térmica, depois a pressão devida a partículas energéticas e finalmente os dados de polarimetria e interferometria. Os resultados são validados com espectroscopia MHD, especificamente com o modo (3,2) de NTM. Este trabalho foi feito dentro da infraestrutura de simulação desenvolvida pela EUROfusion, WPCD. As componentes da pressão das particulas energéticas (deutério e hidrogénio) estão localizadas no core do plasma $\rho_{pol,norm} < 0.45$ e têm valores semelhantes aos da pressão térmica, resultando numa pressão total com um valor máximo (que está deslocado do eixo magnético) à volta de três vezes maior que a pressão térmica. Reconstruir uma descarga com pressões totais tão elevadas é um desafio. A pressão reconstruída é o dobro da térmica, e o mínimo e máximo do fator de segurança e densidade de corrente, respetivamente, estão deslocados do eixo magnético. A adição dos dados de polarimetria e de interferometria melhoram os resultados mas apenas ligeiramente.

Palavras-chave: Tokamak, JET, reconstrução de equilibrio, ICRH, pressão das particulas energéticas,

Abstract

The Reconstruction of MHD equilibrium is fundamental to the understanding of fusion plasma physics. It is necessary for data diagnostic analysis to the study of plasma stability, transport, confinement to the control of the plasma, among others. In this work, the equilibrium of an ICRH and NBI heated JET discharge is studied. The equilibrium is reconstructed with progressively more information using the EQUAL code. Starting by using only magnetic diagnostics, then adding the thermal pressure calculated using the HRTS diagnostic, then the energetic particle pressure components determined numerically using the CYRANO and StixReDist, and finally adding the polarimetry and interferometry diagnostics. The results were validated using the MHD spectroscopy, specifically the (3,2) NTM mode. This was done within the EUROfusion Integrated Modeling framework, WPCD. The energetic particle pressure components (deuterium and hydrogen) were found to be located at the core of the plasma $\rho_{pol,norm} < 0.45$ and to have maximum values similar to the thermal pressure values, so that the total pressure profile has a maximum (which is located at an off-axis position), around three times larger than the thermal pressure. Reconstruction using a discharge with such high total pressures proved to be a challenge. The reconstructed pressure doubled when compared with the thermal pressure, and the maximum and minimum of the safety pressure and toroidal current density were displaced to an off-axis position. The addition of the polarimetry and interferometry diagnostic improves the reconstruction, but only slightly.

Keywords: Tokamak, JET, equilibrium reconstruction, ICRH, energetic particle pressure.

Contents

List of Tables

List of Figures

List of Abbreviations

MHD	Magnetohydrodynamics
D	Deuterium - hydrogen atom with one neutron
T	Tritium - hydrogen atom with two neutrons
p	plasma pressure
ω_c	cyclotron frequency
B	magnetic field
E	Electric field
ϕ	toroidal direction
θ	poloidal direction
J	plasma current density
ψ	magnetic poloidal flux
GSE	Grad-Shafranov equation
q	safety factor
NBI	neutral beam injection
ECRH	electron cyclotron resonance heating
ICRH	ion cyclotron resonance heating
L-mode	low confinement mode
H-mode	high confinement mode
MSE	Motional Stark Effect diagnostic
LiB	lithium beam diagnostic
TS	Thomson Scattering diagnostic
HRTS	High Resolution Thomson Scattering diagnostic
ECE	Electron cyclotron emission diagnostic
CXdiag	Charge exchange diagnostic
WPCD	EUROfusion Project on Code Development for Integrated Modelling
CPO	Consistent Physical objects
UAL	Universal access layer
ITM	integrated tokamak modeling
$\rho_{pol,norm}$	square root of the normalized poloidal magnetic flux
NTM	Neoclassical Tearing mode

Chapter 1

Introduction

1.1 Why nuclear Fusion?

In face of the abounding evidence for climate change and other environmental issues caused by the currently available energy sources, nuclear fusion presents a much-needed solution to the world's energy challenges.

As the standard of living, technology level, and population of the planet increase, so will energy consumption. As can be seen in Figure 1.1, in the last 40 years the world energy consumption doubled and it is expected to increase by 50% in the next 30 years [1] . Ensuring that everyone's energy needs are, and will be met in a sustainable way is an ongoing challenge.

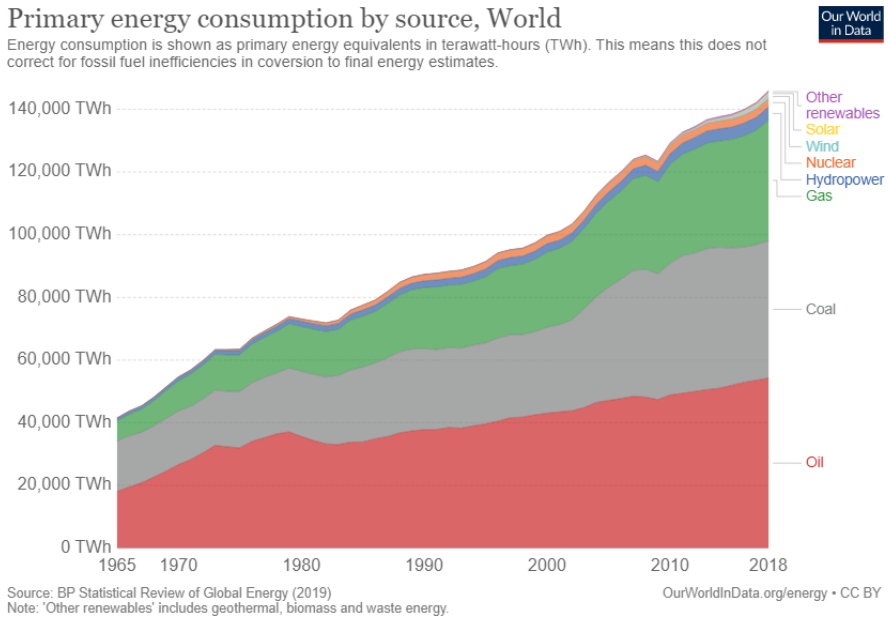

Figure 1.1: Wold primary energy consumption by source [2]

The majority of this energy comes from the burning of fossil fuels (coal, natural gas, and oil). The use of these fuels results in the production of greenhouse gases such as carbon dioxide and other compounds

like nitrogen oxides (NO_x), sulfur dioxide (SO_2), and mercury (Hg) which have negative effects on the environment e.g. acidification of water and soil, and on health e.g. respiratory illnesses.

Alternatives include renewable energies such as solar, hydro, and wind power. However, these are not perfect solutions. Hydropower has environmental consequences such as the emission of greenhouse gases, changes in hydrology and sediment transport, deterioration of water quality, changes in habitats, etc as well as social impacts such as impacts on local communities and cross-border conflicts due to water availability. With wind power, there are environmental impacts as stated in [3]. However, the main problems with the use of wind energy as an alternative to the burning of fossil fuels are wind availability (low speed or unpredictable winds) and energy storage. Solar power has similar problems: the availability (it is not a reliable source of energy in certain weather or climate conditions) and energy storage (since solar energy is intermittent) which reduces its efficiency. The necessity for huge areas when generating solar power on large scales could also be considered a disadvantage.

Nuclear fission has a higher power availability, however, it produces radioactive waste that takes hundreds of years to decay presenting a danger to the environment and, even though the risks of failure are low, their effects are devastating.

Nuclear fusion, as an alternative source for energy production, has many advantages. The fuel is abundant, deuterium occurs naturally in the ocean water and tritium can be produced from lithium (which can be available for 20000 years). Energy production is safe and does not emit harmful substances into the atmosphere. It generates radioactive materials, but those have decays times of a few decades so they would only require 100 years of storage.

1.2 Nuclear Fusion

Nuclear fusion is a reaction in which multiple atomic nuclei with positive charges combine to form a heavier nucleus. Depending on the atomic mass (A) of the reacting nuclei, energy can be released or absorbed. If the atomic masses are smaller than that of iron ($A_{iron} \approx 56$), the binding energy (E_B) of the nuclei before the reaction is bigger than the E_B of the products of the reaction, and thus energy is released, increasing the kinetic energy of the particles. Otherwise, this energy is absorbed, decreasing the kinetic energy of the particles.

The nuclei have positive charges meaning that they repel each other due to Coulomb interaction. In order to get the particles close enough to each other for the reaction to take place, their kinetic energy must be high enough to surpass the repulsion energy. To achieve this, the equivalent gas thermal energy (or temperature) must be high.

The probability of the fusion reaction taking place is proportional to its cross-section (σ). In Figure 1.2, the velocity averaged cross-sections for multiple reactions are shown.

The reaction that requires the least amount of energy and has the highest cross-section is the fusion of deuterium (${}^2_1H$) and tritium (${}^3_1H$), see Equation 1.1. This reaction produces an α particle (${}^4_2He$) and a neutron (n) and $17.6keV$ or $2.8 \times 10^{-12} J$ (a fifth going to the alpha particles and the rest to the neutrons).

This means that for every kilogram of the combined D-T fuel $338 \times 10^6 MJ$ of energy are released [4].

$$D + T \rightarrow \alpha + n + 17.6MeV \tag{1.1}$$

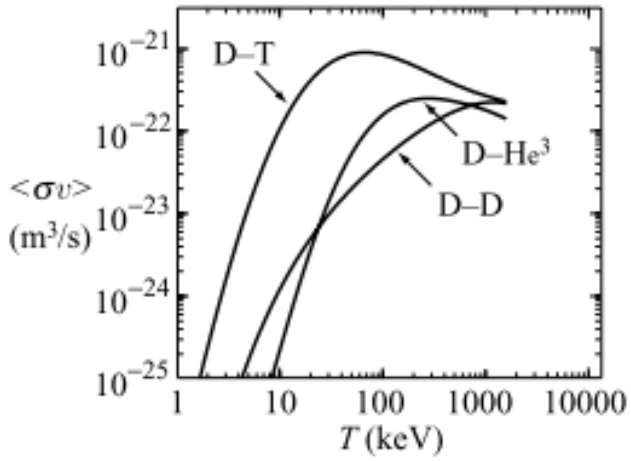

Figure 1.2: Velocity averaged cross-section for the D-T, D-He, and D-D fusion reactions as a function of temperature from [4]

From Figure 1.2, it can be seen that the energies required to initiate fusion reactions are much bigger than the ionization energy ($13.6eV$), so the fuel is a fully ionized gas and it is in the plasma state.

For the alpha power heating to be large enough to balance losses without the need for external power, the operating plasma temperature must be in the order of $15keV$ and the minimum value of $p\tau_E$ must be $8.3atm.s$. Where τ_E is the energy confinement time and p is plasma the pressure, [4].

The ratio between the amount of energy generated by the fusion reactions and the energy supplied is referred to as the energy gain factor, Q. This ratio must be bigger than 1 ($Q > 1$) for the reaction to be economically viable. For the reaction to be self-sustaining, or in other words, for ignition to happen, $Q = \infty$. If the ignition is not possible, additional heating is necessary. Under these more realistic circumstances (finite Q), the confinement time is slightly smaller, thus requiring a hotter core plasma with temperature. The average temperature for ITER is $\sim 11keV$, for DEMO is $\sim 13keV$ and for DEMO2 is $\sim 18keV$ DEMO2 [5].

1.3 How to control Nuclear Fusion

1.3.1 Tokamak

There are three ways to confine the plasma: Gravitational confinement, at play in the sun; Inertial confinement, where the hydrogen gas is compressed by a controlled implosion; and Magnetic confinement, which uses magnetic fields to trap the plasma.

Particles moving in a magnetic field, feel a force perpendicular to it. In a uniform magnetic field, the particles have a helical motion around the field lines with cyclotron frequency $\omega_{ci} = q_i B/m_i$ and radius

$r_{Li} = m_i v_\perp / q_i B$, where B is the magnetic field, q_i is the particle charge, m_i is its mass, and $v_\perp$ is the velocity component perpendicular to the direction of the magnetic field. When using a closed magnetic field configuration, the magnetic field lines form a closed loop (torus), they have a curvature, which leads to a curvature drift ($\mathbf{v}_{curv} = \frac{m}{q}\frac{v_\parallel^2}{R_c^2}\frac{\mathbf{R}_c \times \mathbf{B}}{B^2}$, where $v_\parallel$ is the velocity parallel to the magnetic field and R_c is the radius of curvature). This causes the ions and electrons to drift in opposing directions vertically, and thus creates an electric field. The electric field causes a drift ($\mathbf{v}_E = \frac{\mathbf{E}\times\mathbf{B}}{B^2}$, where $\mathbf{E}$ is the electric field) on both the ions and electrons in the outward direction, therefore there is loss of confinement. To solve the problem, a poloidal field is added to prevent the drift in the vertical direction.

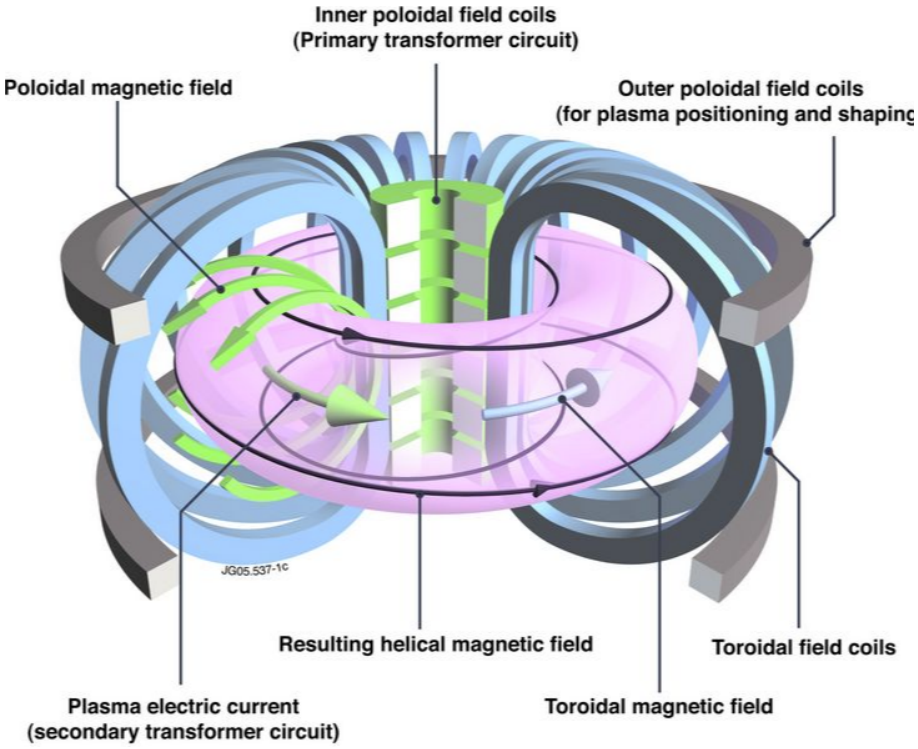

Figure 1.3: Schematic of a tokamak's toroidal and poloidal field coils from [6]

There are several configurations for magnetic confinement, but the one considered the most successful is the tokamak. Tokamak is a toroidal asymmetric structure where plasma is magnetically confined due to the action of magnetic fields, see Figure 1.3. The toroidal plasma current creates the poloidal component of the magnetic field, B_θ. The external toroidal field coils create the toroidal magnetic field, B_ϕ, the $B_\theta << B_\phi$. The magnetic field lines are helices, which rotate slowly in the toroidal direction. There are also extra coils for shaping and positioning the plasma inside the vacuum vessel. The tokamak geometry is shown in Figure 1.4. The ϕ and θ correspond to the toroidal and poloidal directions, respectively. The major radius, R_0, is the distance to the center of the plasma, the minor radius, a, is the radius of the plasma cross-section. The ratio R_0/a is known as the aspect ratio.

1.3.2 Equilibrium

For magnetic confinement fusion to be achieved, it is essential that the whole plasma is kept under force equilibrium. At a fundamental level, this means that the outward expansion force characteristic of a

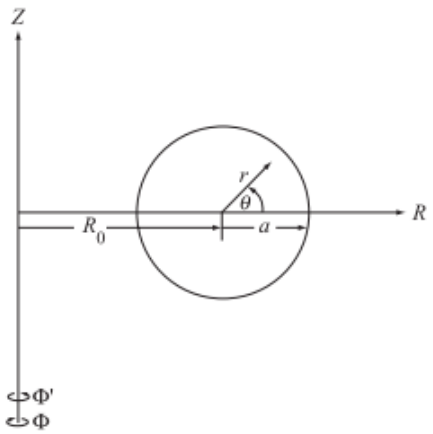

Figure 1.4: Toroidal Geometry [4]

sizable pressure gas (or plasma) needs to be balanced by opposing forces provided for by the magnetic fields.

In order to study the equilibrium, a single-fluid plasma model known as MHD is used. This model describes the plasma macroscopically as one fluid consisting of bulky ions (carrying most of the mass and momentum) and much lighter electrons. The MHD equations can be derived from the two-fluid model [4]. To analyze the equilibrium the following simplifications of the equations are made: In equilibrium, ($\frac{\partial}{\partial t} = 0$) the plasma is assumed to be in steady state; The plasma is assumed to be static ($\mathbf{v} = 0$). The remaining equations are Equations 1.2-1.4. Where μ is the magnetic permeability, $\mathbf{J}$ is the current density, $\mathbf{B}$ is the magnetic field and p is the plasma pressure. Equation 1.2 shows the required balance between the magnetic force and the force due to the plasma pressure.

$$\mathbf{J} \times \mathbf{B} = \nabla p \tag{1.2}$$

$$\nabla.\mathbf{B} = 0 \tag{1.3}$$

$$\nabla \times \mathbf{B} = \mu \mathbf{J} \tag{1.4}$$

From these equations, the existence of so-called magnetic flux surfaces can be derived. In a confined plasma, the pressure contours form closed, nested, toroidal surfaces, see Figure 1.5.

By making the dot product of $\mathbf{B}$ with Equation 1.2, we get $\mathbf{B}.\nabla p = 0$. So the magnetic field lines lie on surfaces with constant pressure (there is no component of $\mathbf{B}$ perpendicular to the surface).

Proceeding in the same manner for the $\mathbf{J}$, we get $\mathbf{J}.\nabla p = 0$, so the current density also lies on the surfaces with constant pressure. The current density and magnetic field are not parallel to each other though, otherwise, the pressure gradient would not be balanced (see Equation 1.2), the plasma cannot be a force-free medium (i.e plasma pressure considered to be small enough, that when compared to the magnetic pressure, it could be neglected).

These surfaces with constant pressure and in which the magnetic field and current density lines lie are called flux surfaces. The poloidal magnetic flux $\psi(R, Z)$ is defined by the flux of the poloidal component

of the magnetic field across a disk-like surface with constant Z bounded by a ring passing through a point $P(R, Z)$, as in Equation 1.5. So that the magnetic field can be described by Equations 1.6 and 1.7. Thus it can concluded that $\mathbf{B}.\nabla\psi = (-\frac{1}{R}\frac{\partial\psi}{\partial Z}, \frac{F}{R}, \frac{1}{R}\frac{\partial\psi}{\partial R}).(\frac{\partial\psi}{R}, 0, \frac{\partial\psi}{\partial Z}) = 0$, the surfaces have constant poloidal magnetic flux, hence their name.

$$\psi(R, Z) = \frac{1}{2\pi}\int_S \mathbf{B}.dS \tag{1.5}$$

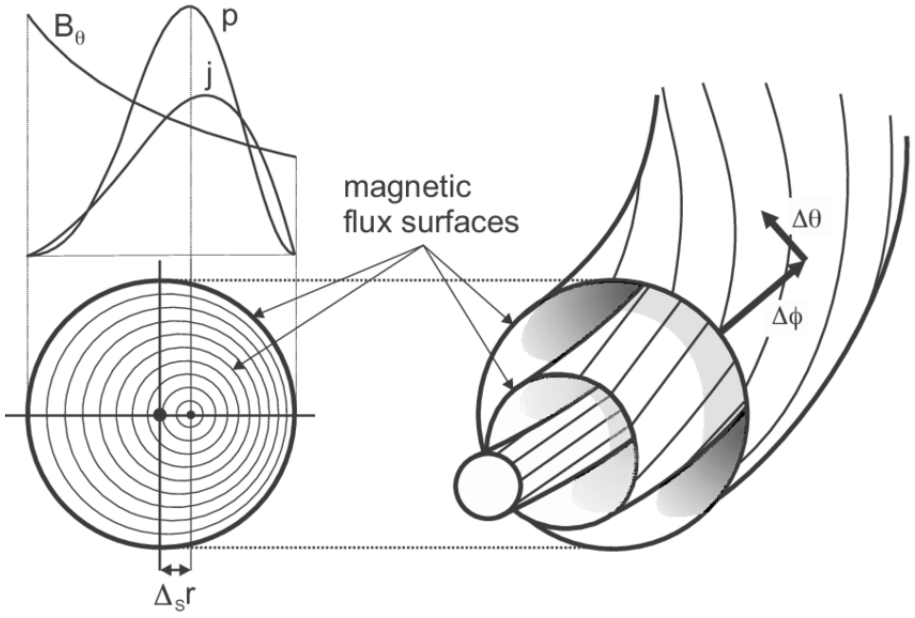

Figure 1.5: Closed nested toroidal surfaces, along with pressure and current profiles and Shafranov shift from [7]

Grad-Shafranov Equation

From the Maxwell and MHD equations, one can derive the Grad-Shafranov Equation 1.11 [8]. Since the tokamak is axially symmetric, in the cylindrical coordinate system (R, ϕ, Z), $\mathbf{B}$ is independent of the ϕ. $\mathbf{B}$ can be written as:

$$\mathbf{B}_\theta = \frac{1}{R}[\nabla\psi \times \mathbf{e}_\phi] \tag{1.6}$$

$$\mathbf{B}_\phi = \frac{F}{R}\mathbf{e}_\phi \tag{1.7}$$

From the Maxwell's equations and $\mathbf{B}$, the expression for the current density can be obtained:

$$\mu\mathbf{J}_\theta = \frac{1}{R}\nabla(F) \times \mathbf{e}_\phi \tag{1.8}$$

$$\mu\mathbf{J}_\phi = -\left(\frac{\partial}{\partial R}\left(\frac{1}{R}\frac{\partial\psi}{\partial R}\right) - \frac{\partial}{\partial Z}\left(\frac{1}{R}\frac{\partial\psi}{\partial Z}\right)\right)\mathbf{e}_\phi = \frac{\Delta^*\psi}{R}\mathbf{e}_\phi \tag{1.9}$$

By replacing Equations 1.6, 1.7, and 1.9 in Equation 1.2, it can be written as:

$$\nabla p = (\Delta^* \psi)\nabla\psi - \frac{F}{\mu R^2}\nabla F \tag{1.10}$$

Since $\psi(R, Z) = constant$ in the flux surfaces, ∇p is perpendicular to $\mathbf{B}$ and $\mathbf{J}$, and ∇p is collinear to $\nabla\psi$ and ∇F we can conclude that $p = p(\psi)$ and $F = F(\psi)$. So the Grad-Shafranov equation can be written:

$$\Delta^* \psi = -\mu_0 R^2 \frac{dp}{d\psi} - F\frac{dF}{d\psi} = -\mu_0 R J_\phi \quad , \quad \Delta^* \psi = \frac{\partial^2 \psi}{\partial Z^2} + R\frac{\partial}{\partial R}\left(\frac{1}{R}\frac{\partial \psi}{\partial R}\right) \tag{1.11}$$

One should note that Equation 1.11 is strictly valid in the plasma domain. It can, however, be generalized to the whole domain of the tokamak including the vacuum region, surrounding the plasma, enclosing the poloidal field coils responsible for plasma positioning and shaping:

$$\Delta^* \psi = \begin{cases} -\mu_0 R J_\phi & \text{in the plasma} \\ -\mu_0 R J_{\phi,ext} & \text{in the external conductors} \\ \Gamma_\mu & \text{in the ferromagnetic materials} \\ 0 & \text{in vacuum} \end{cases}$$

Safety factor

The safety factor, q, has this name because of its role in the determination of stability. Each magnetic field line has a value of q given by Equation 1.12, where $\Delta\phi$ is the change in toroidal angle that the helical magnetic field line takes to be in the same position in the poloidal plane, see Figure 1.6. The $\Delta\theta$ is the difference in the poloidal angle of the magnetic field line after one toroidal rotation.

$$q = \frac{\Delta\phi}{2\pi} = \frac{2\pi}{\Delta\theta} \approx \frac{rB_\phi}{R_0 B_\theta}, \quad \text{if } \frac{R_0}{a} \text{ is large} \tag{1.12}$$

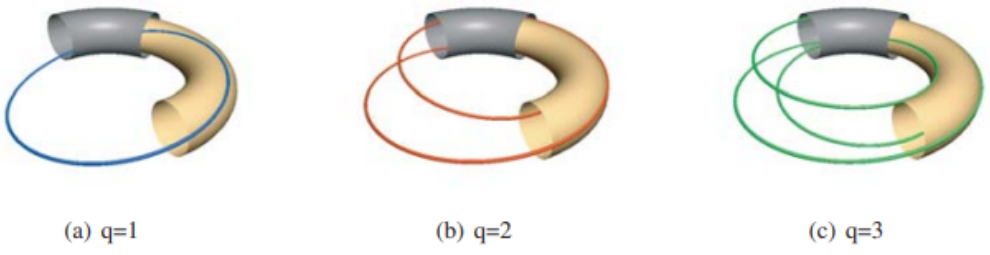

(a) q=1 (b) q=2 (c) q=3

Figure 1.6: Graph of field lines and their respective safety factor values from [7]

Shafranov Shift

Is the outward radial displacement, $\Delta(R)$, of the magnetic flux surfaces centers. This shift depends on the pressure profiles and poloidal magnetic fields as in [9], see Figure 1.5. Intuitively, the Shafranov shift is an indication of the sizable pressure competing with the magnetic field particularly relevant in the high pressure/temperature core of the plasma.

1.3.3 Heating

The toroidal current is a source of plasma heating due to the resistance of the plasma to the current. However, this resistivity η decreases with temperature $\eta \sim T^{-3/2}$, so, as the temperature increases the heating efficiency decreases. The maximum temperature that can be obtained with ohmic heating is approximately $3keV$ [4], not enough for the alpha heating to compensate for the losses. Therefore, external forms of heating are necessary such as neutral beam injection and radiofrequency heating.

With neutral beam injection heating (NBI), a high-energy beam of neutral particles (deuterium or tritium atoms) is injected into the plasma. Since these particles are neutral (not affected by the magnetic fields) they move in a straight line until they are ionized by collisions with the background plasma. This allows them to penetrate to the center of the plasma. The ions are trapped by the magnetic field and their energy is transferred to the rest of the plasma by Coulomb collisions. How much energy is transferred and how much the neutral atoms penetrate the plasma depends on the initial energy of the beam and the injection geometry.

With radio-frequency heating, electromagnetic waves are launched into the plasma from an external antenna. When the frequency of these waves matches the plasma wave frequencies, there is a strong absorption of energy. The frequencies of interest are the ion and electron cyclotron frequencies as well as their harmonics. If the frequencies are the electron's cyclotron frequencies the heating is known as the electron cyclotron resonance heating (ECRH). If they are the ions', it is called ion cyclotron resonance heating (ICRH).

ICRH for the deuterium ions has a weak absorption due to the polarization of the wave at the resonance point. To solve this problem, minority heating is used. This means that a small population of either hydrogen or helium is added to the plasma (which have cyclotron frequencies higher than that of deuterium). This solves the problem since the polarization is determined by the majority species.

1.3.4 Current Drive

The toroidal current can be driven by inductive and non-inductive methods.

With the inductive method, the toroidal current is driven by a transformer that has the plasma as its secondary winding. A varying current in the primary winding of the transformer creates a varying magnetic flux in the secondary winding inducing a toroidal electric field, and so the toroidal current. This means that the tokamak would work as a pulsed device.

To operate a tokamak in steady state, part of the toroidal current must be driven with non-inductive methods like neutral beam injection, electron cyclotron waves, fast waves, and lower hybrid waves. In

addition, another non-inductive current contribution worth mentioning is self-generated by the plasma itself and is named bootstrap current (driven by the plasma pressure gradient and by plasma collisionality) [9].

1.3.5 Energetic particles

Energetic particles generally designate ions with energies, that exceed by far, the thermal energy of the bulk ions. These particles are typically generated in the plasma core (where density and temperature are highest thus where fusion reactions are favored) or where the external heating and current drive methods deposit most of the power. It may depend on the resonance frequency (ICRH) or the tangency radius of the injected beams and plasma density (NBI). Since the energetic ions do not have Maxwellian distributions, kinetic theory is used (the population is described by a density function in space, velocity, and time).

1.3.6 MHD Stability

In studying the stability problem, we aim to see whether a plasma that has been perturbed away from the equilibrium will return to its original position as time progresses (if it is stable) or not (if it is unstable).

Instabilities can be classified into internal or external modes (whether or not they affect the boundary), into pressure or current-driven modes, and ideal or resistive modes (electrical plasma resistivity being zero or non zero).

In a tokamak, plasma instabilities may also have quite a diverse location in the plasma (where the perturbation is largest) and with characteristic length scale (or periodicity) in the poloidal and toroidal direction. It is indeed customary to decompose the mode's structure in Fourier components of the form $exp[i(m\theta - n\phi)]$, m and n being the poloidal and toroidal mode numbers respectively.

MHD modes can be stabilized if the mode characteristics involve bending and compressing the magnetic field lines since this naturally involves spending energy that would otherwise be available for the mode to grow. Since in the surface corresponding to $q = m/n$, there is a resonance for the instability characterized by the m and n mode numbers (the stabilizing effected is minimized), for an (m, n) instability to exist a surface with safety factor equal to $q = m/n$ must exist in the plasma or very close to the plasma boundary in case of external modes. Seeing that the modes with higher values of the poloidal mode number m have a stronger stabilizing effect, in ideal terms, the best plasma stability should come from shaping the q, so that the q values corresponding to low m/n modes are excluded. Unfortunately, having an "elevated" q-profile is not the best option in terms of confinement time, and as such a compromise has to be considered, eventually adopting some feedback control techniques on the most detrimental modes [9].

Some modes will be relevant when looking at the data used in this thesis, such as neoclassical tearing modes (NTMs), Toroidal Alfvén Eigenmode (TAEs), and sawteeth instability.

The sawteeth instability owes its name to the characteristic sawtooth wave-like pattern observed in the core plasma temperature [10]. The eigenmode associated with this instability is believed to be the

ideal ($m = 1, n = 1$) kink mode resonant with the $q = 1/1$ magnetic flux surface. During the very fast event named *sawtooth crash*, the central plasma temperature (but also density) suffers a minor collapse with redistribution of particles and heat towards outward regions (thus showing slight and temporary increases in temperature). The crash, quite violent but still mostly localized in the plasma core, may also trigger the onset of other plasma instabilities such as NTMs.

NTMs are a particular type of resistive instability that occurs for usually low toroidal/poloidal mode numbers e.g. ($m = 2, n = 1$) or ($m = 3, n = 2$) and that is associated to the reconnection of magnetic field lines around the resonant $q = m/n$ magnetic surface, resulting in potentially large magnetic islands that may reach 10% of the minor plasma radius [11]. Usually driven by plasma current density, they can also be driven unstable by the loss of bootstrap current inside the magnetic island, triggered by other events e.g. sawtooth crashes. The onset and growth of such modes is almost always harmful to the plasma confinement e.g. in setting plasma beta (defined as the ratio between the plasma and magnetic pressures) limits in the plasma core for the case of large ($m = 3, n = 2$) or even to the mode-locking and plasma disruption for the case of ($m = 2, n = 1$) modes closer to the plasma boundary [12].

TAEs are a particular case of plasma Alfvén waves which are modes located in the so-called frequency gaps of the shear Alfvén continuum spectrum, owing to the toroidal plasma geometry of the plasma and the non-circular plasma cross-sectional shape. These modes may be destabilized when energetic particles (that can come from the heating schemes, NBI ICRH, ECRH,... or the fusion reactions themselves in the case of alpha particles) with velocities comparable or larger than the plasma Alfvén speed resonate with the modes and transfer to it part of their energy [13]. Eventually, the sustained growth and saturation in amplitude of these Alfvén Eigenmodes leads to a net loss of the energy that would be otherwise transferred to the plasma (reducing the heating efficiency) and even to the loss of confinement of energetic particles.

1.3.7 Transport and Modes of Confinement

As stated before, to achieve fusion, the ions need to be confined for a sufficient amount of time. Transport theory aims to understand and in doing so, control, energy confinement. There are three main types of transport in plasmas: heat conduction, particle diffusion, and magnetic field diffusion.

However, experimental confinement time does not agree with the calculated values, in either the order of magnitude or the scaling relations. It can be up to two orders of magnitude larger [9]. These anomalous values for the transport are due to the presence of turbulence due to micro-instabilities.

So in order to understand the transport, empirical methods are used, such as using stochastic methods to determine the dependence of the confinement time on the plasma parameters such as the temperature (T), magnetic field (B), density (n), minor radius (a), the atomic mass of the plasma ions (A), elongation (k), safety factor (q) and the inverse aspect ratio (ϵ) [4]. The resulting relations can be used to extrapolate for other Tokamaks.

The confinement behavior can be classified into various categories, such as: Ohmically heated plasma's, Low confinement mode (L-mode), High confinement mode (H-mode), Advanced Tokamak.

Ohmically heated plasma

The energy confinement time scaled as Equation 1.13. This value saturates at a density given by Equation 1.14, [9].

$$\tau_E = 0.07 \left(\frac{n}{10^{20}}\right) a^3 \epsilon^{-2} qs \tag{1.13}$$

$$n_{sat} = 0.06 \times 10^{20} I A^{0.5} k^{-1} a^{-1.5} \epsilon^{-1} \tag{1.14}$$

L-mode

To improve the confinement additional heating is applied as described in section 1.3.3. In this mode, it was found that the confinement time decreases with the increased heating power [9]. The energy confinement time scales as:

$$\tau_{EL} = 0.048 \frac{I^{0.85} a^{1.5} \epsilon^{-1.2} k^{0.5} (n/10^{20})^{0.1} B^{0.2} A^{0.5}}{P^{0.5}} \tag{1.15}$$

The L-mode has a pressure profile that decays at a smooth rate towards the plasma edge, see Figure 1.7.

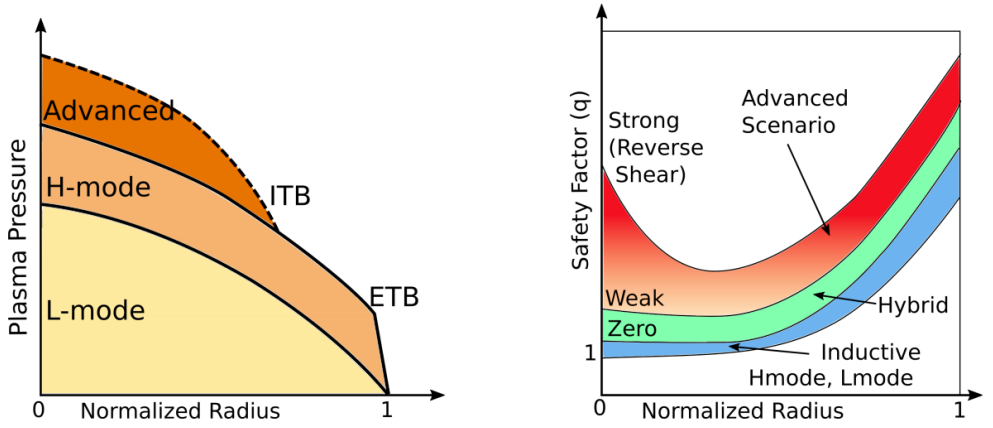

(a) Confinement modes characterized by pressure profile.

(b) Operating scenarios characterized by q profile.

Figure 1.7: Tokamak confinement modes, from [14]

H-mode

The H-mode was discovered in the ASDEX tokamak. This mode provides a confinement time twice as large as the L-mode. To obtain this mode, sufficient external power must be applied as described in Section 1.3.3, allowing for the appearance of an edge transport barrier. The pressure profile is characterized by a steep gradient at the edge of the plasma, see Figure 1.7. In this mode, the confinement is improved, typically, by a factor of 2 [9]

The transition is more easily obtained with the divertor configuration as opposed to the limiter

configuration, see Figure 1.8. The energy confinement time scales as:

$$\tau_{EH} = 0.053 \frac{I^{1.06} a^{1.79} \epsilon^{-1.9} k^{0.66} (n/10^{20})^{0.17} B^{0.32} A^{0.41}}{P^{0.67}} \tag{1.16}$$

Advanced Tokamak

This corresponds to modes of operation where the profiles are controlled by the external power supply. The goal is to achieve a hollow current profile, by increasing the non-inductive off-axis current. The corresponding safety factor profiles are non-monotonic with an off-axis minimum, called reversed shear profile, see Figure 1.7. This is related to a strong pressure gradient in the core. In this scenario, the confinement can be improved by a factor of around 3 (when compared with the L-mode) [9].

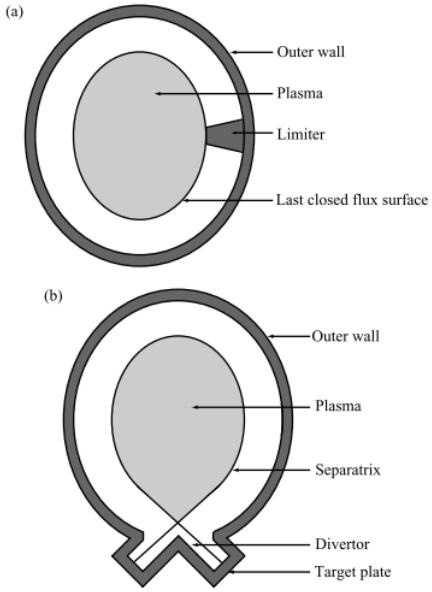

Figure 1.8: Schematic of a limiter (a) and a divertor (b), from [4]

1.3.8 Diagnostics

For the purposes of this thesis, the most relevant diagnostics that are typically installed in many of the running Tokamaks can be subdivided into these three categories: magnetic, current, and kinetic. A brief description of these types of diagnostics along with their contributions when used in equilibrium reconstruction are presented below.

Magnetic Diagnostics

Magnetic diagnostics include magnetic coils and probes, flux loops, saddle loops, and Rogowski coils [15]. These diagnostics measure the total plasma current I_p, the magnetic field, and poloidal flux.

Magnetic coils or probes work in the following manner: assuming the uniform magnetic field over the sensor's area, varying in time, the voltage induced in the coil is $V \propto \dot{B}$, where B is the magnetic field perpendicular to the coil. Since the aim is to know B, integration of V is done, so that $V = c_1 B$, where

c_1 depends on the coil.

The flux loop is made of one loop of wire and is placed outside the vacuum vessel in the toroidal direction. The integrated voltage gives the poloidal magnetic flux through the loop.

Saddle loops are made by connecting two different parts of the flux loops, by integration of the voltage, the poloidal flux difference between two (R, Z) points can be measured.

The voltage out of the Rogowski coil is given by $V = \Phi = nA\mu\dot{I}$, this measurement is integrated in order to have a quantity proportional to I. This measurement is prone to errors. Another method used to calculate the current is the integration of the poloidal magnetic field deduced by each magnetic sensor along a poloidal path in the same toroidal angle to approximate the integral $I = (1/\mu_0) \oint \mathbf{B}.\mathbf{dl}$, where I is the current passing through the surface defined by the closed path of the integral [9].

When the measurements from these diagnostics are used in the equilibrium Reconstruction, the total plasma current, plasma shape, internal inductance ($l_i = \int_\Omega dV B_p^2/(B_{pa}^2\Omega)$), the poloidal plasma beta ($\beta_p = 2\mu_0 \int_\Omega dVp/(B_{pa}^2\Omega)$) and edge current profile can be determined [16, 17], where Ω is the plasma volume, $B_{pa} = \mu_0 I_p/\int_\Gamma dl$ is the average poloidal magnetic field for normalization and Γ is the plasma surface corresponding to Ω.

Current Diagnostics

Current diagnostics consist of Motional Stark effect (MSE), Li Beam (LiB), polarimetry, etc.

LiB utilizes Zeeman splitting of radiation from injected Lithium atoms. In the presence of a magnetic field, the spectral line emission is shifted and split. Since the energy shift of each level is proportional to the magnetic field: $\Delta\lambda_B = \Delta m(\mu/hc)\lambda_0^2 B$, [18], it is possible to get information on the magnetic field.

MSE gives information on the magnetic field distribution. Neutral beam injection is used. As the beam goes through the magnetic field at high velocity, it experiences an electric field $\mathbf{E} = \mathbf{v} \times \mathbf{B}$, where $\mathbf{v}$ is the velocity of the neutral atoms and $\mathbf{B}$ is the background magnetic field. The Stark effect generated by the electric field causes splitting of the radiation emitted by the atoms when excited by collisions with the background plasma, into nine spectral lines. The polarization of the light has the same direction of the magnetic field, so measuring the polarization angle allows the determination of the magnetic field direction, the wavelength splitting has information about the magnetic field magnitude. [19].

Polarimetry measures the polarization shift or Faraday rotation angle of a laser beam (also used for interferometry measurements - see Kinetic Diagnostics in subsection 1.3.8). The shift is proportional to the integral of $n\mathbf{B}$ through the chord of the diagnostic where n is the local plasma density. Various chords are used in the poloidal plane with different paths [20].

These add the internal magnetic field, flux surfaces, and current density information as constraints and allow for the determination of the magnetic surface, current profile, and safety factor profile, [16].

Kinetic Diagnostics

Kinetic diagnostics consist of Thomson scattering (TS), electron cyclotron emission (ECE), charge exchange diagnostic (CXdiag), x-ray crystal spectrometer (XCS), interferometry, etc.

TS is based on the scattering of electromagnetic radiation (laser) from free electrons present in the plasma. Due to the Doppler effect, there is a broadening of the scattered spectrum. The electron thermal temperature is determined from the spectral width of the Thomson scattered signal. The electron density is determined from the signal intensity (or the number of scattered photons) [21].

CXdiag measures the ion temperatures by measuring the frequency broadening of the light emitted by ions when they capture electrons from a neutral beam [22].

ECE power received by an antenna is proportional to the electron temperature. The motion of the electrons in a magnetized plasma leads to the emission of radiation with electron cyclotron frequency and its harmonics. The cyclotron frequency depends on the magnetic field therefore, the position of the measurement can be determined once the magnetic field distribution in (R, Z) is known [23].

Interferometry measures the integrated electron density by comparing the phase of the light from a laser that goes through the plasma with the one that does not. This phase shift is proportional to the integrated density along the path of the laser [20].

When combined, the use of the plasma density and temperature may be used as a constraint when calculating (reconstructing) the plasma equilibrium. They allow for a better determination of the pressure profile particularly the pedestal region [16]. Since precise measurements of the distribution of energetic particles (not Maxwellian) are not directly available, it is necessary to use numerical models to get that information.

1.4 State of the Art

As stated previously, research of fusion plasmas in Tokamaks is important since it presents a great solution for the world's energy challenges.

Most of the research topics, such as tokamak data analysis, study of stability confinement and transport, simulation and modeling, and plasma control require equilibrium reconstruction. Direct, free-boundary equilibrium reconstruction codes determine the topology/spatial distribution of the magnetic fields (or magnetic flux surfaces) and the pressure, toroidal current density profiles.

This section presents a description of the types of equilibrium codes, a description of the equilibrium reconstruction algorithm and some of the existing codes, and a summary of the evolution of the reconstruction codes. It also presents a small description of the calculation of the energetic particle pressure and some of the integrated modeling infrastructures.

1.4.1 How the direct equilibrium reconstruction codes work

The Grad-Shafranov equation (see Equation 1.11) is numerically solved, and the least square error function, which compares the results with the diagnostic data, (χ^2) is minimized in order to determine the topology/spatial distribution of the magnetic field or magnetic flux surfaces, pressure, toroidal density current, and F function profiles.

To reconstruct the flux surfaces, using the Green's function method, the solution to GSE (Equation

1.11) can be written as [17]:

$$\psi(\vec{r}) = \int J_\phi[R', \psi(\vec{r'})] G(\vec{r}, \vec{r'}) dR' dZ', \quad J_\phi = RP'(\psi) + \frac{\mu_0 FF'(\psi)}{4\pi^2 R}, \quad r = (R, Z) \tag{1.17}$$

Where $G(\vec{r}, \vec{r'})$ is the green function, which depends only on the geometry of the tokamak, and it's pre-computed. The p' and FF' functions are represented using a set of basic functions y_n (Equation 1.18), which can be can be polynomials, variable tension splines, ... where x is the normalized poloidal magnetic flux, ψ_0 is the poloidal magnetic flux at the magnetic axis and ψ_1 is the poloidal magnetic flux at the plasma boundary, α_n and γ_n are unknown parameters.

$$\frac{dp}{d\psi} = \sum_n \alpha_n y_n(x) \quad , \quad F\frac{dF}{d\psi} = \sum_n \gamma_n y_n(x) \quad , \quad x = \frac{\psi - \psi_0}{\psi_1 - \psi_0} \tag{1.18}$$

Then the simulated magnetic measurements (C_i) are calculated as described in Equation 1.19. Where m is the number of the iteration, i is the number of the magnetic measurement, $\bar{\alpha}$ is the vector with the parameters of the p' and FF' functions (α_n and γ_n) and I_{ej} is the total current in the j external coil located at $\bar{r}_{ej}$.

$$C_i^{m+1}(r_i) = \sum_j G_{C_i}(r_i, r_{ej}) I_{ej} + \int_{\Omega^m} dR' dZ' G_{C_i}(r_i, r') J_\phi \left[R', \psi^m(r'), \bar{\alpha}^{m+1}\right] \tag{1.19}$$

The unknown parameters are then determined by minimizing the expression in Equation 1.20, where M_i are the available magnetic diagnostic data and σ_i is the uncertainty of those measurements.

$$\chi^2 = \Sigma_i \left(\frac{M_i - C_i}{\sigma_i}\right)^2 \tag{1.20}$$

In order to use the kinetic diagnostics in the reconstruction, the pressure calculated with: $P(\psi) = n_e(\psi)T_e(\psi) + [n_i(\psi) + n_z(\psi)]T_i(\psi) + P_f$, where n_e, n_i and n_z are the electron, ion, and impurity densities, T_e and T_i are the electron and ion temperatures and P_f is the pressure due to the energetic ions. The impurity temperature is assumed to be the same as the ion temperature. The plasma temperature and density are considered constant in the flux surfaces. The value for the pressure due to energetic ions, P_f, is computed analytically as the sum of the pressure due to the various methods for external heating and current drive, with codes described in section 1.4.4 and the values for T_e, T_i, n_e, n_z come from diagnostics described in section 1.3.8, the values of n_i is determined by knowing n_e and n_z and from the quasi-neutrality condition.

The calculated pressure can be added as a constrain by adding a term to Equation 1.20 that compares the calculated pressure from the data and numerical codes with the pressure from the reconstruction.

To calculate the pressure (a flux function) the temperatures and densities need to be in function of the magnetic flux (in general the diagnostic data comes in function of R and Z), therefore the following steps are used:

1. From the external magnetic data the flux surfaces $\psi(\vec{r})$ are reconstructed

2. The data for n_e, n_z, T_e and T_i is mapped in those flux surfaces

3. Using that data, the pressure is calculated.

4. A new poloidal flux surface is reconstructed

5. Go to the second step, until the flux surfaces converge to a predefined tolerance

The current diagnostics and the corresponding reconstructed measurements can also be added to Equation 1.20.

1.4.2 Equilibrium Codes

Free boundary equilibrium codes include the EFIT code [17], the EQUAL code [24], the CLISTE[25], the EQUINOX [26], CEDRES++ [27], NICE [28], XLOC [29]...

EFIT was developed in the 80s to analyze the data of D-III tokamak using only the external magnetic measurements to solve the GSE equation and has since been expanded to use internal current profiles from MSE and pressure profiles from kinetic diagnostics and numerical codes to compute pressure component due to energetic ions. It uses polynomial or variable tension splines as basis functions. It was also expanded to take into account plasma rotation and the iron core of some Tokamaks e.g. JET.

EQUAL is an equilibrium reconstruction code based on the algorithm of EFIT, developed within the European Task Force on Integrated Tokamak Modeling (ITM-TF) [30]. It solves the GS Equation 1.11, with an extra term for the current distribution sources outside the plasma. It uses magnetic, MSE and Faraday diagnostics. It uses either polynomials or B-splines as the basis functions. EQUAL can also adequately describe the effect of the iron core (in the case it exists). The unknown coefficients of the parameterization are determined by minimizing an expression similar to Equation 1.20 with an additional regularization term $\lambda^2 R(\bar{\alpha})$, to control nonphysical oscillations.

CLISTE is an equilibrium code, used for full equilibrium reconstruction between discharges. This code features the natural presence of the scrape-off layer currents in the equilibrium solution, by decoupling the last current-carrying flux surface from the plasma boundary surface. However, since CLISTE was developed originally for ASDEX Tokamak (an air-core Tokamak like ITER), it cannot handle iron core effects.

XLOC is a boundary reconstruction code used at JET to get plasma position and for current control. It determines the shape of the boundary by extrapolating from the magnetic field in the vacuum. It makes a reconstruction every 2 ms.

EQUINOX is a real-time reconstruction code. Finds the functions of p', ff', and n_e that minimize the sum of the differences between the poloidal magnetic field, the measurements from Faraday rotation, and the line integrated density and the ones calculated using the ψ from GSE and the n_e function, and a Tikhonov regularization term. It uses XLOC to get the boundary condition.

Fixed boundary codes include CHEASE [31], HELENA [32],...

To improve the equilibrium without the use of smoothness constraints, [33] proposes a coupling scheme of a GS equation solver with the results of the current diffusion equation. The CDE predicatively models

the current profiles to use in the next equilibrium reconstruction and the inverse GSE solver minimized the least-square criterion on the measured and modeled data.

The Minerva framework uses the concept of Bayesian graphical models, to model the full set of dependencies, functional and probabilistic, between physics assumptions and diagnostic raw data to yield predictions on the internal plasma state including magnetic topology [34], instead of solving the GSE equation.

1.4.3 Evolution of Reconstruction Codes

This section in based on [17], [35] and [36], see Figure 1.9.

From 1980 to 1982 a code was set up to reconstruct the flux surface using data from the pick-up coils [37]. The first equilibrium reconstruction codes were made to analyze data from D-III tokamak using external magnetic data in 1982. With these codes and external data, the plasma shape, stored energy, and the peaking current profile could be determined [38].

MFIT and EFIT [39], were developed in the early 80s. MFIT uses filament currents to model the plasma current profile, it is very computational inexpensive but it is not very accurate when describing flux surfaces. EFIT is still computationally efficient because it uses the filament approach but it interleaves the fitting and equilibrium iterations to find the optimum solution. The accuracy is improved because it allows the distributed plasma current to be constrained by the MHD equilibrium.

To fully reconstruct the pressure and current profiles as well as the associated magnetic topology self-consistently, current and kinetic diagnostics must be used with the magnetic ones. The first kinetic codes were developed in the late 80s.

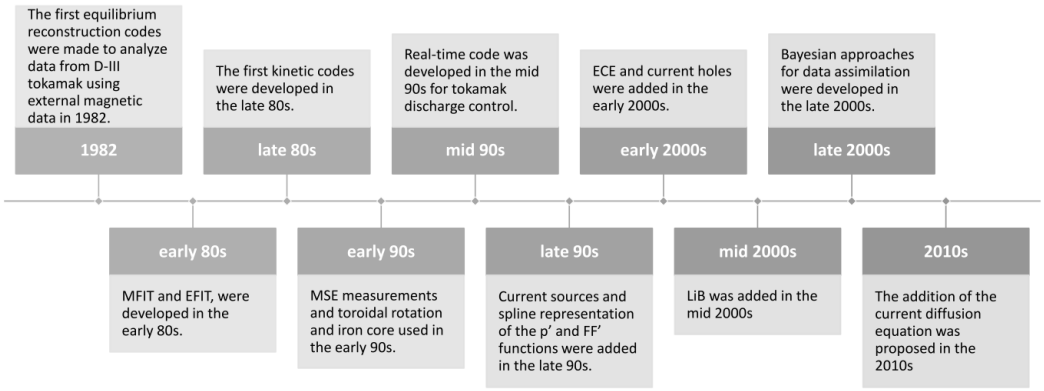

Figure 1.9: Evolution of reconstruction codes

In the early 90s, motional stark effect (MSE) was used along with external magnetic measurements by the EFIT code [40]. The first equilibrium reconstructions taking toroidal rotation into account were also made in the early 90s using information on the plasma mass density and toroidal rotation profile, along with other data. Then a full domain method for plasma equilibrium reconstruction in an iron core tokamak was developed in the early 90s [41].

In the mid 90s, a real-time code, RT-EFIT, was developed. It gave information on the discharge

shape and safety factor profile. This code could be used as a tokamak discharge control tool during the discharge evolution [42].

In the late 90s, the spline representation for the functions p' and FF' was introduced as well as the addition of localized current sources.

In the early 2000s, electron charge exchange diagnostic was added to locate isotherm surfaces (which correspond well to the plasma flux surfaces), and they were used as constraints of the equilibrium reconstruction [43]. Current holes (regions with very small or zero current density) were also added as constraints.

In the mid-2000s, the Lithium beam polarity diagnostic was used to improve the measurement of the edge current density profile [44].

In the late 2000s, early 2010s Bayesian approaches for data assimilation were developed, [45].

In the 2010s, the addition of the current diffusion equation was proposed to improve the equilibrium without relying on the smoothness constraints [33].

1.4.4 Numerical methods to determine the energetic particle pressure component

To calculate the pressure contribution from energetic particles, numerical codes that simulate the heating and current drive are used. The process and codes used to do it depend on the external heating method.

When simulating the effects of ICRH and ECRH, first the launching, propagation, and absorption of the waves are simulated using wave codes that solve Maxwell's equations such as CYRANO [46], TORIC [47], EVE [48], LION [49] for ICRH and TORBEAM [50], TRAVIS, GRAY, TORAY for ECRH. The different sets of codes have different methods for solving the wave equations since the different frequency ranges between the two allow for different approximations. For ICRH full-wave solvers are used while for ECRH ray tracing methods are used. These codes give an initial distribution. Then Fokker-Plank codes, which solve the equation with the same name (kinetic equation that describes the evolution of the ion distribution functions), give the time evolution of the initial distribution. Examples of codes that are used for ICRH are RFOF [51], StixRedist [52], FPSIM, SSFPQL, etc.

When simulating NBI, the number of injected particles that are ionized must be calculated with an NBI initiation code such as BBNBI [53], NEMO [54]. Again an FP code is used to simulate the slowing down of the ionized particles through collisions in order to determine the time evolution of the distribution functions. Codes used are RISK [55], NBISIM, FIDIT.

1.4.5 Integrated tokamak Modeling

The goals of this thesis involve the use of different codes (equilibrium, heating) with different data provenance and thus are best addressed using Integrated Modelling approaches and frameworks. Here one briefly describes three well-known examples.

The European Integrated Tokamak Modeling Task Force (EFDA ITM-TF) simulation framework created a standardized platform and an integrated modeling suite of validated numerical codes for the

simulation and prediction of a complete plasma discharge of an arbitrary tokamak. To achieve this goal, the ITM-TF created a generic data structure with both the simulated and experimental data. This allows for the creation of integrated simulations using different codes and for codes that describe the same physics to be interchanged. The machine-related data is standardized, and the codes become independent of the tokamak experiment. This framework is being pursued by the EUROfusion Code Development for integrated Modeling project (WPCD) [56].

CRONOS is a numerical suit that solves transport equations. It integrates, in a modular structure, general 2D magnetic equilibrium, radiation and particle loss, several heat, particle impurities transport models, as well as heat particle and momentum source models [57]. It generates an input dataset from experimental data, runs the transport simulation, stores and allows visualization of the results.

OMFIT or One Modeling Framework for Integrated Tasks is a framework that uses a bottom-up strategy to integrated modeling. It has a free-form tree data structure at the core of the framework, that provides a unified way to collect, manage and exchange data from physics codes and experimental data management systems, and other integrated modeling frameworks [58].

1.5 Outline of the Thesis

This thesis starts with an introduction to nuclear fusion and its advantages as an energy source. There is also an introduction to the basic functioning of Tokamaks and some of the areas of study relevant to this thesis, such as equilibrium, heating and current drive, stability, confinement, and diagnostics. In the state of the art, a summary of the different types of reconstruction codes, a description of the algorithm for direct equilibrium reconstruction codes and their evolution are presented, along with a small description of the numerical methods for simulating external heating and a description of some of the existing integrated modeling frameworks.

In Chapter 2, the setup for the thesis is presented. This includes a description of the simulation infrastructure, the data (shot 90198 of JET), codes and workflows used to make the equilibrium reconstructions (EQUAL, EQSTABIL RECONSTRUCT AND REFINE, and EQSTABIL RECONSTRUCT AND REFINE Time Loop) and to simulate the external heating (CYRANO, StixReDist and HEATING AND CURRENT DRIVE).

In Chapter 3, the validation metrics used for the simulations made are presented, along with a description of the method used for the mapping of the diagnostics data and calculation of the thermal pressure from the diagnostics as well as the methods for obtaining the total pressure profile using the energetic particle pressure from the Heating and current drive workflow. Descriptions of the methods used for the various simulations made are also presented: reconstructions using only the magnetic diagnostics, using the thermal pressure profile and using the total pressure profile as a constraints, and using polarimetry and interferometry diagnostics.

In Chapter 4, the results of those simulations are presented.

First, the method to map the diagnostics and calculate the thermal pressure was tested. The electron temperature, density, and thermal pressure profiles are shown for the 48.0s time slice along with their

time evolution, from $42s$ to $52s$ (see Section 4.1).

Next, the workflows mentioned above were used to make equilibrium reconstructions using only the magnetic diagnostics (see Section 4.2) and using the magnetic diagnostics along with the thermal pressure profile (see Section 4.3). Here, the reconstructed profiles (the pressure, safety factor, toroidal current density) are shown along with their time evolution, as well as, for some global quantities such as the stored energy and plasma current.

The following step was to use the heating and current drive workflow to get the energetic particle pressure due to ICRH and then to calculate the total pressure profile. This was done for several time slices. Their total pressure profiles and their components are presented in Section 4.4.

Then equilibrium reconstructions are made using magnetic diagnostics and the calculated total pressure profiles. The results are presented in Section 4.5, along with a comparison between this and the two previous reconstructions.

Since the equilibrium reconstructions that used the total pressure profile were somewhat surprising (reconstructed profiles that did not match well to the calculated profiles, hollow current density, and safety factor profiles, worse MHD marker values, etc) some actions were tried in order to improve the results: First, checking how the equilibrium reconstruction used to map the HRTS diagnostics and as input for the heating and current drive workflow affected the total pressure profile and so, how it affected the equilibrium reconstruction, the results are in Section 4.6. Second, checking if multiple iterations of the calculation of the total pressure and equilibrium reconstructions would yield better results (as described in Section 1.4.2 for the thermal pressure profile), the results are presented in Section 4.7. Finally, polarimetry and interferometry diagnostic information was added to the reconstructions with the hope that these constraints would force the current density and safety factor profiles to become monotonic, the results are presented in Section 4.8.

In Chapter 5, a summary of the observations is made, the results are discussed and compared to other similar experiments, and some subjection on what might improve the results is made. The appendixes show the code parameters used for the various simulations made in the thesis.

Chapter 2

Setup

2.1 Simulation infrastructure and EUROfusion

One of the biggest challenges fusion research faces is that, once higher fidelity in the simulations is envisioned, few problems can be solved with standalone specialized tools/codes. This is justified by the large number of dependencies that any problem might involve i.e. the input data necessary can come from disparate sources and/or methods. Hence an "integrated approach" is necessary when addressing many of the physics problems in plasma discharges numerically. This rationale was behind the creation of several Integrated Tokamak Modeling efforts worldwide, including in Europe. One such effort was the EUROfusion Code Development for Integrated Modeling (WPCD) [56] including a significant number of modeling codes with a focus on integrated modeling.

The goals of WPCD are to (1) build on and optimize existing modeling codes, (2) add new physics to existing models, (3) create integrated workflows that include both the physics and machine information and that can be used for any device. These can be used for predicting, analyzing, and simulating plasma discharges.

The platform was made to be modular so that each physical module/code can be used along with others to form workflows. In order to achieve it, a generic data structure for both the simulated, and experimental data was created. The elements of the data structure are called Consistent Physical Objects or CPOs. The Universal Access Layer (UAL) library was developed in order to transfer these objects between modules and to write in an ITM database. It can be used with Fortran, C++, Python, Java, and Matlab. The Kepler scientific workflow manager is used to add together all the physics actors/codes into integrated simulations.

2.2 CPO

CPOs or Consistent Physical Objects is a physics based hierarchical data structure made to store data from various diagnostics, results from modeling/simulation codes, or a complete description of a physics area. These are used as the inputs and outputs of the various codes and scripts used in this work. The

information on the CPOs can be seen in [59]. In Table 2.1 is a description of the CPOs used in this work.

CPO	Description
equilibrium	Results of equilibrium codes. Stores both 1D and 2D profiles along with global quantities and the constraints and code parameters used.
magdiag	Magnetic diagnostic measurements and derived quantities from flux loops and poloidal field probes (plasma current, diamagnetic flux, magnetic field and flux)
pfsystems	Description of active poloidal coils, passive conductors, currents flowing in those and mutual electromagnetic effects on the device.
ironmodel	Model of the iron circuit.
msediag	MSE diagnostic measurements (polarization angle) and diagnostic setup.
tsdiag	Thomson scattering diagnostic measurements (electron thermal temperature and density) and diagnostic setup.
coreprof	Plasma 1D profiles obtained by solving the core transport equations or by fitting to experimental data.
wall	Geometry representation of the tokamak first wall
antennas	Information on the antenna systems for heating and current drive.
nbi	Geometry, energy and power representation of the NBI system.
coreimpur	Impurity species.
waves	Radio-frequency wave propagation and deposition.
coresource	Generic source term for the core transport equations.
distsource	Sources of particles for input to kinetic equations.
corefast	Flux surface averaged fluid measures and transport coefficients of energetic particle populations.
polardiag	Polarimetry measurements (faraday angle) and diagnostic setup.
interfdiag	Interferometry measurements (line integrated electron density) and diagnostic setup.
ece	Electron cyclotron emission diagnostic measurements (electron temperature) and diagnostic setup.

Table 2.1: Description of the CPOs used in this work

2.3 Kepler

Kepler is a software application for the analysis and modeling of scientific data [60]. It is used to make workflows, which consist of various steps (data analysis, computations,...) represented by actors - the basic building block of workflows. An actor can be composed of other connected actors that perform simpler tasks - known as a composite actor. Each actor has input and output ports for data and parameters

which customize it.

2.4 Data

In this work, shot 90198 of JET [61] is used. JET or Joint European Torus, is a European tokamak located in Culham Centre for Fusion Energy in Oxfordshire, UK that started operating in 1983. It has a major radius of $R_0 = 2.96m$, minor radius of $a = 1.25m$ (horizontal) and $b = 2.10m$ (vertical), magnetic field of $B = 3.45T$.

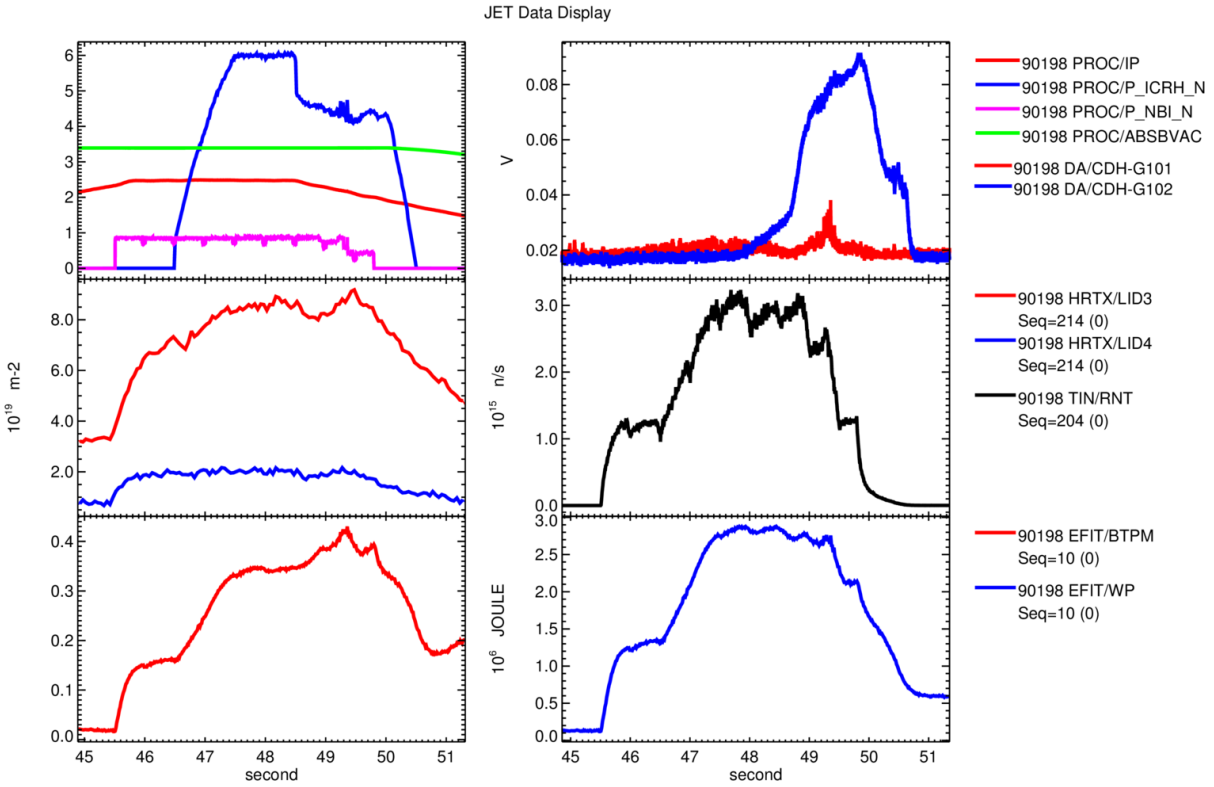

Figure 2.1: Jet data for shot 90198. The top-left graph shows the ICRH power in MW (blue), the NBI power in $\times 10MW$ (magenta), the plasma current in MA (red), and the toroidal magnetic field in T (green). On the middle left the graph shows the line averaged density through the plasma core in red and through the plasma edge in blue. On the bottom left the graph shows the poloidal plasma beta calculated using the EFIT code. On the top right, the graph shows the amplitude of the odd (red) and even (blue) toroidal mode number of magnetic perturbations measured at the tokamak first wall, converted to V. On the middle right, the graph shows the neutron rate and on the bottom right, the plasma stored energy in MJ calculated using the EFIT code.

Figures 2.1 and 2.2 provide some information about this shot. As can be seen, NBI heating starts at $45.4s$ (with $\sim 8.9MW$ power) reduces to $\sim 4.5MW$ at $49.4s$, and goes to zero at $49.8s$, the ICRH power increases from $0MW$ at $46.5s$ to $\sim 6.0MW$ at $47.5s$, then drops to $\sim 4.5MW$ at $48.5s$ and goes back to zero from $50.0s$ to $50.5s$. It can also be seen that the measured plasma current at $48.0s$ is $2.48MA$ and that the toroidal magnetic field is around $3.4T$. Another detail presented in Figures 2.2 is that the sawtooth instability, usually associated with the presence of a $q = 1$ magnetic surface in the plasma, only appears at around $t \sim 50.5s$, as evidenced by the appearance of regular spikes in the central channels of

the ECE diagnostics e.g. channels 78 and 96 in the graph showing the temperature measured with the ECE diagnostic.

Admittedly, this plasma discharge can be quite challenging to model since it presents a combination of two heating methods and, as is well known, ICRH can lead to significant energetic ion content. This is also evident from the relatively high neutron flux shown in Figure 2.1.

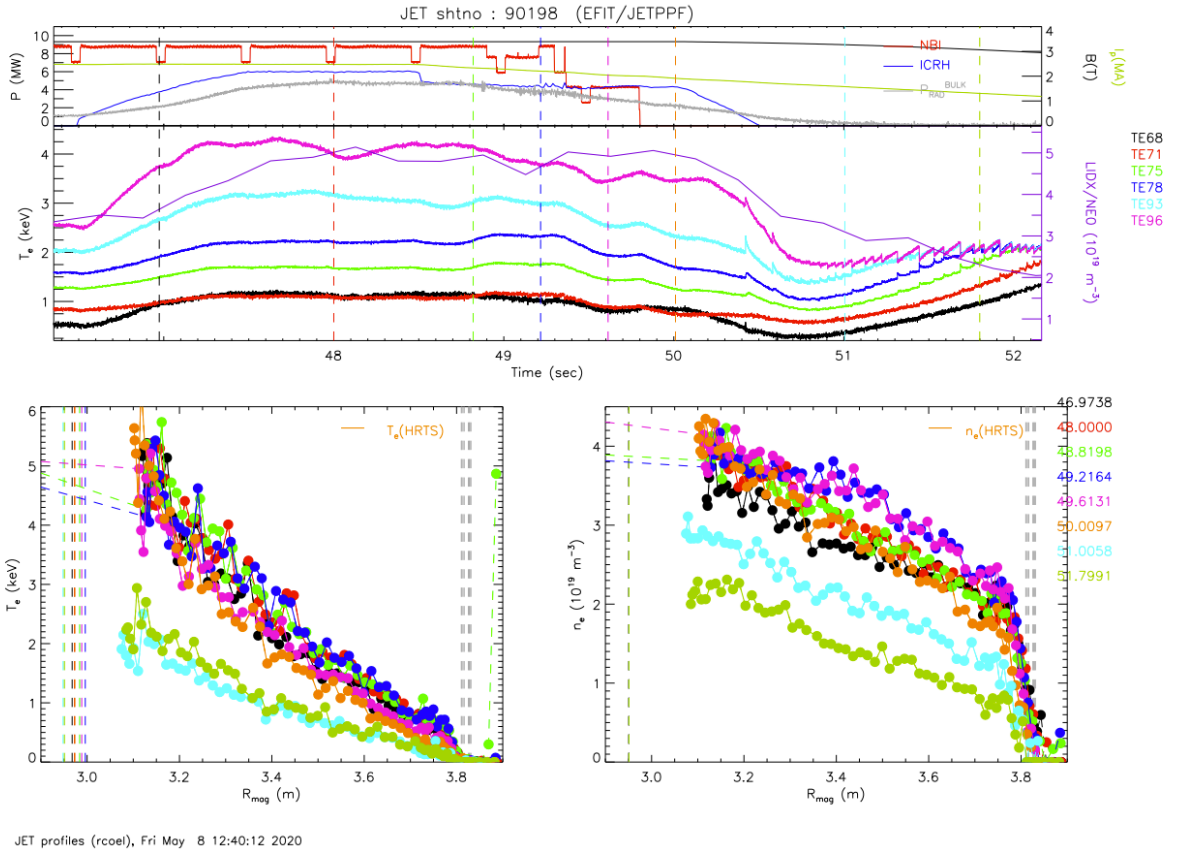

Figure 2.2: Graphs for the 90198 shot of JET. The top graph shows the NBI power and the ICRH power, in red and blue respectively, the plasma current in green, the magnetic field in black, and the radiated power in gray. The middle plot shows the electron temperature measured using the ECE diagnostic for different fixed frequency channels. The bottom left graph shows the electron temperature measurements with HRTS in function of R_{mag} (the major radius along the horizontal plane containing the magnetic axis) for several time slices. The bottom right graph shows the electron density measurements with HRTS in function of R_{mag} for several time slices.

In Figure 2.3, in the range of frequencies $[150, 200]kHz$ there are lines corresponding to $n = 1, 2, 3, 4, 5$ and 6, higher n corresponding to higher frequencies from $\sim 46.8s$ to $\sim 50.4s$. These correspond to Toroidal Alfvén Eigenmodes, see Section 1.3.6. These modes start to become more visible at around the same time as ICRH power is turned on and one might easily infer that the modes are driven by the ICRH driven energetic ion population.

In the range of frequencies $[50 - 100]kHz$, there is a noticeable blue area (so with toroidal mode number $n = 2$) from $46.8s$ to $48.2s$, the $f \sim 80kHz$ is believed to be a High Order Geodesic Acoustic Eigenmode [62].

In the range of frequencies from $[0, 50]kHz$, there are two stronger lines: for $f \sim 24kHz$ which

corresponds to toroidal mode number $n = 1$ from $46.0s$ to $49.5s$ and for $f \sim 12kHz$ which corresponds to toroidal mode number $n = 2$ from $47.0s$ to $50.0s$. The poloidal mode number associated with this $n = 2$ is determined empirically. As stated in Section 1.3.6, the (n, m) mode is resonant in the surface characterized by $q = m/n$, the m value has to be such that the surface exists in the plasma. The safety factor values at the core and edge are 1 and 4 respectively. Therefore, $m = 1$ does not work. The $m = 2$ and $m = 5$ and higher do not work because $q = 1$ and $q = 2.5$ are placed either closer to the core or to the boundary than expected by looking at Figure 3.2 and following analysis in Section 3.10. Therefore, the $m = 3$ poloidal mode number is left, corresponding to $q = 1.5$ surface. This $(m, n) = (3, 2)$ mode is believed to be a Neoclassical Tearing Mode, see Section 1.3.6.

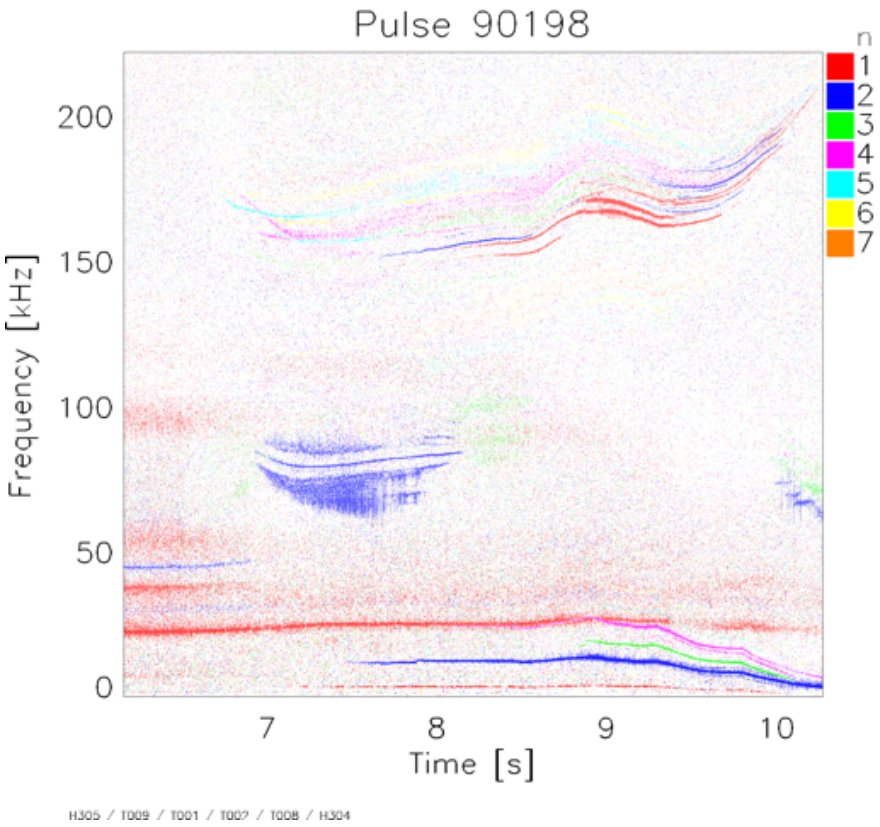

Figure 2.3: Time evolution of the toroidal mode spectra for the dominant MHD activity observed in shot #90198. The frequencies $f \sim [150 - 200]kHz$ correspond to Toroidal Alfvén Eigenmodes (TAEs), the $n = 2$ at $f \sim 12kHz$ is a $(3, 2)$ Neoclassical Tearing Mode (NTM) resonant at the $q = 3/2$ magnetic surface. The $n = 2$ mode at $f \sim 80kHz$ is believed to be a High Order Geodesic Acoustic Eigenmode (HOGAE) [62]

2.5 Codes

2.5.1 EQUAL

EQUAL is the equilibrium reconstruction code used. For a brief explanation of the algorithm, see section 1.4.1. This code uses, when available, the magdiag, pfsystems, toroidalfield, wall, ironmodel, msediag, interfdiag, polardiag, and coreprof CPOs, and stores the output on the equilibrium CPO. To adjust the

reconstruction various parameters can be changed, they are presented in Table 2.2. During this work, different sets of parameters for the profiles were tested: the number, position, and individual weights of the knots were changed along with the constraint weight and tuneff. The other parameters were kept the same: (1) B-splines were used, (2) the profiles of $P'(\psi)$ and $FF'(\psi)$ were not forced to zero at the boundary, and (3) the constraint type used was lang_lao. The pressure weights were also changed depending on the existence of the thermal or total pressure profile. The weights for faraday and the plasma density profile (ne) were also changed.

Generally, 97 grid points (advantageous for FAST Fourier transforms since it corresponds to $3 \times 2^5 + 1$ points) were used, but when using the total pressure profile they were increased to 129 ($2^7 + 1$).

The total plasma current, the measurements from the differential and flux loops, pick up and poloidal field coils, and iron magnetization were used and their weights were kept the same for the majority of the simulations. For this pulse, there were no MSE measurements and the diamagnetic signal was not used since it was not being stored in the CPOs (their weights were kept at 1×10^{-8}).

2.5.2 CYRANO

This is the wave code used within the heating and current drive workflow. It is used for ion cyclotron heating. It simulates the propagation of the radio-frequency waves (in the range of the ion cyclotron range frequencies) through the plasma. It uses the equilibrium, coreprof, antenna, and wave CPOs and stores the results on the wave CPO.

2.5.3 StixReDist

This is the Fokker-Plank code used within the heating and current drive workflow. This code is used for ion cyclotron heating. Combined with the wave code, it characterizes the evolution of the ion distribution when interacting with radio-frequency waves. This code uses the equilibrium, coreprof, antennas, and waves CPOs and fills the distribution CPO.

2.6 Workflows

2.6.1 EQSTABIL RECONSTRUCT AND REFINE

This is a Kepler workflow that reconstructs the plasma equilibrium using diagnostic data for a single time slice. This workflow has the ability to use either EQUINOX or EQUAL reconstruction codes and the HELENA, CHEASE, or CAXE high-resolution equilibrium codes. It can use, only the magnetic data to make the reconstruction, or in addition to it, use kinetic/thermal pressure profiles (from the coreprof or calculated using diagnostic data).

The workflow is separated into 5 main actors: INITIALIZATION, ReconstructEq, FixedBndCode, and Finalize, as shown in Figure 2.4. The INITIALIZATION actor reads the data from the IMAS database specified by the user, device, shot, and run_in provided for the closest time slice to the given time. It also checks the data for errors. The ReconstructEq makes a reconstruction using magnetic diagnostics

Grid	
nr	It's the number of grid points in the radial direction.
nz	It's the number of grid points in the vertical direction.
Fitting	
cocos_in	coordinate system convention of the input data
min_plasma_current	It's the minimum plasma current value at which the discharge is not considered to be in vacuum.
maxit	It's the maximum number of iterations.
error_iter	It's the error value at which the algorithm stops.
Weight	
ip	It's the fitting weight given to the total plasma current.
diamag	It's the fitting weight given to the diamagnetic signal.
flux	They are the fitting weights for the differential and flux loops measurements.
bpol	They are the fitting weights for the magnetic pick-up coils measurements.
pfcoils	They are the fitting weights for the poloidal field coils measurements.
iron	They are the fitting weights for the iron magnetization measurements.
mse	They are the fitting weights for the measurements of the motional stark effect diagnostic (MSE).
faraday	They are the fitting weights for the polarimetry measurements.
ne	They are the fitting weights for the interferometry measurements.
pressure	They are the fitting weights for the pressure profile points in the coreprof.
pressure_abserr	It's the absolute pressure error.
pressure_relerr	It's the relative pressure error.
pressure_data_type	It's the type of pressure profile. If "thermal", the thermal pressure (stored in profiles1d.pr_th in the coreprof) is used. If "total", the total pressure (stored in profiles1d.pr_perp in the coreprof) is used.
flux_in_weber	If "true", the flux in the flux loops is in Weber, if not it's divided by 2π.
Profile	
npprime and nffprime	They are the number of test functions for P' and FF' respectively.
pprime_type and ffprime_type	They set the type of test functions, P for polynomial and B for B-spline.
pprime_zerobound and ffprime_zerobound	If true, they force the profile gradients to zero at the boundary.
pprime_wbound and ffprime_wbound	They're weights constraining the profile gradients to be zero at the boundary.
pp_knot and ff_knot	They're the B-spline knots for the profiles.
pp_knot_tune_reg and ff_knot_tune_reg	They are individual weights on B-splines for the curvature constraint, to increase or decrease the curvature constraint locally (default=1.0). A typical application is to allow for strong gradients at the plasma boundary.
nstab	If 1, vertical stabilization is imposed. If 2, vertical stabilization is imposed, but the poloidal flux contribution is not stored in the output.
constraint_type	Type of regularization on current profile. If 'default' = no scaling, if 'langlao', scaled to get weight equivalent to EFIT's regularization, if 'current', scaled to be proportional to plasma current.
constraint_weight	It's the weight of regularization.
constraint_tuneff	It's the ratio of regularization for FF' relative to P'.
Output	
nprof	Number of radial points of output 1D profiles
cocos_out	coordinate system convention of the output data

Table 2.2: EQUAL parameters

and the pressure profile in the coreprof (if filled). Then, if the FBE variable is set to yes, a thermal pressure profile is calculated and a new reconstruction is made using the magnetic diagnostics and the calculated pressure profile as a constraint. The FixedBndCode redefines plasma boundary and calculates a high-resolution equilibrium. The new plasma boundary is set at the flux surface that corresponds to cut_off and so are the equilibrium profiles. The Finalize stores the CPOs in the run_out.

The inputs of the workflow are:

- FBEcode - reconstruction code.
- FBE_only - if set to "yes" it only does the reconstruction, not the high-resolution refinement. If set to "no", it does both.
- FBEkinetics - if set to "no", it does not map the experimental data nor does it calculate the thermal pressure and it does not do the second reconstruction.
- cut_eq - if set to "yes", the equilibrium is cut at cut_off.
- cut_off - It's the percentage of the normalized poloidal flux defining the magnetic surface acting as the new plasma boundary.
- eqcode - high-resolution code to be used

Figure 2.4: Representation of the EQSTABIL RECONSTRUCT AND REFINE workflow

2.6.2 EQSTABIL RECONSTRUCT AND REFINE Time Loop

This is a Kepler workflow that reconstructs the plasma equilibrium using diagnostic data for multiple time slices over a given time range with a given time step. This workflow has the ability to use either EQUINOX or EQUAL reconstruction codes and the HELENA, CHEASE, or CAXE high-resolution equilibrium codes. It can use data only the magnetic data to perform the reconstruction, or in addition to it use kinetic/thermal pressure profiles (from the coreprof or calculated using other diagnostic data).

The workflow is separated into 7 main actors: INITIALIZATION, Check TIME, Reconstruct, SAVE SLICE, ADVANCE TIME and STOP THE RUN, see Figure 2.5. The INITIALIZATION works as described in the previous section, STOP THE RUN as the same function as the finalize. The Reconstruct has the same function as the ReconstructEq and FixedBndCode. The other actors do as their names indicate.

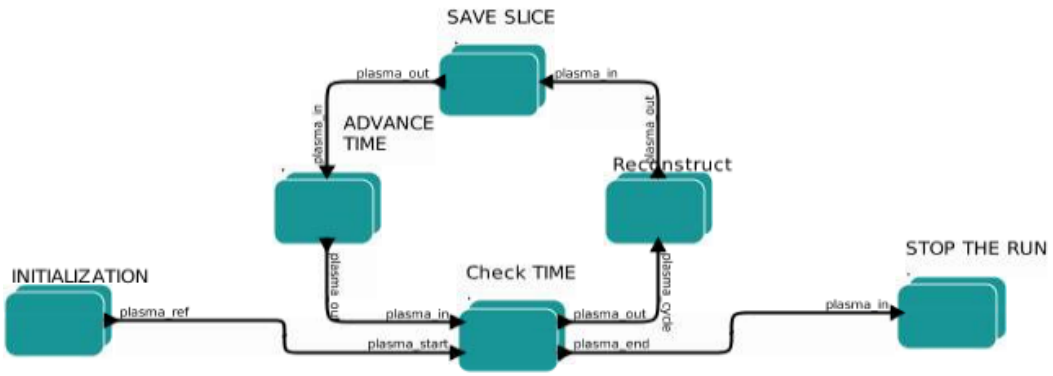

Figure 2.5: Representation of the EQSTABIL RECONSTRUCT AND REFINE with time loop workflow

2.6.3 HEATING AND CURRENT DRIVE

This is a Kepler workflow made for developing a composite actor for heating and current drive. This workflow simulates neutral beam injection, electron and ion cyclotron resonant heating.

The workflow is separated into several main actors: Initialisation, Initial HCD state, Control block for the time loop, Preprocess, Heating Current Drive, Rebundle, and Finalise, see Figure 2.6. In Initialisation actor the input parameters are validated, and the information from the CPOs (equilibrium, coreprof, coreimpur, coreneutrals, corefast, coredelta, waves, distsource, distribuition, wall, nbi, antennas,...) is added to a bundle along with the start, end and step time. The Initial HCD actor separates the information into plasma info, mach (includes the antennas, nbi, and wall), and hcd (includes waves, distsource, and distribuition), the CPO information can be overridden by the workflow parameters. The Preprocess actor updates the equilibrium using the CHEASE code (if update_equilibrium is set to true) and updates the neoclassic CPO (if update_neoclassic is set to false). The Rebundle actor updates the coreprof and hcd.

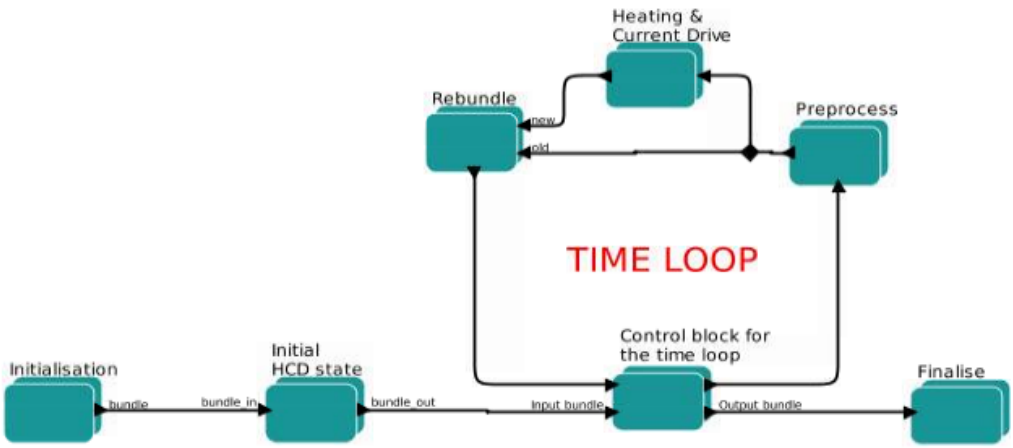

Figure 2.6: Representation of the Heating and current drive workflow

The HCD workflow core is easily seen to be organized in wave and particle source contributions (see

Figure 2.7). Indeed, there are initially two separate paths for the contributions of wave deposition codes (such as IEDEP, TORIC, EVE, LION or CYRANO for ICRH or GRAY, TORAYFOM, TORBEAM or TRAVIS for ECRH) and for NBI beam deposition codes (such as NEMO or BBNBI), these create/fill either the wave or distsource CPOs respectively. Both concur to build a distribution CPO that is suitably advanced by the appropriate Fokker-Plank code (though possible, no wave-NBI code synergies were used). The Coresource Corefast fill these CPOs using the results from the previous actors. This workflow needs the information in the equilibrium and coreprof CPOs (for every case) and additionally the information in the antennas and wall CPOs (in the case of ECRH), in the antennas, corefast, distribution CPOs and toroidal mode spectra (in the case of ICRH) and coreimpur, nbi and distsource CPOs (in the case of NBI).

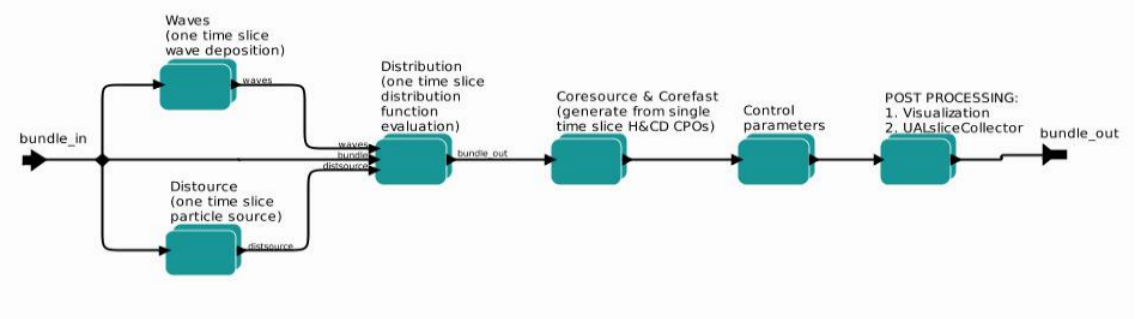

Figure 2.7: Representation of the composite actor for heating and current drive.

Chapter 3

Methods

3.1 Validation metrics used for the equilibrium reconstruction

Throughout this thesis, various simulations are made using the EQUAL code. According to Section 2.5.1, this code has various parameters that can be changed to get a better or a worse equilibrium reconstruction. Most important for this thesis, are the weights and placement of the B-spline knots and the pressure profile weights.

The EQUAL code minimizes the cost function as seen in Section 1.4.1, and so, it chooses an equilibrium reconstruction depending on the measurement errors.

To choose the best parameters for the reconstruction, various metrics are used: (1) the magnetic errors, (2) the shape of the pressure profile (if it stays positive close to the boundary or how similar it is to the given pressure profile) (3) the safety factor and flux surface averaged toroidal current density profiles shape (expected to be the ones from H-mode scenario, see Figure 1.7) (4) The existence or not of the $q = 1.0$, therefor the sawtooth instability (5) The safety factor value in the position of the $(3, 2)$ mode (see Section 2.4) according to the ECE and magnetic diagnostics (as explained in Section 3.10). The last point is only used for the $48.0s$ time slice.

3.2 Data analysis, Mapping of the data, and Calculation of pressure

In this section, the data obtained using Thomson Scattering (TS), specifically the electron density (n_e) and thermal electron temperature (T_e) are analyzed, mapped, and used to calculate the thermal pressure.

A python script is used. This script can map the data from the first two occurrences of the charge exchange spectroscopy diagnostic, which measures T_i (in case different charge exchange systems exist and have valid data), the first occurrence, if there is data, of the lithium beam diagnostic which measures n_e, the first occurrence, if it exists, of the electron cyclotron emission diagnostic which measures T_e and the first two occurrences (in case different Thomson scattering systems exist and have valid data) of the Thomson scattering diagnostic which measures T_e and n_e.

Since the time slices and time steps of the equilibrium and diagnostics are different, to map the data, the closest equilibrium time slice (t_{eq}) to the given value is chosen and the diagnostic data within half the equilibrium time step of that slice ($[t_{eq} - \Delta t/2 \; ; \; t_{eq} + \Delta t/2]$) are averaged and filtered.

When used as a part of the workflows mentioned in Section 2.6, there is only one equilibrium slice, so the time interval used to get the diagnostic data (to be filtered and averaged) is given by the user.

The values are mapped into the flux surfaces of a given equilibrium. Meaning, that the temperatures and densities, which are given in function of the R and Z coordinates, are turned into functions of the poloidal magnetic flux ψ (knowing the $\psi(R, Z)$).

The values are fitted to a function with a shape similar to the hyperbolic tangent to remove noise and the pressure is calculated with either $P = 2n_eT_e$ or $P = n_iT_i + n_eT_e$, depending on the existence of the charge exchange spectroscopy diagnostic data.

If there are two occurrences of the same diagnostic or multiple diagnostics that measure the same quantity, the data sets are shifted, if necessary, in relation to each other and fitted to the function multiple times. Then the best fit is chosen.

A final self-consistent (for both density and temperature) shift in the fitted profiles is made to ensure that the separatrix temperature does not deviate much from characteristic values for JET ($\sim 75eV$ based on two point models for energy flux through the separatrix). The electron temperature data is shifted so that $T_e(\rho_{pol,norm} = 1) = 70eV$, and the other data ($n_e$ and T_i) are shifted by the same amount. The value of $70eV$ is merely indicative and can be changed in the script.

The script follows the listed steps:

1. It gets the desired shot, equilibrium run, diagnostics run, time slice, time step, filter for the data, and information on the use of the electron cyclotron emission data using the *argparse* library.

2. It gets and checks the existence of a reconstructed equilibrium, the data from Thomson scattering diagnostic, lithium beam diagnostic, charge exchange spectroscopy diagnostic, and electron cyclotron emission CPOs using the *ual* and the *copy* libraries.

3. It interpolates ψ in function of R and Z values using the function *SmoothBivariateSpline* from the *scipy.interpolate* library, with a smoothing factor of 1% maximum value of ψ.

4. It filters and averages the data in time using the *signal.medfilt* function from the *scipy* library, and the *average* from the *numpy* library.

5. It maps the electron density data into the flux surfaces (from the Thomson scattering and from lithium diagnostics, if the data exists). This is done by using the interpolated function $\psi(R, Z)$, to get the function $n_e(\rho_{pol,norm})$, where $\rho_{pol,norm} = \sqrt{\frac{\psi - \psi_{axis}}{\psi_{boundary} - \psi_{axis}}}$.

6. The data from the different diagnostics is fitted to the function:

$$z = \frac{XSYM - x}{HWID}, \quad mod = \frac{(1 + |\alpha|z)\, e^z - (1 - |\beta|z)\, e^{-z}}{e^z + e^- z}, \quad Fped = Amod + B \tag{3.1}$$

$$y = Fped + (aheight - Fped) e^{-\left(\frac{x}{awidth}\right)^{aexp}} \tag{3.2}$$

Where A is half the pedestal height, B is the offset of the tanh, $XSYM$ is the position of the pedestal, $HWID$ is the width of the pedestal, *aheight* is the maximum of the function, *awidth* is the width of the Gaussian like function added and *aexp* is its the exponent. If there are multiple diagnostics data or multiple occurrences of the same diagnostic, the data sets are shifted in relation to each other and fitted multiple times, and the best fit is chosen. The fits are made using the *interpolate.splrep* function from the *scipy* library.

7. It maps the electron temperature data into the flux surfaces (from the Thomson scattering and from electron cyclotron emission if the data exists) in the same manner as before.
8. It shifts the electron temperature profile along $\rho_{pol,norm}$ so that $T_e(1) = 70eV$. Then, it shifts the electron density by the same amount.
9. It maps the ion temperature into the flux surfaces (from charge exchange diagnostic) if the data exists.
10. It shifts the ion temperature profile so that the ion temperature and electron temperature have the same pedestal centers.
11. Then it creates a common grid for the T_e, n_e and T_i data.
12. Then, it calculates the thermal pressure by using $P_{th} = n_e T_e + n_e T_i$ if T_i exists or $P_{th} = 2n_e T_e$ if it does not.
13. Finally, it saves the results to the coreprof CPO (if desired). If it is to be used for reconstruction, points are added at the magnetic axis and boundary, if not the points are interpolated again to be in the same grid as the equilibrium CPO.

This script was tested for multiple times slices to check the fits from 45.5s to 51.0s with a time step of 0.05s for the 90198 shot of JET. The results are in section 4.1.

A similar script was made, in order to do this for many time slices with either the equilibrium time step or a given value (if it's bigger). This script was tested using time slices from 42.0s to 52.0s using the equilibrium time step. The results are in section 4.1.

3.3 EQUAL testing with only magnetic diagnostics

The next step was to test the EQUAL reconstruction code using only the magnetic diagnostics. In order to do this, the workflows mentioned in Sections 2.6.1 and 2.6.2 were used.

The measurements used were the plasma current (ip), the diamagnetic signal (diamag), the measurements from the differential and flux loops (flux), from the pickup coils (bpol), from the poloidal field coils, and from the iron magnetization (iron).

Initially the EQSTABIL RECONSTRUCT AND REFINE workflow was used to test different EQUAL code parameters for multiple time slices. In the tests, the parameters changed were the number of grid points, the constraint weight, the pressure derivative, and FF' knot points and their corresponding individual weights and the constraint tuneff. The main objective was to fine-tune a set of parameters

that lead to a smooth pressure profile that was always positive (negative edge pressure is a common drawback when relaxing too much regularization).

Then the EQSTABIL RECONSTRUCT AND REFINE with time loop was used to get the equilibrium reconstruction from 46.0s to 52.0s with a time step of 0.1.

3.4 EQUAL testing with magnetic diagnostics and thermal pressure profile

The next step was to test the EQUAL reconstruction code using the magnetic diagnostics and the thermal pressure profile. In order to do this, the workflows mentioned in Sections 2.6.1 and 2.6.2 were used.

Initially the EQSTABIL RECONSTRUCT AND REFINE workflow was used to test different EQUAL code parameters for multiple time slices. The workflow follows the steps:

1. It makes the first equilibrium reconstruction using only the magnetic diagnostics and the EQUAL code, creating the $\psi(R, Z)$ function.
2. It maps the electron density and electron temperature obtained using the Thomson scattering diagnostic using the first equilibrium, transforming the $T_e(R, Z)$ and $n_e(R, Z)$ functions into $T_e(\psi)$ and $n_e(\psi)$ functions. Then, it calculates the thermal pressure ($P_{th}(\psi) = 2n_eT_e$) with a script similar to the one described in Section 3.2.
3. It makes a second equilibrium reconstruction, using the same magnetic diagnostics as well as the thermal pressure profile.

With this workflow, the EQUAL parameters used for the first and second equilibrium reconstruction are, by virtue of the way EQUAL code is designed, the same (they remain in memory during KEPLER execution). In the tests, the parameters changed were the constraint weight, the pressure derivative and FF' knot points, their corresponding individual weights, and the pressure weights. The main objective was to find a set of parameters that lead to a pressure profile that matches the thermal pressure profile, especially in the pedestal region.

Then the EQSTABIL RECONSTRUCT AND REFINE with time loop was used to get the equilibrium reconstruction from 46.0s to 52.0s with a time step of 0.1 with the same steps.

3.5 Heating and current drive workflow testing and calculation of the total pressure profile

In order to get the total pressure profile, it is necessary to calculate the energetic particle component of the pressure and add it to the thermal pressure. In this thesis only the ICRH is considered, the NBI contribution to the pressure profile was found to be much smaller than the ICRH. Therefore, the heating and current drive workflow described in Section 2.6.3 was used to calculate the energetic particle component of the pressure profile created by the ion cyclotron heating.

As can be seen in Section 2.4, at 48.0s the ICRH and NBI power are at a maximum. It can also be seen that at this time the plasma stored energy is in the middle of its highest step. From Sections 4.1 and 4.3 we can also see that the 48.0 time slice is located in the middle of the time interval where the pressure pedestal is well defined (and so where the plasma is considered to be in H-mode). Since the objective of the thesis is to study the equilibrium reconstruction using the pressure that comes from energetic particles originated from ICRH, this time slice was chosen for the initial tests.

The following steps are used:

1. The EQSTABIL RECONSTRUCT AND REFINE workflow was used to get a kinetic reconstruction (using the thermal pressure profile), with the same parameters for the first and second reconstructions. The 48.0s time slice was used.
2. The antennas and wall information was added to the run with the kinetic equilibrium reconstruction,
3. A new thermal pressure was calculated with the kinetic equilibrium and added to the coreprof CPO to be used in the heating and current drive workflow.
4. The heating and current drive workflow was used: First, the equilibrium reconstruction is updated using CHEASE code. Then, the wave code CYRANO is used to simulate the propagation of the ICRH waves and fill the wave CPO and the Fokker-Plank code StixReDist is used to characterize the evolution of the ion distribution when interacting with the waves and to fill the distribution CPO. Finally, the corefast CPO is filled.

After having the energetic ion pressure components written on the corefast CPO the total pressure was calculated with a script that follows these steps:

- It checks if the grids for the thermal pressure (in the coreprof) and the energetic particle pressure components (in the corefast) are the same.
- It adds the energetic particle pressure components and thermal pressure: $P_{tot} = P_{th} + P_{fast,e} + P_{fast,D} + P_{fast,H}$.
- It changes the grid of the total pressure to the equilibrium grid with cubic spline interpolation.
- It saves this new pressure to the coreprof CPO as profiles1d.pr_perp.

In order to add the pressure and to use the workflow, the thermal pressure had to be defined on the core region. The mapping of the Thomson scattering diagnostic, generally, only gives measurements for $\rho_{pol,norm} > 0.2$, so the extrapolated values from the fitted function outside of the domain of the fitting data were used.

Then the same process was used to calculate the total pressure for other time slices: 46.7s, 46.9s, 47.1s, 47.5s, and 49.0s. It was found in Section 4.1, that at 46.7s the pedestal, characteristic of the H-mode, is formed. The time slices of 46.9s and 47.1s are "located" in the increase of the core pressure, according to Section 4.1. It was found in Section 2.4, that 47.5s is the time at which the ICRH power reaches its maximum at 6.0MW. The 49.0 time slice is found in the decrease of the core pressure but before the disappearance of the pedestal (Section 4.1), in the lower step of the ICRH power of 4.5MW (Section 2.4), and in the decrease of the plasma current according to the Figure 4.16 in Section 4.3.

3.6 EQUAL testing with magnetic diagnostics and total pressure profile

The next step was to test the EQUAL reconstruction code using the magnetic diagnostics and the total pressure profile for the 48.0s time slice. In order to do it the following steps were followed:

1. The first equilibrium reconstruction was made using only the magnetic diagnostics.
2. The electron temperature and electron density from the High Resolution Thomson Scattering diagnostic were mapped into the flux surfaces of the first equilibrium.
3. The thermal pressure was calculated by $P_{th} = 2n_eT_e$.
4. The second equilibrium reconstruction was made using the magnetic diagnostics and thermal pressure.
5. The electron temperature and electron density from the High Resolution Thomson Scattering diagnostic were mapped into the flux surfaces of the second equilibrium.
6. The thermal pressure was calculated by $P_{th} = 2n_eT_e$.
7. The energetic particle components of the pressure was determined using the heating and current drive workflow.
8. The total pressure was calculated by $P_{tot} = P_{th} + P_{fast}$
9. The third equilibrium was made using the magnetic diagnostics and total pressure.

Steps 1-4 were made using the EQSTABIL RECONSTRUCT AND REFINE workflow. In order to get a reconstructed pressure profile as close as possible to the total pressure, and the safety factor profile with absolute values above 1 (no sawtooth instability) and with the right position for $q = 1.5$ (see Section 3.10 for a detailed description and rationale for the $m = 3$, $n = 2$ NTM location), various tests were made, with different combinations of the following modifications to the equal parameters:

- Increasing the number of grid points.
- Changing the pressure weights: Higher values at the core region and pedestal, smaller at the midradius.
- Adding more knots, at the points where the total pressure derivative has local maxima and minima.
- Decreasing the constraint tuneff, in order to give more importance to the pressure (as opposed to the FF' function).
- Decreasing the pressure relative error.
- Using the minimum possible value of constraint weight.

Then the same process was followed for the time slices: 46.7s, 46.9s, 47.1s, 47.5s, and 49.0s, using the parameters that were found to be the best for 48.0s.

3.7 Total pressure using different kinetic equilibrium reconstructions

Since the heating and current drive codes use both the equilibrium and coreprof CPOs as input and since the ICRH deposition, when located in the deep plasma core, is quite sensitive to the equilibrium flux map, we can anticipate that there will be different total pressure profiles for different equilibrium reconstructions. Thus, in this section, various total pressure profiles were made using different equilibrium reconstructions.

In order to do it, a magnetic equilibrium reconstruction was made using the EQUAL code, then the diagnostic data from Thomson scattering were mapped and the thermal pressure profile calculated. Using this thermal pressure profile, seven different equilibrium reconstructions were made using the EQUAL with different pressure weights:

- Reconstruction (a) - all pressure weights equal are set to 1.
- Reconstruction (b) - the pressure weights for $\rho_{pol,norm} > 0.75$ are set to 1 and the others to 0.
- Reconstruction (c) - the pressure weights for $\rho_{pol,norm} > 0.80$ are set to 1 and the others to 0.
- Reconstruction (d) - The pressure weights for $\rho_{pol,norm} > 0.90$ are set to 1 and the others to 0.
- Reconstruction (e) - The pressure weights for $\rho_{pol,norm} > 0.95$ are set to 1 and the others to 0.
- Reconstruction (f) - The pressure weights for $\rho_{pol,norm} > 0.97$ are set to 1 and the others to 0.
- Reconstruction (g) - All pressure weights are set to 0

For each of these reconstructions, a new thermal pressure profile is calculated, the energetic particle pressure components are determined using the Heating and current drive workflow, and the total pressure profile is constructed as was described in Section 3.5. Then these pressures are used in the equilibrium reconstruction, to see if there are improvements when compared with the previous section.

3.8 EQUAL testing with two iterations of the total pressure

In this section, two iterations of the equilibrium reconstruction using the total pressure profile are made. To do this the following steps are used:

1. First equilibrium reconstruction using the EQUAL code and only the magnetic diagnostics.
2. Mapping the electron temperature and density from the HRTS diagnostics into the first equilibrium and calculating the thermal pressure profile by $P_{th} = 2n_eT_e$.
3. Second equilibrium reconstruction using the EQUAL code and the thermal pressure profile as a constraint.
4. Mapping of the TS diagnostics and calculation of the thermal pressure profile.
5. Determination of the energetic particle pressure components using the Heating and current drive workflow.

6. Calculation of the total pressure profile by $P_{tot} = P_{th} + P_{fast}$.
7. Third equilibrium reconstruction using the EQUAL code and the total pressure profile as a constraint.
8. Mapping and calculation of the Thermal pressure profile.
9. Second use of the Heating and current drive workflow to calculate the energetic particle components of the pressure.
10. Calculation of the total pressure profile.
11. Fourth equilibrium reconstruction

For the fourth reconstructions, several were made and the best was chosen (with the criteria mentioned in Section 3.1). The parameters for the reconstructions were chosen as before:

- The knots of the p' and FF' functions were placed at the maximums and minimums of the pressure derivative;
- The individual weights of the p' and FF' functions were somewhat proportional to the derivative values (stronger binding to sharp variation in the profile);
- Higher values of pressure weights at the core and pedestal were used;
- The smallest value of the constraint weights was used.

3.9 EQUAL testing with polarimetry and interferometry

In an attempt to get better results, in this section, the interferometry and polarimetry diagnostics measurements were added to the reconstruction. These diagnostics measure the integrated electron density and Faraday rotation angles along certain lines of sight, that cross the core of the plasma. Since they give more information along lines of sight that pass through the core of the plasma, it was expected that their addition to the reconstruction would facilitate getting a better pressure profile and monotonic safety factor and flux surface averaged toroidal current density profiles, since their addition would give a restriction, even if indirectly, to the FF' profile.

First, these diagnostics were added to the magnetic only reconstruction and to the kinetic reconstruction using the thermal pressure profile. Various parameters were tested for the $48.0s$ time slice. The best from parameters from the tests were used to make the reconstruction from $46.0s$ to $52.0s$ with a time step of 0.1.

These measurements were also added to the kinetic reconstruction with the total pressure profile for the same time slice.

The equilibrium reconstructions only use channels 3, 5, and 7 of the polarimetry and interferometry diagnostics [1].

[1] These channels were chosen since there is a systematic offset of the other Faraday angle channels (due to unknown causes) preventing their regular use on EFIT according to private communication with EFIT responsible officer at JET.

3.10 Comparing the Reconstructed q value in the (3,2) mode position, obtained with the ECE and magnetic diagnostics

From Section 2.4 it was concluded that (3,2) mode was present in this shot. From the data in Figure 3.2, the location of the magnetic surface with $q = 3/2$ can be found and the corresponding q value from the equilibrium reconstruction determined.

Since the ($n = 2$,$m = 3$) mode is expected to be a typical Neoclassical Tearing Mode (NTM), it does cause magnetic reconnection and thus an inversion in the temperature perturbation at opposite sides of the magnetic surface where $q = 3/2$. As such, it can be located by looking for the π jumps in the phase of the cross power spectral density (CPSD) or coherence between the temperature fluctuations and the magnetic signal, where the coherence between the two signals is large. These jumps happen at $R \approx 2.60m$, $R \approx 3.25m$ and $R \approx 3.35m$. Admittedly, there should only be a single jump at the High Field Side ($R \sim 2.6m$) and at the Low Field Side since the q-profile is not expected to be hollow. The analysis of Figure 3.2 also evidences that at the most external phase jump ($R \sim 3.35m$) the temperature perturbation is quite low and the coherency is much noisier. Therefore, it is highly unlikely that the jump is "physical". We keep the two values ($R \sim 3.25m$ and $R \sim 3.35m$) since they may be useful for validating the reconstructions since they provide a convenient error bar to the estimated position of the $q = 3/2$ surface. To get the q values calculated by the EQUAL code in these positions, these steps are followed:

1. From the plot of the electron temperatures see Figure 3.1, the electron temperatures that correspond to the found R values are determined.
2. Then the ECE channel and their frequencies are identified (for the $R \approx 2.6m$ two channels were found with similar temperatures, hence the two different in Table 3.1)
3. The magnetic field is calculated (it's assumed to be approximately given by the toroidal magnetic field since the poloidal component is much smaller).
4. The interpolation of the $B_\phi(R, Z)$ from the EQUAL reconstruction is used to find the value of R (the reconstructed ones, not the same as in Figure 3.1) for the channel (knowing the Z position, which is constant for all ECE measurements).
5. The interpolation of $\psi(R, Z)$ is used to find the ψ value, knowing the R and Z values.
6. The interpolation of the $q(\psi)$ is used to find the q values.

The values for the toroidal magnetic field and the frequency, temperature, and R, used to get to those values are presented in table 3.1. The other values are dependent on the reconstruction so they will be shown in Chapter 4.

3.11 Finding the radial location of the ICRH deposition

In order to find the radial location of the ICRH deposition, the wave frequencies used were found, along with the masses of the ions present in the plasma. Then the first and second harmonics of the frequencies

	$R_{EFIT}(m)$	$\Delta()$	$T_e(keV)$	channel	$f(GHz)$	$B_\phi(T)$
1	3.35	183	2.6	80	85.20	3.0436
2	3.25	171	3.0	81	86.20	3.0794
3	2.6	183	4.0	40 41	109.7 110.2	3.9189 3.9367

Table 3.1: Values to get the toroidal magnetic field. Where R_{EFIT}, Δ and T_e are the value of R seen in Figure 3.2, the channel and f are determined by the T_e, the B_ϕ is the toroidal magnetic field calculated knowing the frequency.

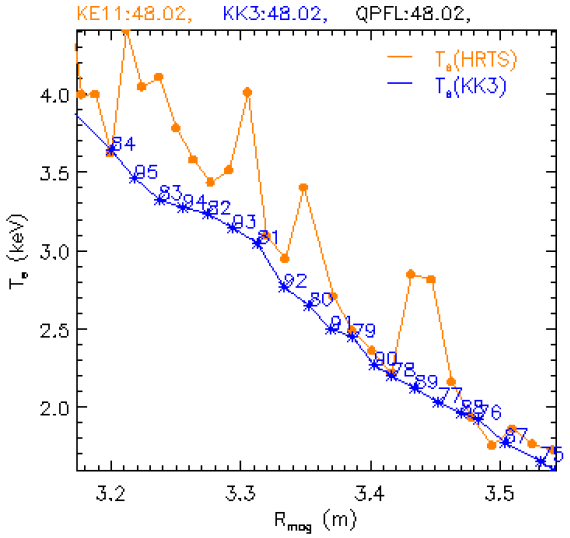

Figure 3.1: Electron temperature in function of R_{mag}. The Orange line is the electron temperature measured by Thomson scattering and the blue line is the electron temperature measured by ECE with the identification of the measurement channels.

were determined. Then the toroidal magnetic field was calculated using the mass of each ion and assuming that the frequencies used were either the first or second harmonic of the frequency. The toroidal magnetic field ($B_\phi(R,Z)$) from the equilibrium reconstruction is interpolated and used to find the radial position that corresponds to the required magnetic fields. The frequency values and magnetic fields can be found in Table 3.2. The radial locations depend on the equilibrium reconstruction, thus they can be found in Chapter 4.

		$f_1 = 49.0MHz$	$f_2 = 51.0MHz$	$f_3 = 51.4MHz$
Hydrogen $m_H = 1.67 \times 10^{-27}kg$	$1^{st}harmonic$ $2^{nd}harmonic$	$B_\phi = 3.22T$ $B_\phi = 1.61T$	$B_\phi = 3.35T$ $B_\phi = 1.68T$	$B_\phi = 3.38T$ $B_\phi = 1.69T$
Deuterium $m_D = 3.34 \times 10^{-27}kg$	$1^{st}harmonic$ $2^{nd}harmonic$	$B_\phi = 6.44T$ $B_\phi = 3.22T$	$B_\phi = 6.70T$ $B_\phi = 3.35T$	$B_\phi = 6.75T$ $B_\phi = 3.38T$

Table 3.2: Toroidal magnetic field where resonance happens for both ions species present in the plasma and assuming that they are either first or second harmonics. Shot=90198

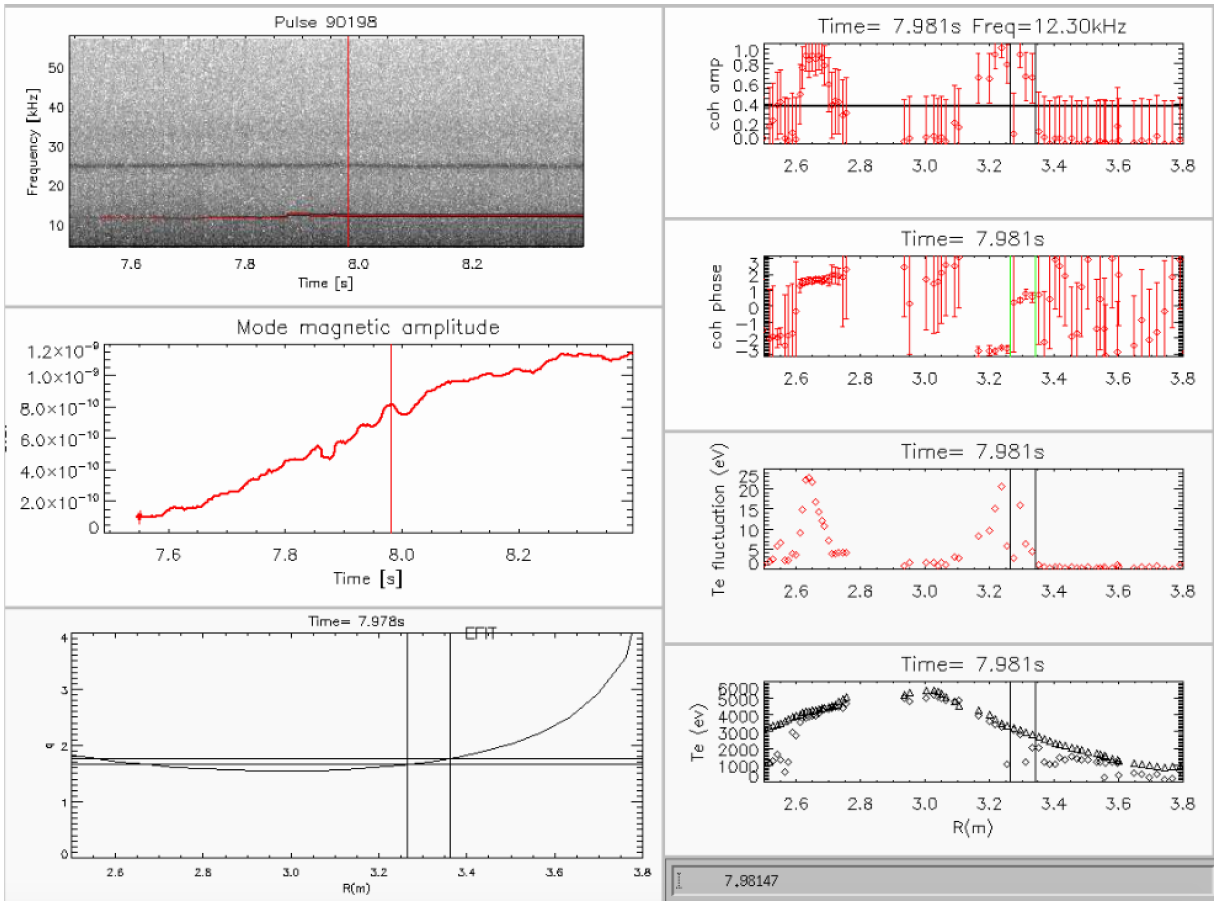

Figure 3.2: First plot on the left: Spectrogram of the magnetic signals. Second plot on the left: Magnetic amplitude of the mode corresponding to 12.3kHz. Third plot on the left: Safety factor profile at time 7.981s made with EFIT. First plot on the right: Amplitude of the cross power spectral density (CPSD), or coherence between the temperature fluctuation signal from ECE and the magnetic signal in function of R at frequency 12.3kHZ. Second plot on the right: Phase of the CPSD between the temperature fluctuation signal from ECE and the magnetic signal in function of R at frequency 12.3kHz and at time 7.981s. Third plot on the right: Electron temperature fluctuation from ECE at time 7.981s. Fourth plot on the right: Electron temperature from ECE in function of R at time 7.981s.

Chapter 4

Results

4.1 Data analysis, Mapping of the data, and Calculation of pressure

To test the script described in Section 3.2, various time slices were used. Here the results for the 48.0s time slice are shown.

In Figure 4.1, the electron density and electron temperature measured with the Thomson scattering diagnostic are shown in function of $\rho_{pol,norm}$, after they were mapped into the flux surfaces. The fitted functions to these data sets are also shown. In this time slice, the electron temperature pedestal is obvious, its center is at $\rho_{pol,norm} = 0.94935 \pm 0.00001$. It also shows the data and fitted functions after being shifted to have $\rho_{pol,norm}(T_e = 70eV) = 1$. Before the shift the value was $\rho_{pol,norm}(T_e = 70eV) = 0.9798$.

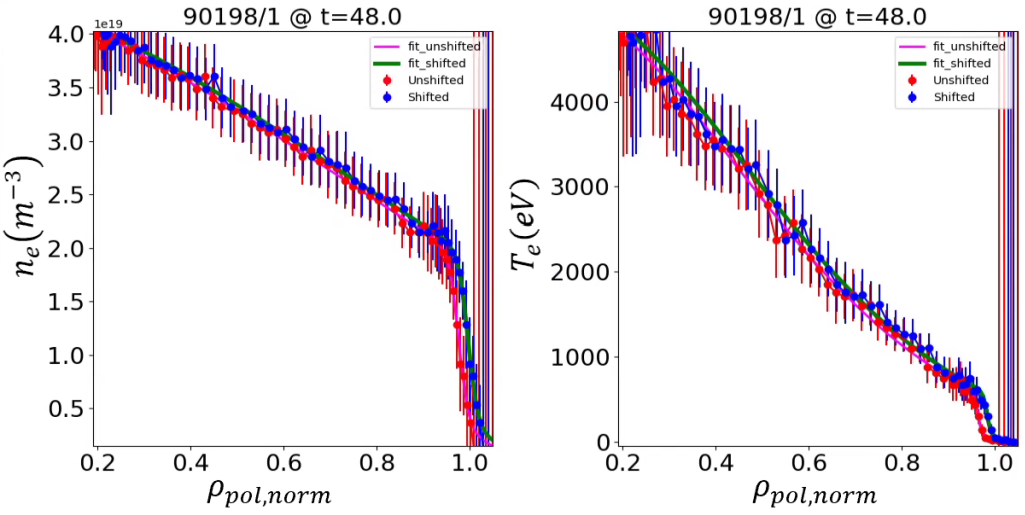

Figure 4.1: On the left: electron density in function of $\rho_{pol,norm}$. On the right: electron temperature in function of $\rho_{pol,norm}$. In red: the initial data. In blue the shifted data. The pink line is the function fitted to the data, and the green line is the same function after the shift. Shot=90198, Run_eq=1, Run_diag=1 Time=48.0s.

In Figure 4.2, the electron temperature and electron density fitted and shifted profiles are shown, as well as the comparison of the pressure profiles: the thermal pressure profile calculated with $2n_eT_e$ and the one in the equilibrium CPO (equilibrium reconstruction using only the magnetic diagnostics). As can be seen the pedestal present in the pressure calculated using the diagnostics does not appear in the equilibrium pressure profile.

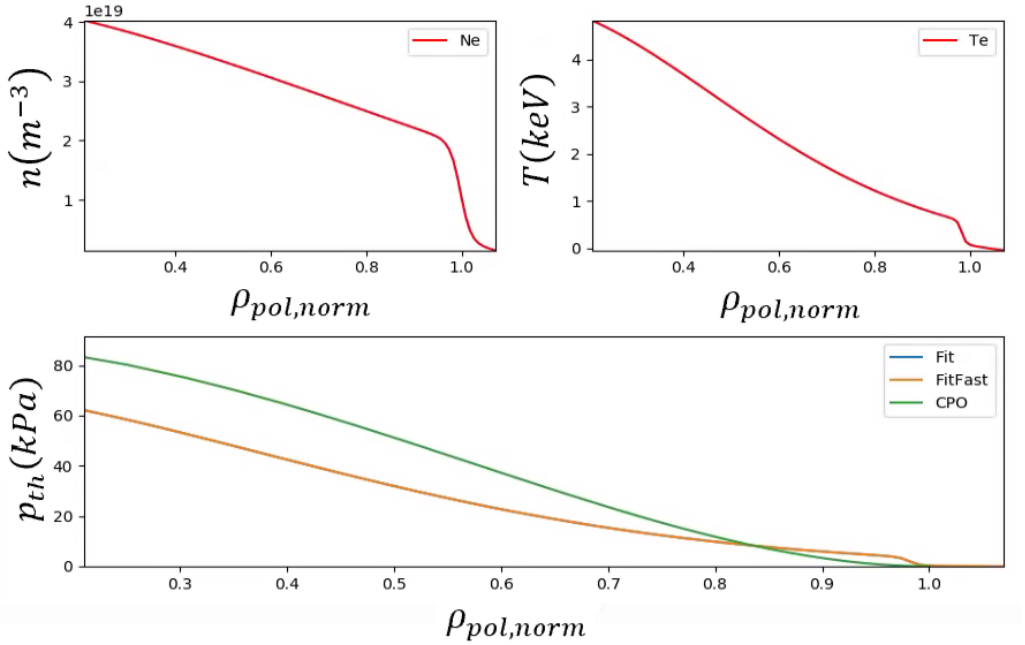

Figure 4.2: On the top left: electron density fitted function. On the top right: electron temperature fitted function. On the bottom: pressure in function of $\rho_{pol,norm}$, the yellow line using $2n_eT_e$ and the green line is the pressure profile from the equilibrium CPO. Shot=90198, Run_eq=1, Run_diag=1 Time=48.0s.

The script with the time loop was used to see the shape of the electron temperature, electron density, and thermal pressure in function of time and $\rho_{pol,norm}$.

In Figure 4.3, it can be seen that the density on the core increases from $1-2\times10^{19}m^{-3}$ to $3.5-4\times10^{19}m^{-3}$ at $\sim 47s$, an indication of the increased confinement considering the gas fueling remained reasonably constant from $t\sim[46-49.5]s$.

In Figure 4.4, it can be seen that there is an increase in the core temperature to $\sim 4.5KeV$ at $47.0s-50.0s$, and the incremental appearance of the pedestal at around $\rho_{pol,norm}\approx 0.98$. A dip in the core temperature at around $49.0s$ can also be seen.

In Figure 4.5, we can see the formation of the pedestal at around $46.7s$ and its disappearance at around $49.7s$. The increase in the core pressure (at $\rho_{pol,norm}<0.2$) starts at around $47s$ and reaches a maximum of $55kPa$ at around $48.0s$. There is a dip in the core pressure at around $50s$ followed by an increase to $60kPa$ at around $51.0s$. The appearance of the pedestal and increase in the core pressure at $46.7s$ happens at around the same time as the start of the ICRH wave deposition, and the first dip in the core pressure and disappearance of the pedestal at $49.7s$ happens in the time vicinity where the ICRH wave and NBI power start to decrease and the gas fueling is drooped accordingly.

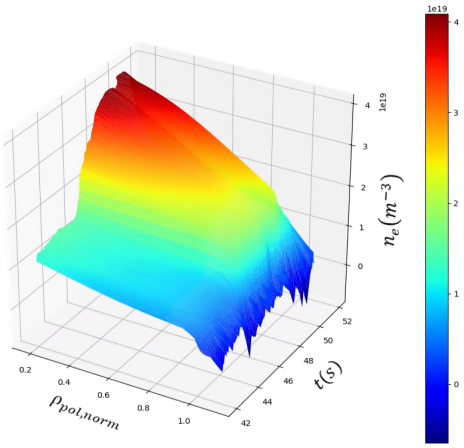

Figure 4.3: Fitted and shifted data of electron density from Thomson Scattering in function of time and $\rho_{pol,norm}$. Shot=90198, Run_eq=1, Run_diag=1.

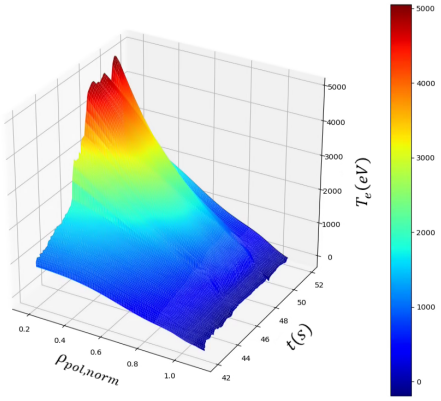

Figure 4.4: Fitted and shifted data of electron temperature from Thomson Scattering in function of time and $\rho_{pol,norm}$. Shot=90198, Run_eq=1, Run_diag=1.

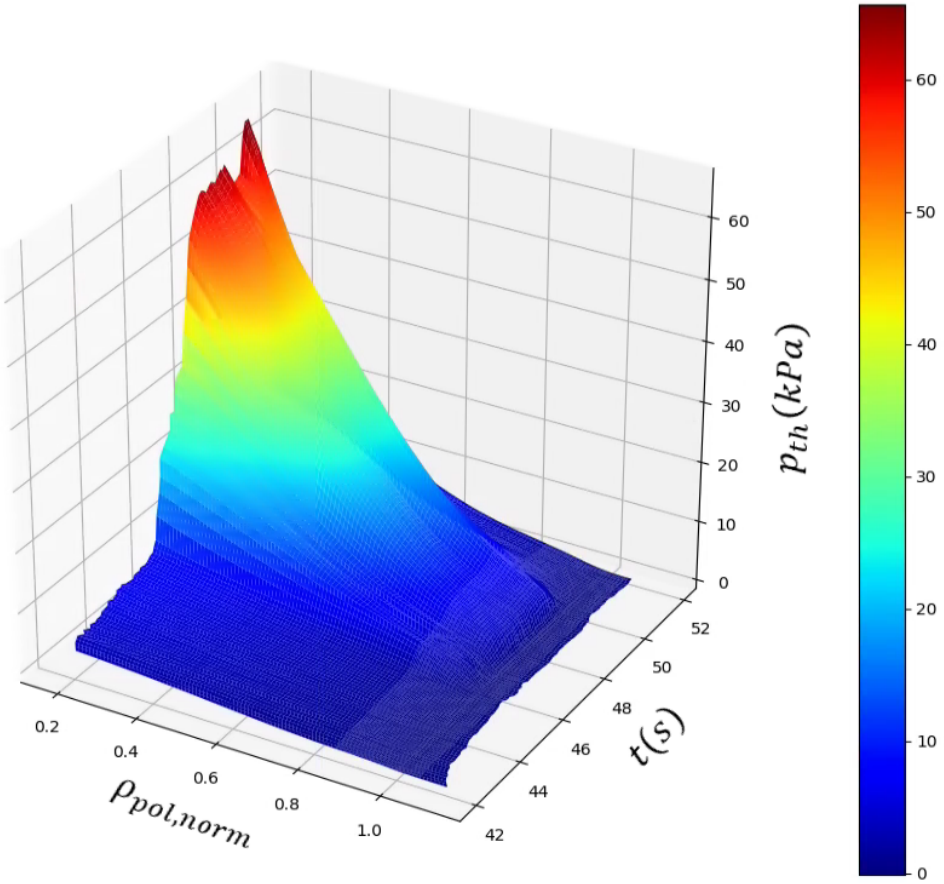

Figure 4.5: Thermal pressure calculated with the electron density and temperature from Thomson scattering in function of time and $\rho_{pol,norm}$. Shot=90198, Run_eq=1, Run_diag=1.

4.2 EQUAL testing with only magnetic diagnostics

In the first set of tests, the number of grid points was changed. The values tried were: 20, 65, 129, and 180. No significant differences were seen in the results when using 65, 129 and 180. When using 20 grid points spikes appear in the flux surface averaged toroidal current density and safety factor profiles in the core region.

In the second set of tests, the constraint weight was changed. The values tried were 0.0005, 0.001, 0.002 and 0.008. Decreasing this parameter leads to more oscillations in the profiles, which may lead to negative pressure profiles. So when using only the magnetic diagnostics a higher value for the constraint weight is preferred.

In the third set of tests, the individual weights for each radial knot of the pressure derivative B-spline were changed. Decreasing the values has the same effect as the constraint weight but localized to the position of the knots. So again higher values are preferred, especially, for the knots located next to the plasma boundary (where the pressure can become negative).

In the fourth set of tests, the placement and number of knots of the p' and FF' profiles were changed. A smaller amount of knots leads to smother profiles, since "local features" in the profile are inhibited by construction.

After the tests, the parameters presented in appendix A.1 were chosen. In Figure 4.6, the reconstructed equilibrium profiles at 48.0s are presented along with the contour plot of the flux surfaces. From the pressure profile, it can see that there is no pedestal in this time slice and that the pressure is not negative. It can also be seen that the safety factor does not cross the $q = 1.0$ line as expected.

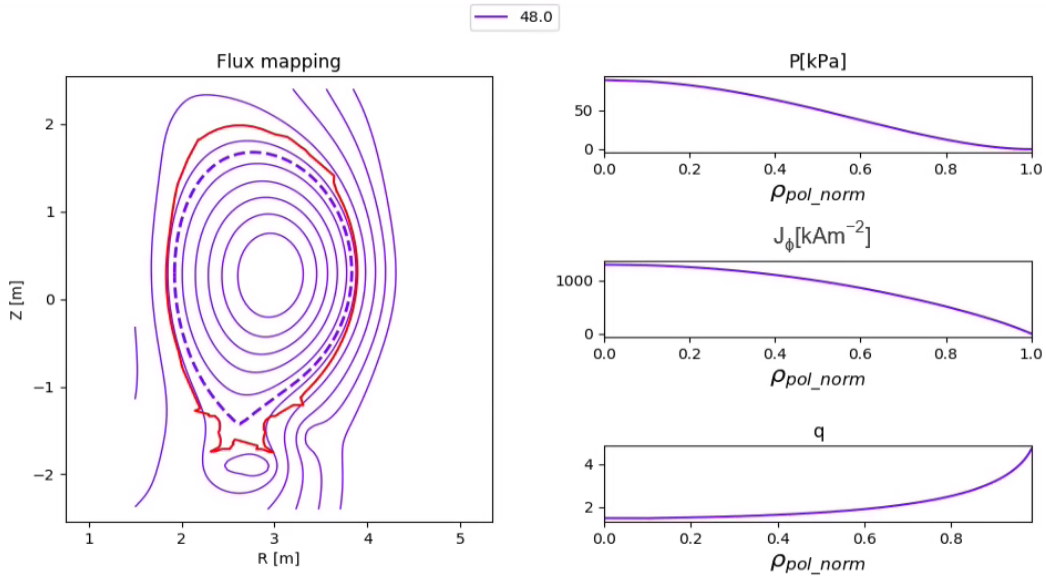

Figure 4.6: On the left: Contour plot of the flux surfaces. On the top right: Pressure profile. On the middle right: Flux surface averaged toroidal current density profile. On the bottom right: Safety factor profile. Shot = 90198. Run_eq = 2001. Time = 48.0s.

In Table 4.1, the values of the safety factor and their relative error values for the $n = 2$ and $m = 3$

mode position when compared with $q = 1.5$ are presented, they were calculated according to the method described in Section 3.10.

In Figures 4.7 and 4.8, it can be seen that the pedestal never exists and that the pressure profile never becomes negative. From Figure 4.9, it can be seen that the safety factor never crosses the q=1 line, which would have been expected at $51s - 52s$.

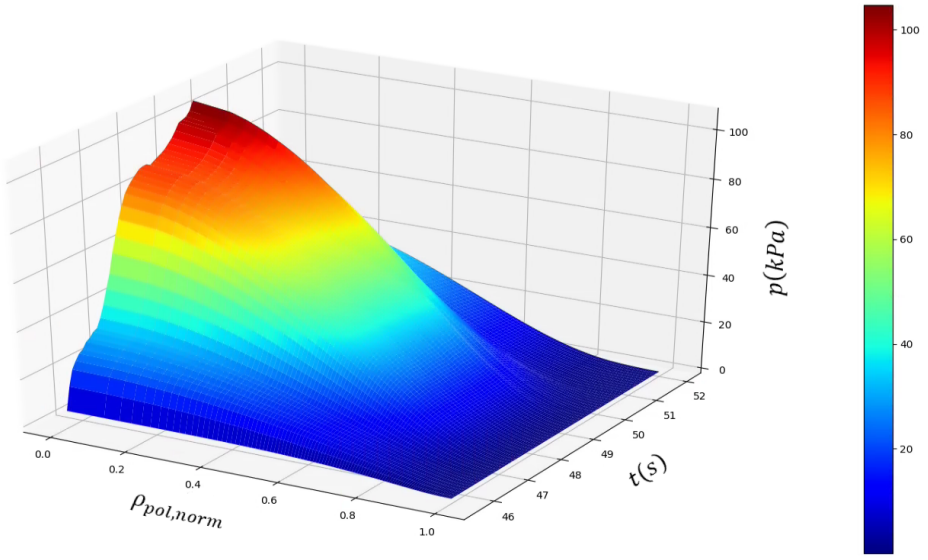

Figure 4.7: Pressure profile obtained from the equilibrium reconstruction using only the magnetic diagnostics in function of time and $\rho_{pol,norm}$. Shot=90198, Run_eq=2001.

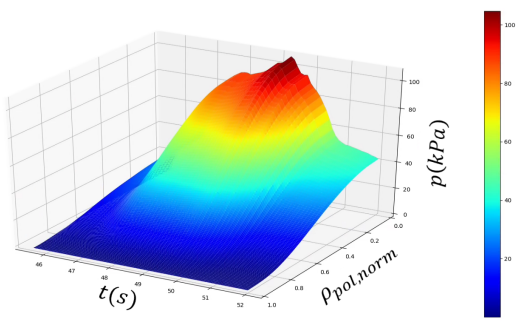

Figure 4.8: Pressure profile obtained from the equilibrium reconstruction using only the magnetic diagnostics in function of time and $\rho_{pol,norm}$ (different perspective). Shot=90198, Run_eq=2001.

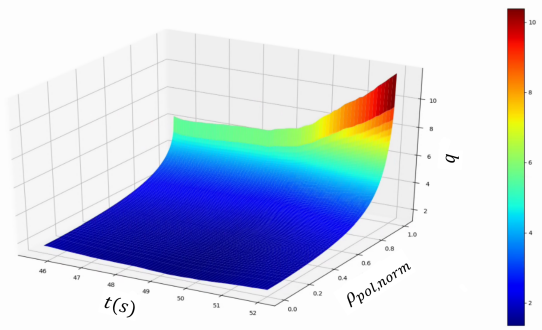

Figure 4.9: Safety factor profile obtained from the equilibrium reconstruction using only the magnetic diagnostics in function of time and $\rho_{pol,norm}$ (different perspective). Shot=90198, Run_eq=2001.

B_ϕ	R	ψ	q	$R.E(q)$
3.0436	3.3280	4.2557	1.6885	12.6
3.0794	3.2918	4.0000	1.6442	9.6
3.9189	2.5822	4.2546	1.6901	12.7
3.9367	2.5701	4.3307	1.7048	13.7

Table 4.1: EQUAL safety factor value that corresponds to the $n = 2$ and $m = 3$ mode and the relative error when compared to $q = 1.5$. Obtained according to section 3.10. Shot = 90198. Run = 2001. Time = 48.0s.

4.3 EQUAL testing with magnetic diagnostics and thermal pressure profile

In these tests, the thermal pressure profile is used. So, getting negative pressure next to the plasma boundary is not a problem. This allows for the use of smaller values of constraint weight and individual knot weights.

Since the objective of this section is to get a reconstructed pressure profile that is similar to the thermal pressure profile, especially in the pedestal region, knot points were added in this region (to allow for more flexibility in the function) and their individual weights were decreased.

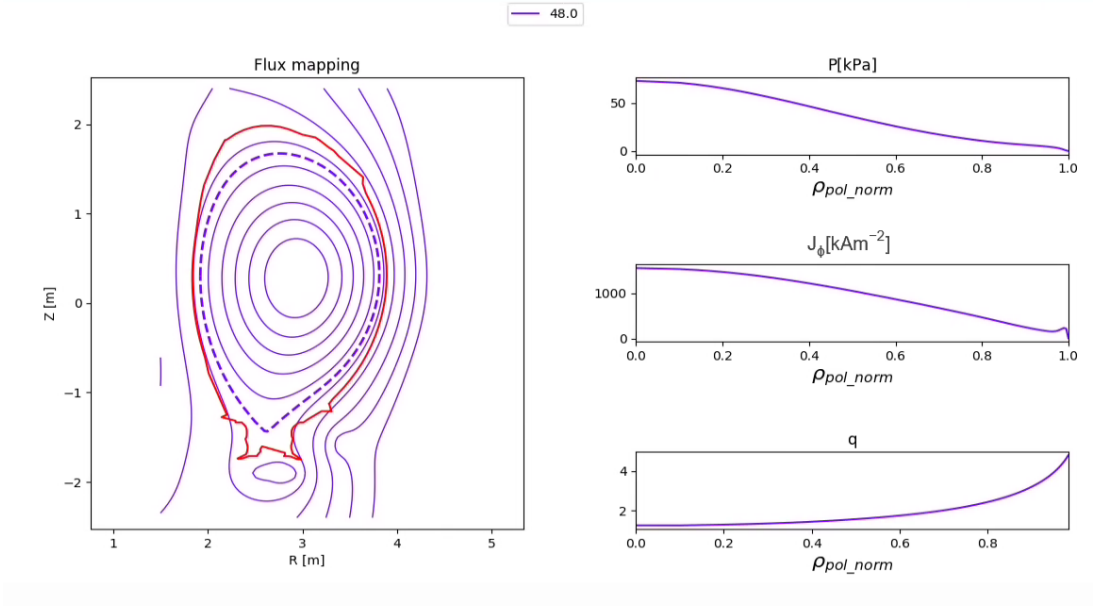

Figure 4.10: On the left: Contour plot of the flux surfaces. On the top right: Pressure profiles. ON the middle right: Flux surface averaged toroidal current density profiles. On the bottom right: Safety factor profiles. Shot = 90198. Run_eq = 2003. Time = 48.0s.

During these tests, the error_iter parameter had to be increased, so that the code would converge.

The chosen parameters for the reconstruction are the ones presented in appendix A.2. EQUAL uses Fortran "save" commands for some of the variables stack (including regularization and knot weights) to

speed up execution when performing multi time code executions, this is propagated into the workflow execution and thus the same parameters are used in the first (magnetic only) and second (kinetic) reconstructions.

In Figure 4.10, the profiles from the second reconstruction for the 48.0s time slice can be seen. Some differences, when compared with the first reconstruction, are: the pedestal can be seen in the pressure profile and in the flux surface averaged toroidal current density profile, and there is a decrease in core pressure and an increase in the core flux surface averaged toroidal current density. There aren't any obvious changes to the shape of the safety factor profile.

In Figure 4.11, the comparison between the thermal pressure profile and the pressure profile from the second reconstruction is presented. It can be seen that the two are very similar.

In Table 4.2, the values of the safety factor for the $n = 2$ and $m = 3$ MHD mode position and their errors are presented. As can be seen, they are improved when compared with the values from the magnetic only reconstruction.

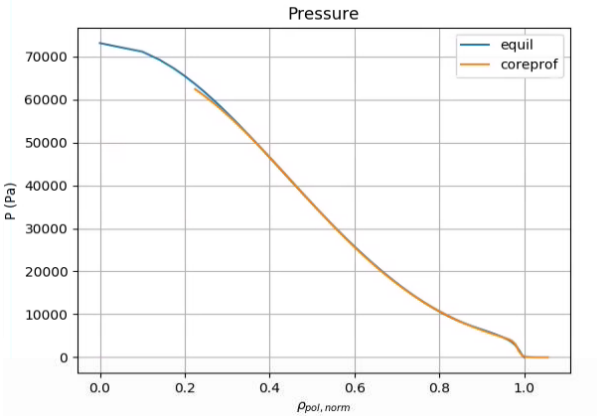

Figure 4.11: Shot = 90198. Run_eq = 2003. Time = 48.0s.

B_ϕ	R	ψ	q	$R.E(q)$
3.0436	3.3317	4.3428	1.5527	3.5
3.0794	3.2953	4.0553	1.4899	0.7
3.9189	2.5943	3.9364	1.4650	2.3
3.9367	2.5817	4.0191	1.4821	1.2

Table 4.2: EQUAL safety factor value that corresponds to the $n = 2$ and $m = 3$ mode and its error when compared to $q = 1.5$. Obtained according to section 3.10. Shot = 90198. Run = 2003. Time = 48.0s.

In Figures 4.12, 4.13, and 4.15, it can be seen that the pressure profiles are never negative and that the pedestal is formed at around $46.5s$ and disappears at around $49.5s$, as expected. It can also be seen that there is a decrease in the core pressure from $48.6s$ to $49.2s$ followed by an increase in the pressure until $50.2s$. This behavior is also observed in the safety factor profile and its opposite in the flux surface averaged toroidal current density profile. It is not observed, however, in the stored energy, see Figure 4.17, in fact on the second increase of the pressure the stored energy decreases. This hints that the decrease in core pressure is accompanied by an increase in the pressure outside of the core and the second increase in the core by a decrease in the rest of the pressure, which can be confirmed by the plot of the

pressure profiles. At $50s$ there is a loss of the pedestal and a faster decrease of the pressure from the core to the boundary of the plasma. It can also be seen that the safety factor never crosses the q=1 line (confirmed by Figure 4.14), which it should not for the majority of the time.

In Figure 4.16 we can see that the plasma current measured by the magnetic diagnostics and the reconstructed one match.

When comparing these results with the graphs in Section 2.4, it can be seen that the times of the first decrease in the core pressure and of the decrease in the NBI and ICH power match. When comparing the pressure profiles from this reconstruction and from Section 4.1, they exhibit the same behaviors.

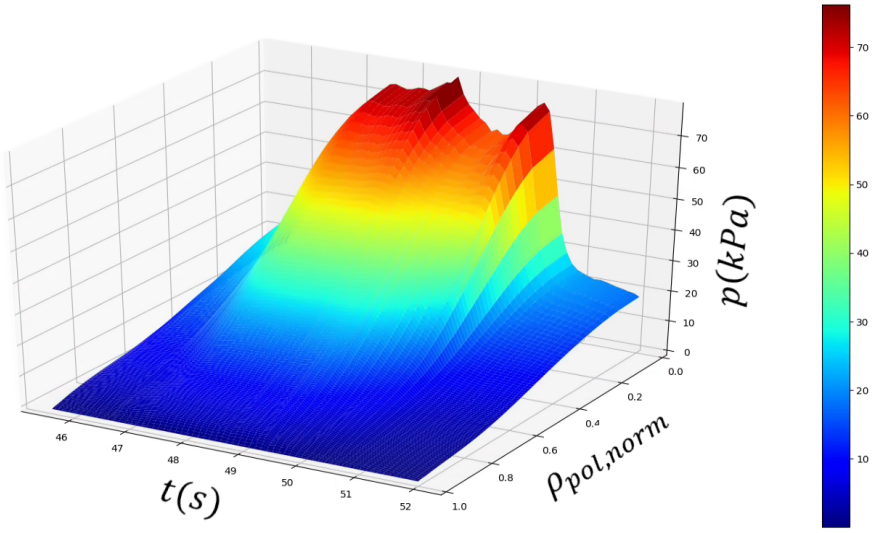

Figure 4.12: Pressure profile obtained from the equilibrium reconstruction using the thermal pressure in function of time and $\rho_{pol,norm}$. Shot = 90198, Run_eq = 2003.

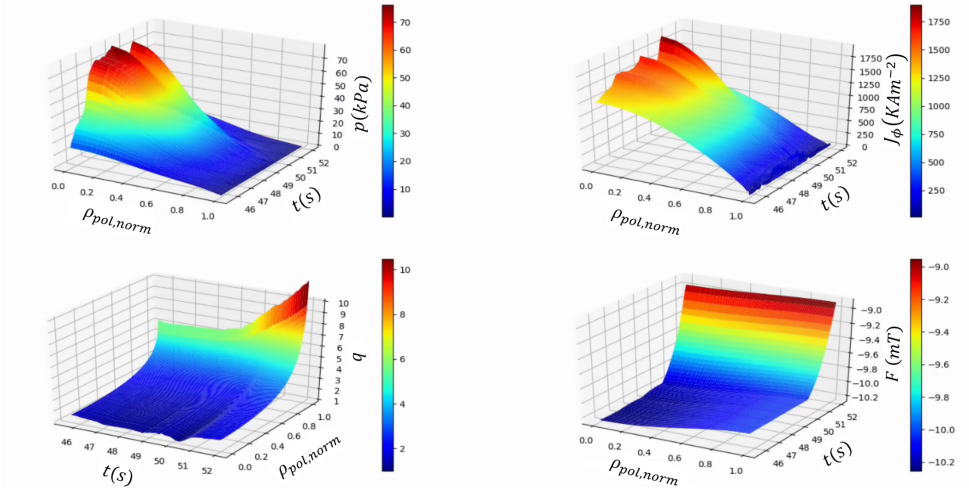

Figure 4.13: On the top left: pressure profile obtained from the equilibrium reconstruction using the thermal pressure in function of time and $\rho_{pol,norm}$. On the top right: the flux surface averaged toroidal current density profile. On the bottom left: The safety factor profile. On the bottom right: the f function profile. Shot = 90198, Run_eq = 2003.

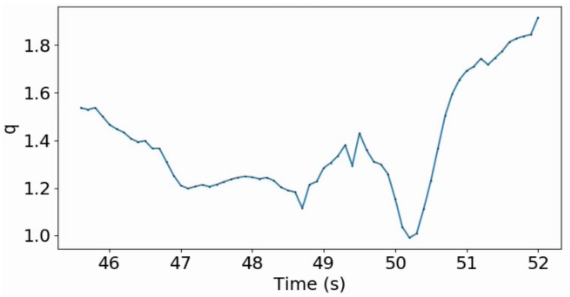

Figure 4.14: Safety factor at $\rho_{pol,norm} = 0$ in function of time. Shot = 90198, Run_eq = 2003.

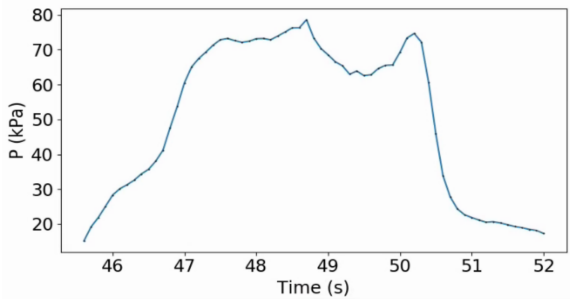

Figure 4.15: Pressure at $\rho_{pol,norm} = 0$ in function of time. Shot = 90198, Run_eq = 2002.

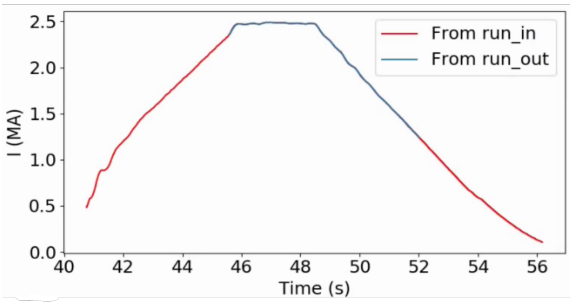

Figure 4.16: Plasma current in function of time. In red the plasma current measured with the magnetic diagnostics and in blue the plasma pressure obtained with the reconstruction. Shot = 90198, Run_eq = 2003.

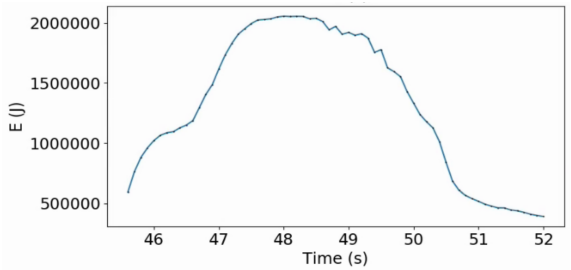

Figure 4.17: Stored energy ($w_{mhd} = \frac{3}{2}\int pdV$) in function of time. Shot = 90198, Run_eq = 2003.

4.4 Heating and current drive workflow testing and calculation of the Total Pressure Profile

In this section, the energetic particle component of the pressure was calculated for the 48.0s time slice. The first step was to use the EQSTABIL RECONSTRUCT AND REFINE workflow to make an equilibrium reconstruction using only the magnetic diagnostics, followed by the calculation of the thermal pressure and a second equilibrium reconstruction. The EQUAL parameters used were the same for both reconstructions and were the same as the ones in Section 4.3. The second step was to calculate a new thermal pressure using the kinetic equilibrium. The third step was using the HEATING AND CURRENT DRIVE workflow to calculate the energetic particle pressure components due to ion cyclotron heating.

In Figures 4.18 to 4.21 the outputs of the workflow are presented. From Figures 4.18 and 4.19 we can see that the ions absorb far more energy from the waves than the electrons, and the hydrogen ions more than the deuterium, as expected.

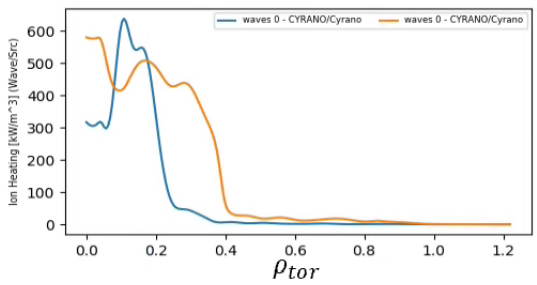

Figure 4.18: Power absorbed by the ions from ICRH waves, calculated by Cyrano. In blue, it's the wave power absorbed by the deuterium. In orange, it's the wave power absorbed by the hydrogen. Shot=90198, Run=2009, Time=48.0s.

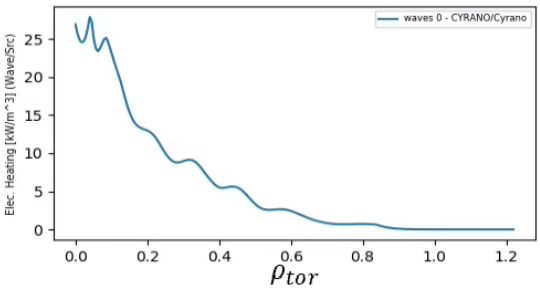

Figure 4.19: ICRH wave power absorbed by the electrons, calculated by Cyrano. Shot=90198, Run=2009, Time=48.0s.

From Figures 4.20 and 4.21 we can see that the big majority of the power absorbed by the electron is transferred to the electrons. The power absorbed by the deuterium ions is transferred to electrons and other deuterium ions and the power absorbed by the hydrogen ions is transferred mostly to electrons and deuterium (hydrogen is a minority species, and so less energy is transferred to hydrogen ions).

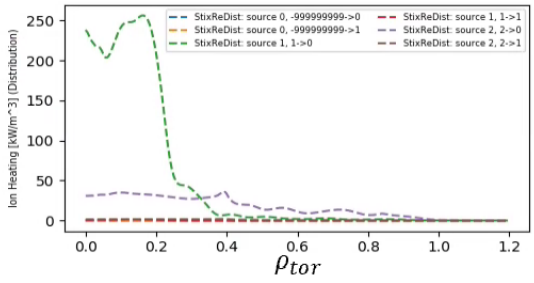

Figure 4.20: Power transferred to the ions by collisions, calculated by the StixReDist code. In blue, from electron to deuterium, in orange, from electrons to hydrogen. In red, from deuterium to hydrogen, in green, from deuterium to deuterium. In purple, from hydrogen to deuterium, and in gray, from hydrogen to hydrogen. Shot=90198, Run=2009, Time=48.0s.

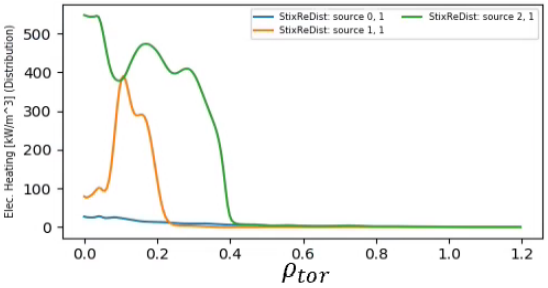

Figure 4.21: Power transferred to the electrons by collisions, calculated by the StixReDist code. In blue, from the electrons, in orange, from deuterium, and in green, from hydrogen. Shot=90198, Run=2009, Time=48.0s.

The contents of the corefast, along with the calculated total pressure before and after the grid change are presented in Figure 4.22. In this figure, we can see that when the ICRH effects are added to the pressure profile, its maximum more than triples. It goes from $70kPa$ (thermal pressure) to $220kPa$ (total pressure). It can also be seen that when interpolating from the corefast and coreprof grid to the

equilibrium grid (the blue and yellow/orange lines respectively) a slight change in the profile for $\rho_{tor} < 0.1$ is introduced. We can also see that the majority of the energy is deposited at the core, $\rho_{tor} < 0.4$ or $\rho_{pol,norm} < 0.45$ but off the axis (the pressure maximum is located at $\rho_{tor} = 0.1$ or $\rho_{pol,norm} = 0.12$.

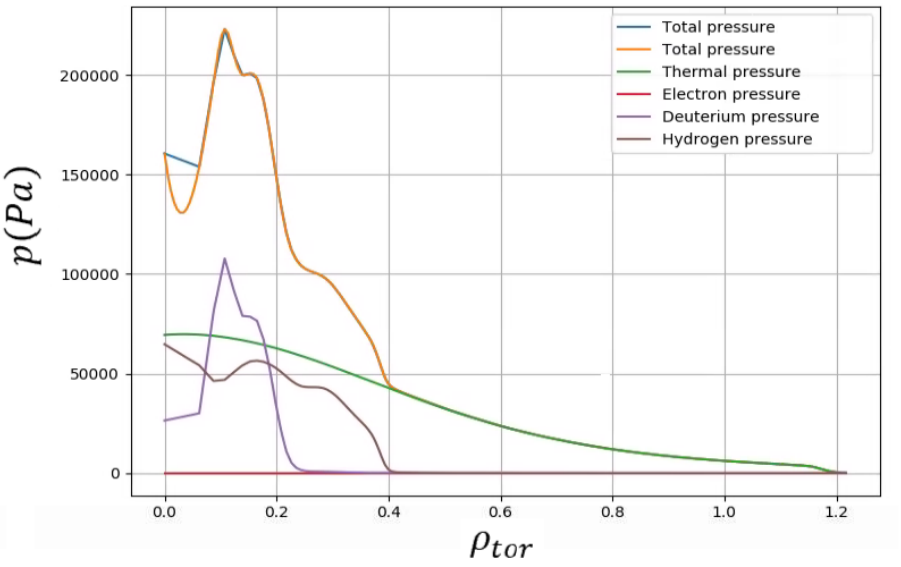

Figure 4.22: Pressure components in function of ρ_{tor}. In red is the electron fast pressure, in brown is the hydrogen fast pressure, in purple is the deuterium fast pressure, in green is the thermal pressure (calculated using the mapped diagnostics into the 2007 equilibrium), in blue is the addition of the previously described components and in orange is its interpolation into the 2007 equilibrium grid. Shot=90198, Run=2010, Time=48.0s.

Then the same process was followed for other time slices. The thermal pressure calculated using the kinetic equilibrium increases from $46.7s$ to $48.0s$ and then it decreases.

In Figure 4.23 the energetic deuterium and hydrogen pressure components are presented (these are referred to as P_{fast} or fast pressure in the figures for convenience). When comparing the deuterium pressure we can see that the maximums are in the same location $\rho_{pol,norm} \sim 0.12$ and that those values increase from $40kPa$ at $46.7s$, to $152kPa$ at $47.1s$ and then decreases until $49.0s$ with $92kPa$, so they do not follow the same behavior as the thermal pressure. It can also be seen that the deuterium pressure spreads to higher $\rho_{pol,norm}$ for $t > 47.5s$. When comparing the hydrogen pressure we can see that the pressure increases until $48.0s$ and only then starts to decrease.

In Figure 4.24, the total pressure profiles are presented. It can be seen that for the other time slices the maximum pressure values are still off-axis at around $\rho_{pol,norm} \sim 0.12$ and that this value increases significantly from $46.7s$ to $47.1s$, while the ICRH power is increasing. In the $47.5s$ and $48.0s$, there is no increase in the maximum pressure but the curve widens. The maximum value decreases at the $49.0s$ as expected since the ICRH power also decreases.

It can be seen that in the region, $0 < \rho_{pol,norm} < 0.1$, a sharp inflection in the profile may occasionally be observed (especially exaggerated at $47.1s$). These are clearly artifacts caused by the interpolation

scheme when changing between the HCD code and core profile radial grids and so these points should not be considered in the reconstruction.

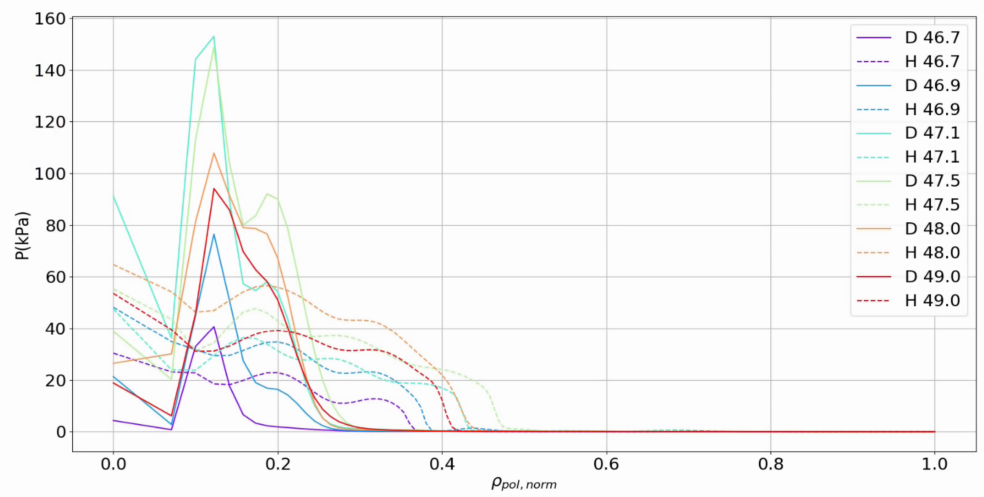

Figure 4.23: Components of the fast pressure in function of $\rho_{pol,norm}$. The full lines correspond to the deuterium fast pressure and the dashed lines to the hydrogen fast pressure. Shot = 90198. Runs = 2503, 2513, 2523, 2533, 2009 and 2543. Times= 46.7, 46.9, 47.1, 47.5, 48.0 and 49.0.

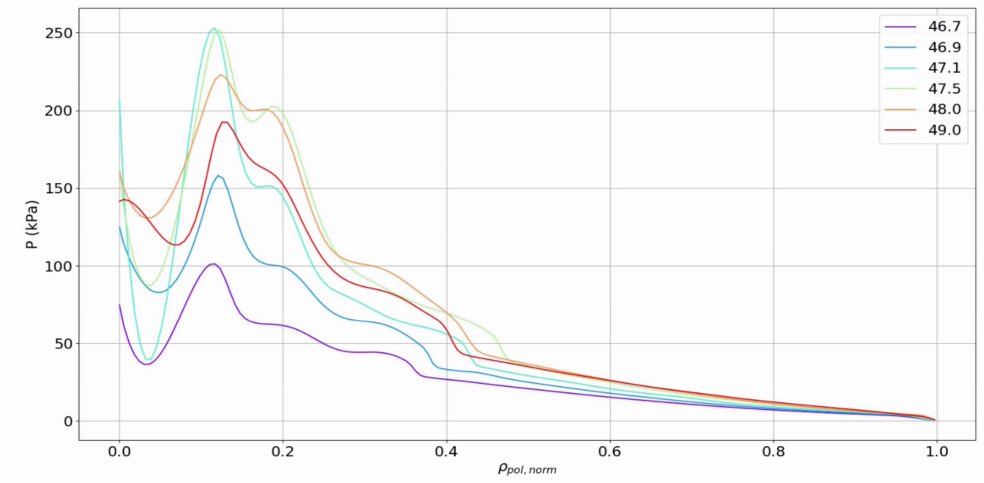

Figure 4.24: Total pressure profiles in function of $\rho_{pol,norm}$. Shot = 90198. Runs = 2504, 2514, 2524, 2534, 2010 and 2544. Times= 46.7, 46.9, 47.1, 47.5, 48.0 and 49.0.

4.5 EQUAL testing with magnetic diagnostics and total pressure profile

In this section, the total pressure obtained in Section 4.4, was used as a constraint in the third equilibrium reconstruction. Different sets of parameters were tested for this pressure profile. While doing these tests it became apparent that getting a reconstructed pressure profile with a positive derivative close to the magnetic axis is extremely difficult.

In the first set of tests, more knots were added especially in the core region, and their individual

weights reduced, along with the constraint weights.

In the second set of tests, the number of grid points was increased to 129, the knots at the core were moved to the points where the pressure derivative has its maxima and minima, the constraint tuneff was changed to 0.5 and the pressure weights were set to 1.0 in the core and pedestal region ($\rho_{pol,norm} < 0.3$ and $\rho_{pol,norm} > 0.9$) and the others were set to 0.3. The individual knot weights were obtained by trial and error (with the aim of getting a good fit to the total pressure profile, good q=1.5 marker values, and a safety factor above q=1). The final parameters are presented in appendix A.3.

In Figures 4.25, 4.26, and in Table 4.3, we can see the reconstructed pressure profile is not very similar to the total pressure profile in the core region, but the fit at the pedestal is still good. We can also see that the safety factor profile is hollow, which it should not be (this could be improved by increasing the regularization parameters, but it would also lead to a worse pressure profile and to the existence of q=1), that it does not cross the $q = 1$ line and that the q error values for the location of the $(m = 3, n = 2)$ mode location (calculated using the methods described in the section 3.10) are high.

In Figure 4.27, the radial positions for deposition of the ICRH power are presented, they were calculated according to Section 3.11 and using the kinetic equilibrium with the thermal pressure (the one used in the heating and current drive workflow). As can be seen only the radial positions that correspond to the first harmonic hydrogen frequency and the second harmonic deuterium frequency are within the plasma boundaries. Their mean R values are $3.12m$, $3.00m$, and $2.98m$. For the second harmonic hydrogen frequency, they are: $7.2m$, $6.5m$, and $6.3m$ and for the first harmonic deuterium frequency, they are: $1.56m$, $1.33m$, and $1.30m$.

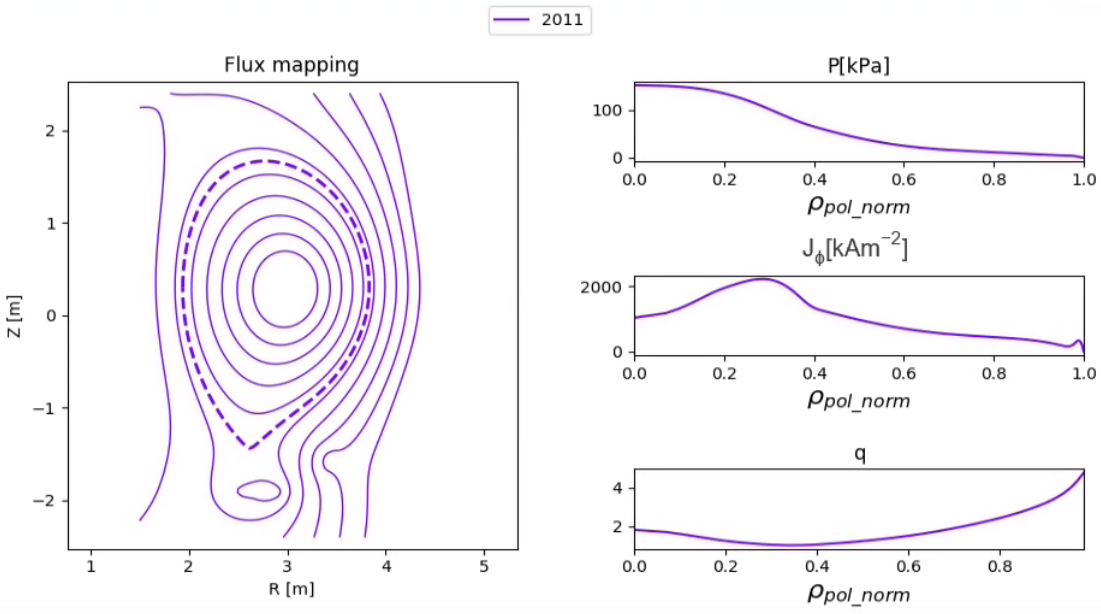

Figure 4.25: On the left: Contour plot of the flux surfaces. On the top right: Pressure profiles. ON the middle right: Flux surface averaged toroidal current density profiles. On the bottom right: Safety factor profiles. Shot = 90198. Run_eq = 2011. Time = 48.0s.

In Figures 4.28 and 4.29 and Table 4.4, the differences between the three reconstructions are presented:

the one using only the magnetic diagnostics (run=2006), the one that uses the thermal pressure profile (run=2007) and the one that uses the total pressure profile (run=2011).

From the first to the second reconstruction, the pressure profile gets the pedestal (characteristic of the H-mode) and the maximum pressure decreases from $109kPa$ to $76kPa$, the flux surface averaged toroidal current density profile also gets an oscillation at the pedestal and its maximum value decreases from $1870kAm^{-2}$ to $1600kAm^{-2}$, the safety factor profile shape does not have significant changes but the error values for $q = 1.5$ are improved, from $\sim 15\%$ to $\sim 2\%$. On average the error values for the magnetic sensors increase.

B_ϕ	R	ψ	q	$R.E(q)$
3.0436	3.3278	3.7816	1.1295	24.7
3.0794	3.2914	3.4449	1.0383	30.8
3.9189	2.5849	4.1171	1.2305	18.0
3.9367	2.5726	4.2152	1.2622	15.9

Table 4.3: EQUAL safety factor value that corresponds to the $n = 2$ and $m = 3$ mode and its error when compared to $q = 1.5$. Obtained according to section 3.10. Shot = 90198. Run = 2011. Time = 48.0s.

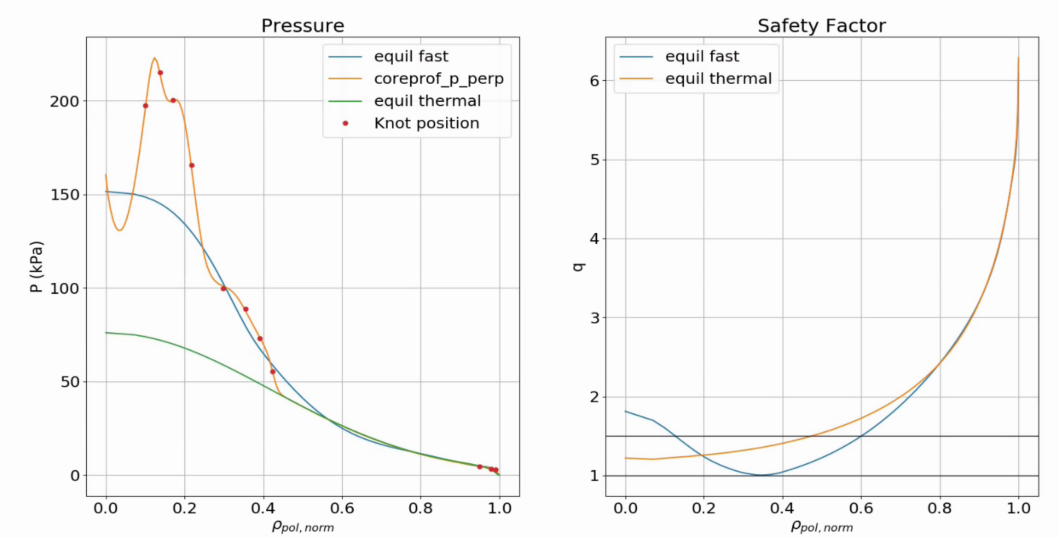

Figure 4.26: On the left: Comparison of the pressure profiles from the second equilibrium reconstruction (using the thermal pressure profile), in green, the third equilibrium reconstruction (using the total pressure profile) in blue, and the total pressure profile in orange. The positions of the knots of the B-spline function are also shown by the red dots. On the right: Comparison of the safety factor from the second (orange) and third (blue) reconstructions. Shot=90198. Run=2011. Time=48.0s.

From the second to the third reconstruction, the maximum pressure increases significantly (it doubles) to $151kPa$, the maximum of the flux surface averaged toroidal current density profile is shifted to an off-axis position and increases to $2240kAm^{-2}$ (at $\rho_{pol,norm} \sim 0.29$), though the axis value decreases to $1050kAm^{-2}$, the safety factor profile changes as well, its minimum is shifted to $\rho_{pol,norm} \sim 0.35$. When

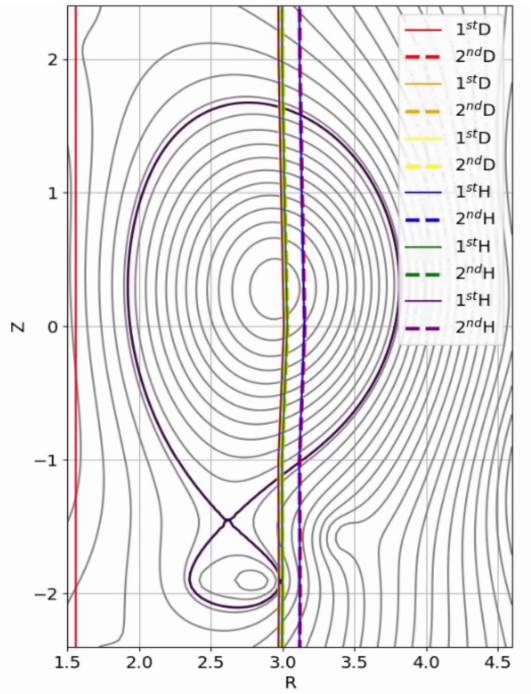

Figure 4.27: Contour plot of the poloidal magnetic flux ψ in R and Z along with the vertical lines with the R position of the deposition of the ICRH power calculated according to section 3.11. Shot=90198. Run=2007. Time=48.0s.

comparing the contour plot of the magnetic surfaces we can see a slight shift to the right.

As can be seen the q errors for the $(m = 3, n = 2)$ mode are better when the thermal pressure is added to the equilibrium reconstruction, but get worse when the total pressure is used. The opposite happens with the magnetic diagnostics errors, the majority gets worse when the thermal pressure is added and then becomes better once the total pressure is used.

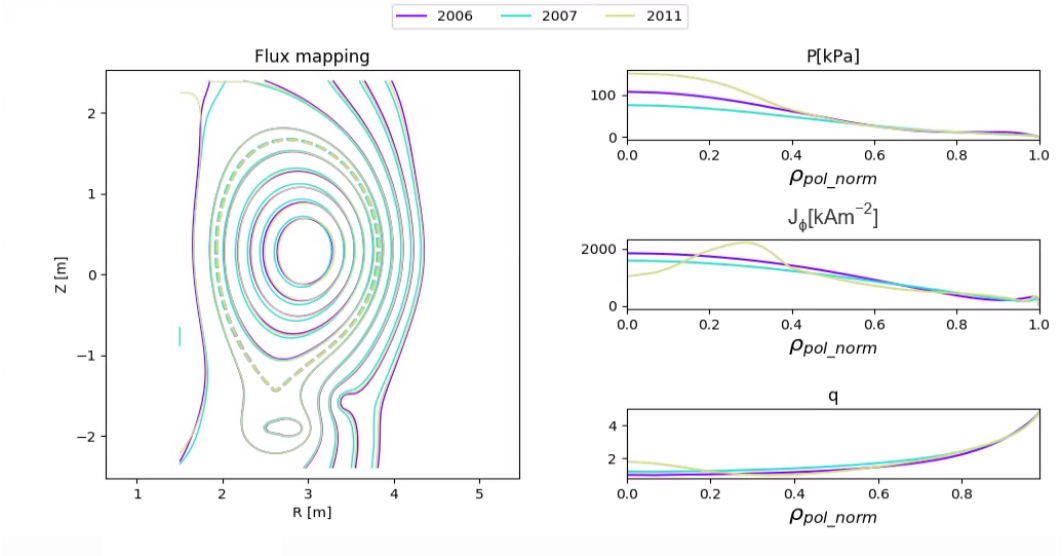

Figure 4.28: On the left: magnetic surface plot on a poloidal cross-section. On the right: pressure profiles (first), flux surface averaged toroidal current density profiles (second) and safety factor profiles (third). The purple, blue, and green colors represent the magnetic, kinetic, and total pressure reconstructions, respectively. Shot=90198. Run=2006, 2007 and 2011. Time=48.0s.

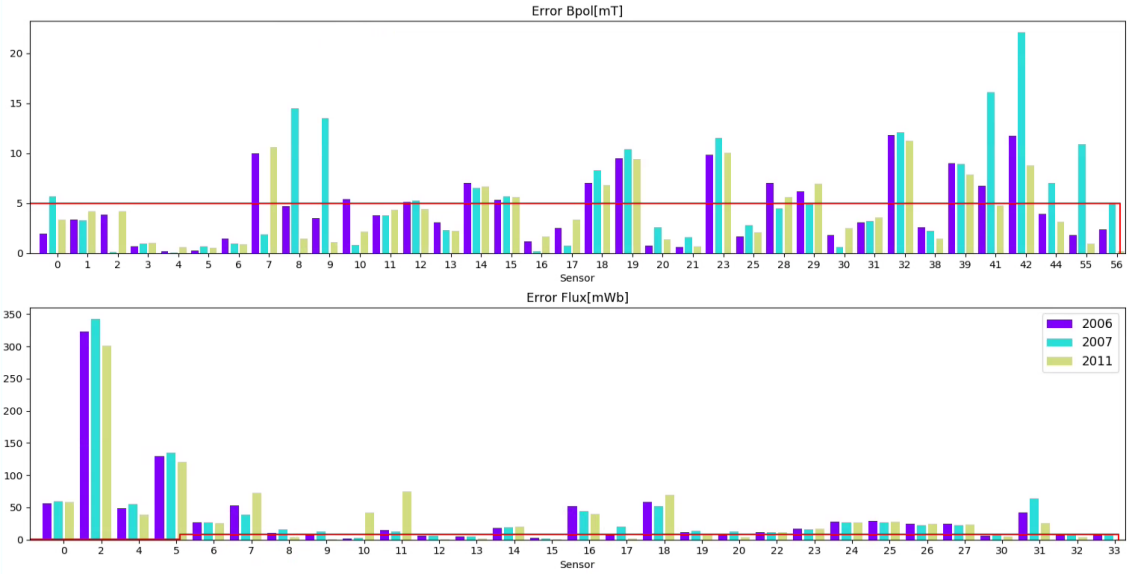

Figure 4.29: On top: error between the reconstructed and measured poloidal magnetic field. On the bottom: magnetic flux error. The purple line corresponds to the magnetic only reconstruction, the blue line to the kinetic reconstruction, and the green line to the reconstruction using the total pressure profile. Shot = 90198. Runs = 2006, 2007 and 20011. Time=48.0.

B_ϕ	R.E(q) 2006	R.E(q) 2007	R.E(q) 2011
3.0436	14.6	2.1	24.7
3.0794	18.4	2.2	30.8
3.9189	15.4	3.4	18.0
3.9367	14.2	2.2	15.9

Table 4.4: EQUAL safety factor error value that corresponds to the $n = 2$ and $m = 3$ mode when compared to $q = 1.5$. Obtained according to section 3.10. Shot = 90198. Runs = 2006,2007,2011. Time = 48.0s.

Next, the same reconstruction was made for the other time slices. As can be seen in Figure 4.24 the shape of the total pressure profiles is similar for all time slices (the points where the derivative has its maximums and minimums have the same location), so the profile parameters were kept the same for all reconstructions. However the pressure weights were changed so that the parts of the profiles where the interpolation should not be considered ($0 < \rho_{pol,norm} < 0.07$) were changed to 0.

The results of the reconstructions are shown in Figure 4.30. We can see that the reconstructed pressure profiles never follow the shape of the total pressure profiles exactly (as with the 48.0s time slice, the reconstructed profiles are decreasing functions). However, the maximum values of the two have the same behavior in time (they increase from 46.7s to 47.5s and then decrease). We can also see that the safety factor profile is monotonic for the 46.7s, 46.9s, and 49.0s time slices (where the total pressure is smaller) but it is hollow for the other time slices. The flux surface averaged toroidal current density profiles either have an off-axis maximum (for the 47.1s, 47.5s, 48.0s, and 49.0s time slices) or a step-like increase for $0 < \rho_{pol,norm} < 0.4$.

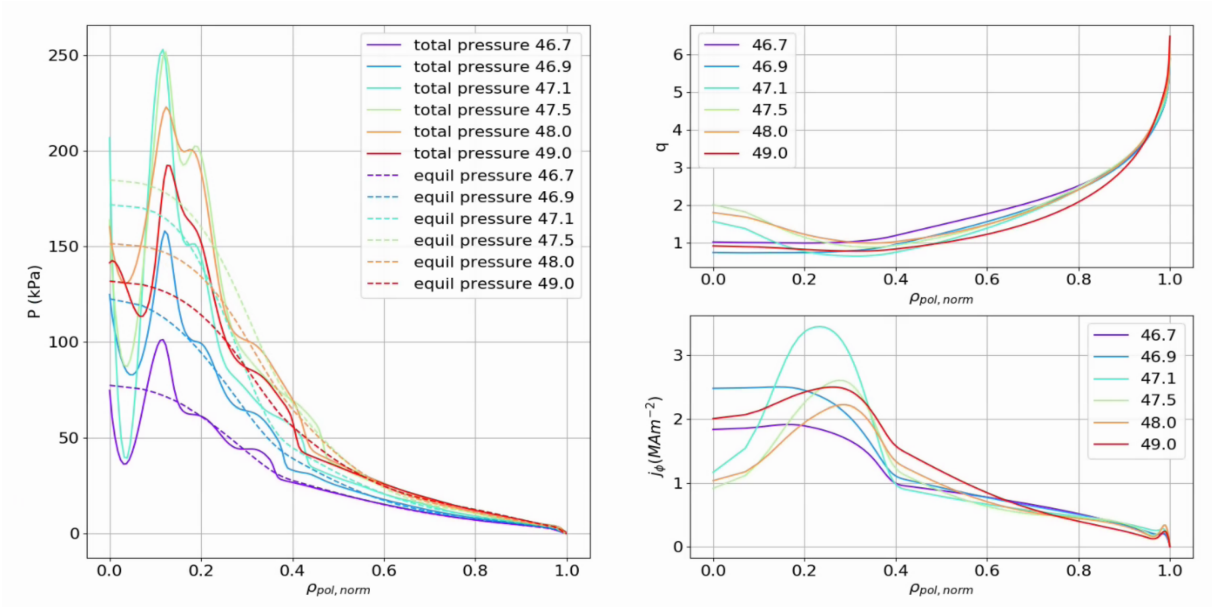

Figure 4.30: On the left: Reconstructed and total pressure profiles. On the top right: reconstructed safety factor profiles. On the bottom right: reconstructed flux surface averaged toroidal current density profiles. Shot=90198. Run_tot=2504, 2514, 2524, 2534, 2010, 2544. Run_eq= 2506, 2517, 2527, 2537, 2011, 2545. Time=46.7, 46.9, 47.1, 47.5, 48.0, 49.0.

4.6 Total pressure using different kinetic equilibrium reconstructions

As stated in Section 3.7 from the Methods Chapter, to see how different kinetic equilibrium reconstructions (using suitable pressure constraint weight distribution to mimic fitting different radial domains of the pressure profile) affect the calculation of the total pressure, first a reconstruction was made using the parameters in appendix A.1. Then the thermal pressure profile was calculated by mapping the Thomson diagnostics, which can be seen in Figure 4.31.

Then seven different equilibrium reconstructions were made, their only difference being the pressure weights see appendix A.4.

Figures 4.31 and 4.32 and Table 4.5 show the differences between these reconstructions. As expected when all weights are set to 1.0, the fit to the pressure profile is the best and the magnetic diagnostics errors are the worst (in general). The two last reconstructions have a bad fit at the pedestal, the worst $q = 1.5$ error values and the smallest error values for the magnetic diagnostics. The reconstruction with the best $q = 1.5$ error values is c, which has the weights set to 1.0 for $\rho_{pol,norm} > 0.80$ only.

B_ϕ	2012	a - 2014	b - 2015	c - 2016	d - 2017	e - 2018	f - 2019	g - 2020
3.0436	12.3	1.2	4.5	0.2	3.2	2.5	5.2	15.0
3.0794	9.4	3.2	8.0	3.5	0.07	6.3	9.1	18.8
3.9189	12.7	5.9	6.5	1.6	2.2	3.6	6.3	16.0
3.9367	13.7	4.8	5.4	0.6	3.1	2.4	5.2	14.6

Table 4.5: EQUAL safety factor error value that corresponds to the $n = 2$ and $m = 3$ mode when compared to $q = 1.5$. Obtained according to Section 3.10. Shot = 90198. Runs = 2014,2015,2016,2017,2018,2019 and 2020. Time = 48.0s.

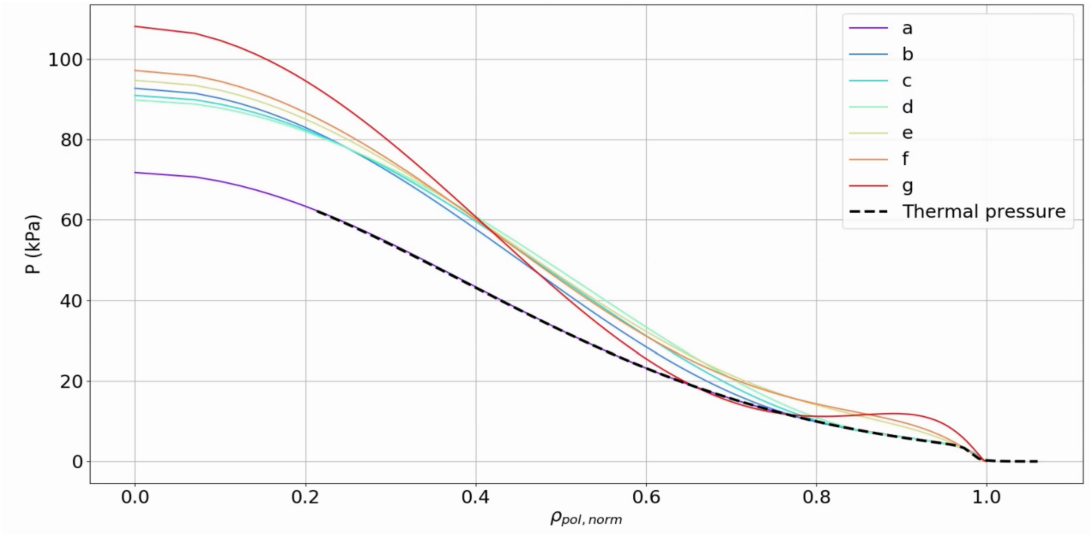

Figure 4.31: Pressure profiles from the second equilibrium reconstruction (kinetic) and the thermal pressure profile used in that reconstruction. Shot = 90198. Runs = 2013, 2014, 2015, 2016, 2017, 2018 , 2019 and 2020. Time= 48.0s.

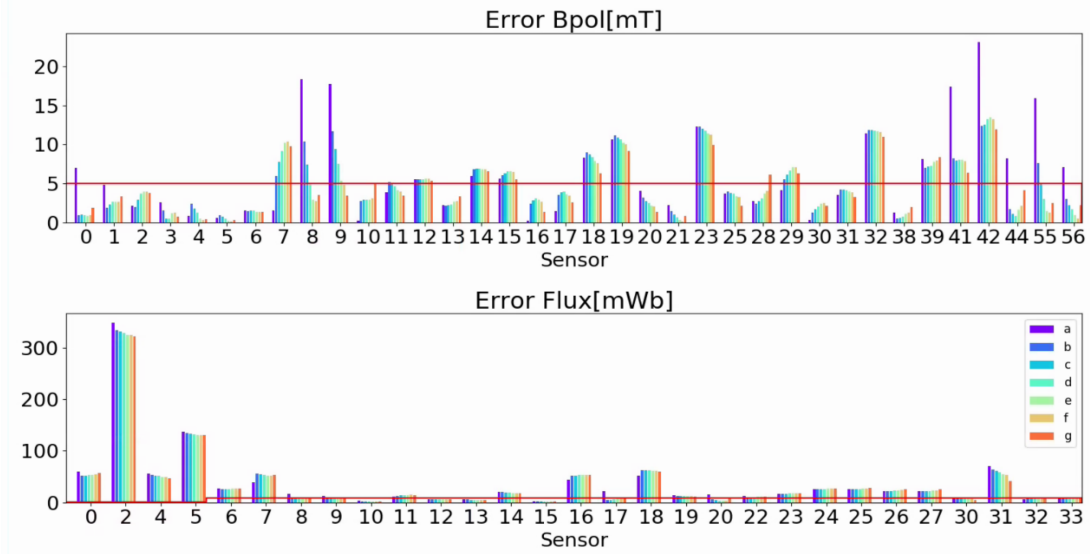

Figure 4.32: On top: error between the reconstructed and measured poloidal magnetic field. On the bottom: magnetic flux error. Shot = 90198. Runs = 2013, 2014, 2015, 2016, 2017, 2018 , 2019 and 2020. Time= 48.0s.

With these reconstructions, the R values for the deposition of the wave are described in Table 4.6. As can be seen the values for the R position of the first harmonic frequencies for the hydrogen ions and second harmonic frequencies for the deuterium ions are the same for all the reconstructions.

In Figure 4.34 we can see that the pressures due the energetic hydrogen ions are very similar for all reconstructions (c and d go to zero are shifted slightly to the left) and the differences in the total pressure profiles, seen in Figure 4.33 come mostly from the differences in the energetic deuterium pressure and the thermal pressure profiles.

Figure 4.33 presents the total pressure profiles obtained. It can be seen that the c and d are very similar ($weight = 1$ for $\rho_{pol,norm}$ bigger than 0.8 and 0.9), b, e and f are similar ($weight = 1$ for $\rho_{pol,norm}$ bigger than 0.75, 0.95 and 0.97), and that the a (all ones) profile is similar to the one in section 4.4 (all 0.95), as expected.

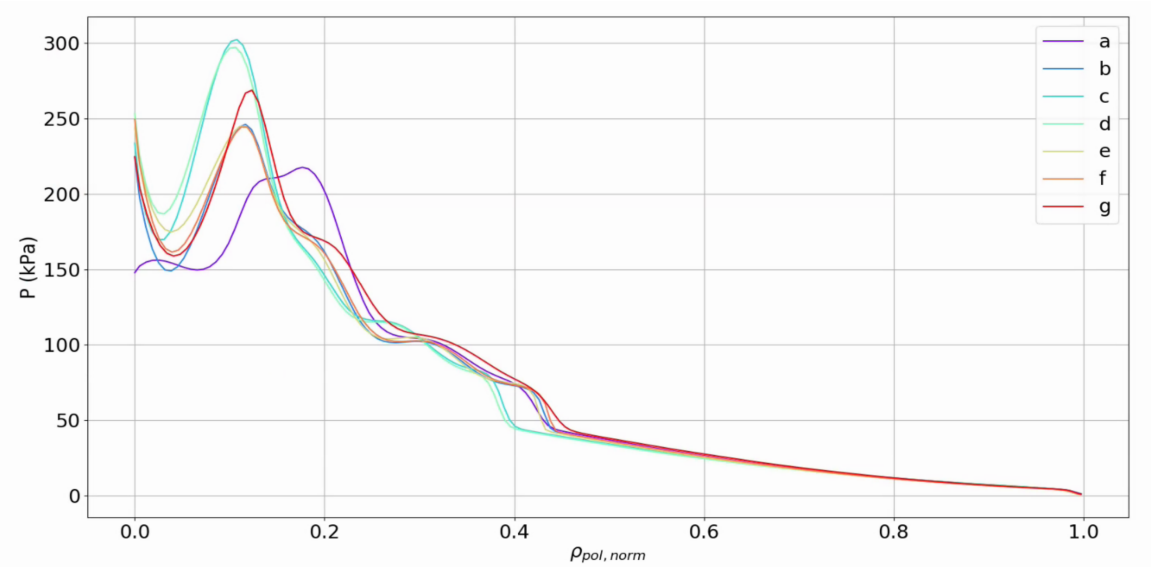

Figure 4.33: Total pressure profiles . Shot = 90198. Runs = 2035, 2036, 2037, 2038, 2039 , 2040 and 2041. Time= 48.0s.

	a (2014)	b (2015)	c (2016)	d (2017)	f (2018)	g (2019)	h (2020)
$R_1(m)$	3.125	3.125	3.125	3.125	3.124	3.124	3.124
$R_2(m)$	3.003	3.003	3.003	3.003	3.003	3.003	3.003
$R_3(m)$	2.980	2.980	2.980	2.980	2.980	2.980	2.980

Table 4.6: R position of the deposition of the ICRH deposition power deuterium ions and for the hydrogen ions. Shot = 90198. Runs = 2014,2015,2016,2017,2018,2019 and 2020. Time = 48.0s.

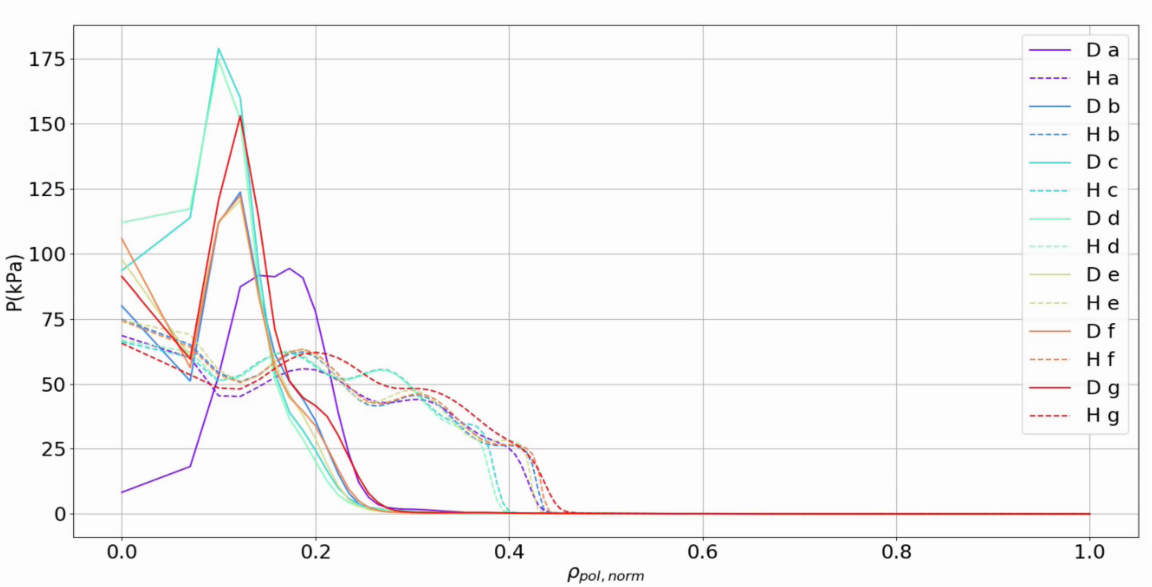

Figure 4.34: Fast pressure components for deuterium (D) and hydrogen (H) ions. Shot = 90198. Runs = 2028, 2029, 2030, 2031, 2032 , 2033 and 2034. Time= 48.0s.

Then the total pressure profiles were used in a third equilibrium reconstruction. Since some of the profiles are very similar, only four of those were chosen for the reconstructions. The ones chosen were: a, b, d and g (in Figure 4.34).

In order to make the third equilibrium reconstruction, several parameters were tried and the best one was chosen. The main differences between the various attempts were the number of knots (some of the knots that had smaller absolute values of the pressure derivative were removed) and the pressure weights at the core: in some all weights were set to 1 up to the outer boundary of the energetic ion pressure contribution ($\rho_{pol,norm} < 0.4$), in others only the main peak ($\rho_{pol,norm} < 0.2$) and in others only the growing part of the profile ($\rho_{pol,norm} < 0.1$).

A combination of the shapes of the pressure profile (how it fits to the total pressure and pedestal), safety factor shape and error values and whether or not it crosses the q=1 line, the current density shape and magnetic diagnostic error were used as criteria to choose between the reconstructions. The first iteration of the pressure profiles and their corresponding equilibrium reconstruction are presented in Figure 4.35.

As before, getting a pressure profile with the same shape as the total pressure was not possible (the reconstructed pressure profiles are still decreasing functions), but for the 'b' (similar to 'f' and 'e' and so for $\rho_{pol,norm} > 0.75, 0.95, 0.97$ respectively) case it was possible to get safety factor and flux surface averaged toroidal current density profiles without the off-axis minimum and maximum, although the safety factor profile crosses the $q = 1$ line. In this case, the values of the $q = 1.5$ error are far better than in the other reconstructions (although still worse than the thermal reconstruction), see Table 4.7 . In all the cases the q=1.5 errors worsen and the magnetic errors get better when compared to the kinetic equilibrium reconstruction. The parameters used are once again in appendix A.5.

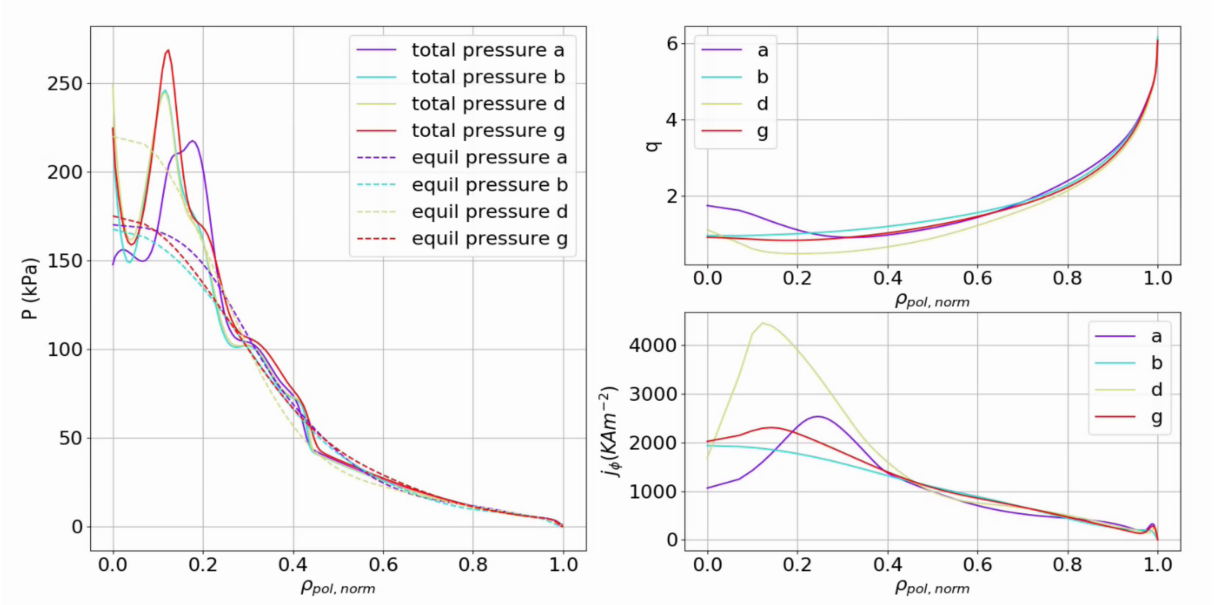

Figure 4.35: On the left: Total and equilibrium pressure profiles. On the top right: safety factor profile. On the bottom right: Flux surface averaged toroidal current density profile. Shot=90198, Runs_tot=2035, 2038, 2040, 2041, Runs_eq=2042, 2043, 2044, 2045, Time=48.0.

B_ϕ	a - 2042	b-2044	d - 2043	g - 2045
3.0436	32.9	13.9	28.7	23.4
3.0794	41.2	18.9	38.1	32.2
3.9189	30.3	10.6	28.3	26.4
3.9367	28.2	9.0	25.4	23.8

Table 4.7: EQUAL safety factor error value that corresponds to the $n = 2$ and $m = 3$ mode when compared to $q = 1.5$. Obtained according to Section 3.10. Shot = 90198. Runs = 2042,2043,2044,2045. Time = 48.0s.

4.7 EQUAL testing with two iterations of the total pressure

In this section of the thesis, a fourth equilibrium reconstruction was made using a second version of the total pressure profile.

The new total pressure profiles were calculated using the third equilibrium reconstructions (the ones made using the first version of the total pressure). They are shown in Figure 4.36. As can be seen for 'a', 'b' and 'g' cases the new total pressures are closer to being decreasing functions and have their maximums at the magnetic axis. The values are also higher than for the previous iteration. For the 'a', the maximum pressure value for the third equilibrium reconstruction (off-axis) is $220kPa$ and the maximum value for the fourth is $350kPa$. For the 'b', it goes from $250kPa$ to $320kPa$. For the 'g', it increases from $270kPa$ to $320kPa$.

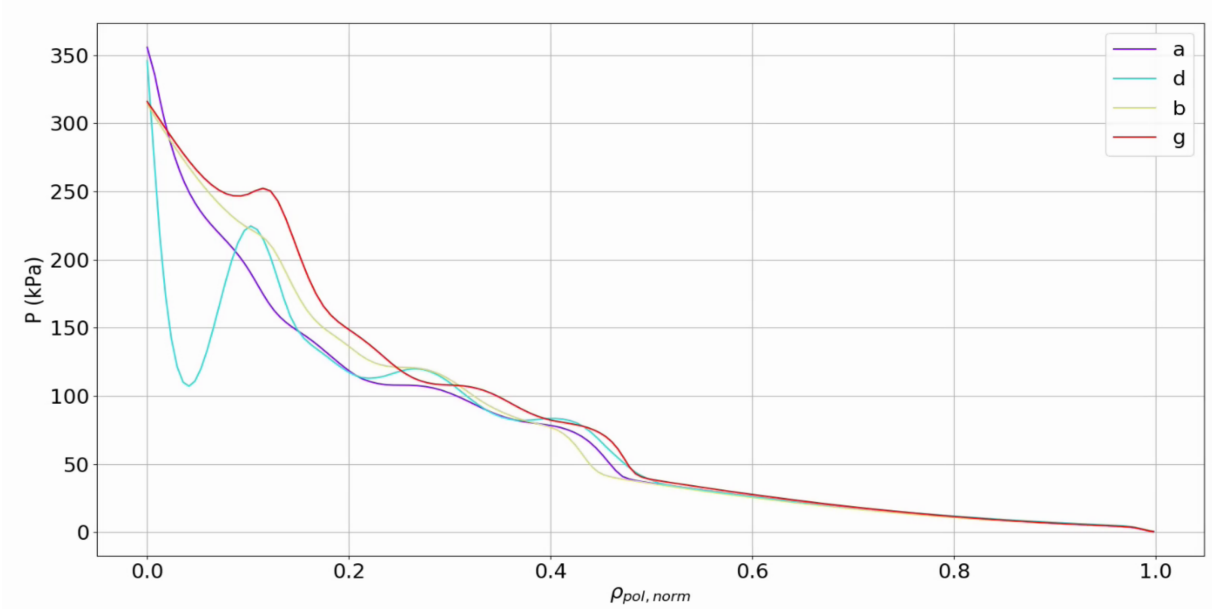

Figure 4.36: Total pressure profiles using the third equilibrium reconstruction. Shot=90198, Runs= 2054, 2055, 2056, 2057. Time=48.0.

So the fourth equilibrium reconstructions were made for the 'a' and 'b' total reconstructions.

Next, there is a description/comparison of the 4 iterations of equilibrium reconstructions: the first using only the magnetic diagnostics, the second using the thermal pressure profile, the third using the total pressure profile and the fourth using the second calculation of the total pressure for 'a' case (the one where all the thermal pressure profile points were used in the second equilibrium reconstruction).

In Figure 4.37 we can see the various pressure profiles. The equilibrium pressure profiles change significantly with each iteration. The first reconstructed equilibrium does not have the pedestal and its maximum value is $89kPa$, the second reconstructed equilibrium has a pedestal and its maximum value drops to $72kPa$ (since all the thermal pressure profile points are used in the reconstruction), the thermal pressure profile and the reconstructed one are a very close match. The third reconstructed equilibrium also has a pedestal and its maximum value doubles to $170kPa$, this profile is not very similar to the one used as a constraint at the core. The fourth equilibrium, once again still has the pedestal and the maximum increases again to $290kPa$, this profile matches much better to the total pressure profile used as a constraint (since it is a decreasing function).

On the right plot of the same figure, we can see how the different equilibriums affect the mapping and calculation of the thermal pressure profile. The first profile only has the values where measurements exist, the second and third ones have fitted values at the core (since their values were needed to calculate the total pressure). We can see that for the same value of pressure (same electron density and temperature, same data point, same R and Z), from the first to the second mapping, the values are shifted to the right (bigger $\rho_{pol,norm}$) and form the second to the third there is a shift to the left (to a smaller value of $\rho_{pol,norm}$). These shifts can be explained either by fitting errors or by the geometry, different positions of the flux surfaces in each equilibrium used by the mapping.

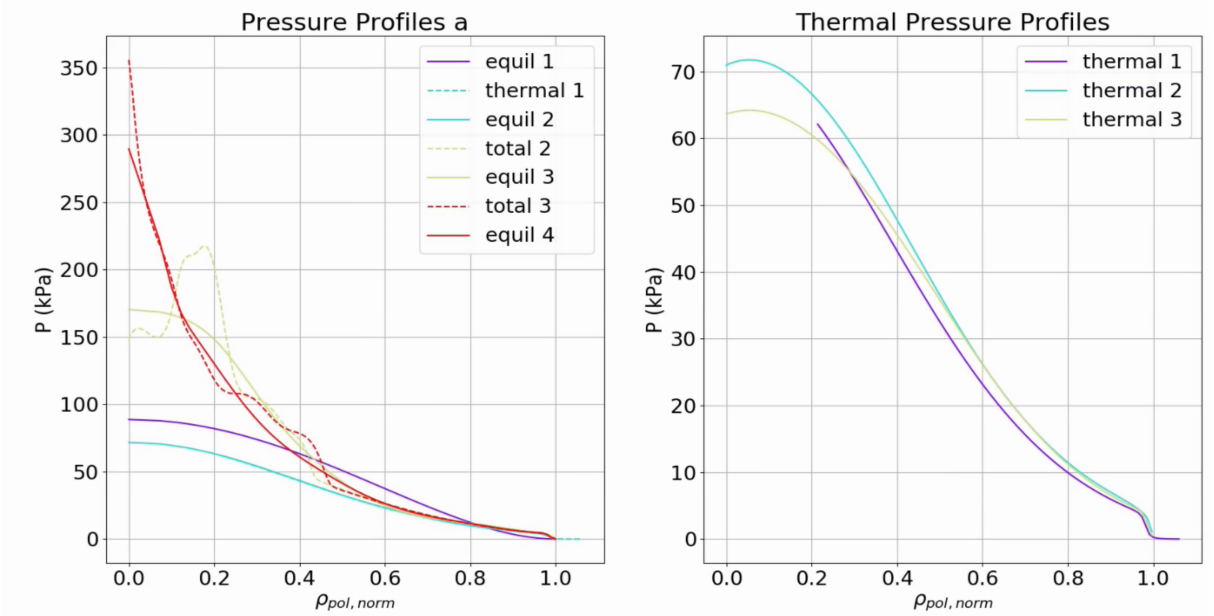

Figure 4.37: On the left: Pressure profiles from the equilibrium reconstructions and the profiles used as constraints. On the right: Thermal pressure profiles determined using the HRTS diagnostic and the first three reconstructions. Name = a. Shot=90198, Runs_eq= 2012, 2014, 2042, 2058. Runs_thermal= 2013, 2021, 2046. Runs_constraint = 2013, 2036, 2054. Time=48.0.

By looking at Figure 4.38, it can be seen that the positions of the flux surfaces do change in each iteration, getting more similar as they reach the boundary (which also happens in the thermal profiles, their differences are mostly on the core region). From the first to the second equilibrium the surfaces shift to the left and from the second to the third they shift to the right. So (from the second to the third equilibrium) the same point in (R,Z), the same value of pressure, corresponds to a surface closer to the axis, so a smaller value of $\rho_{pol,norm}$, and so there is a shift of that point to the right. These differences in the equilibrium and thermal profiles can explain the different deposition of the ICRH waves simulated by the codes, therefore, the different total pressure profiles. It can also be noted that from the third to the fourth reconstructions, the flux surfaces get much smaller, and so it's hard to see if there is any shift of the surfaces.

In Figure 4.39 we can see the differences between the safety factor and flux surface averaged toroidal current density profiles on the various iterations. The flux surface averaged toroidal current density, of the second equilibrium reconstruction, has a similar shape to the first one for most $\rho_{pol,norm}$ (with a smaller value at the axis $1.64 \times 10^6 A/m^2$ instead of $1.29 \times 10^6 A/m^2$) with the exception of the pedestal region. As before, in the third reconstruction, the maximum of the profile leaves the axis to $\rho_{pol,norm} = 0.25$ with a value of $2.55 \times 10^6 A/m^2$ which is not the expected shape. In the fourth equilibrium, the minimum goes back to the axis with a value of $4.53 \times 10^7 A/m^2$ which is much bigger than expected. The plasma current remains very similar for all four reconstructions at $\sim 2.46 \times 10^6 A$.

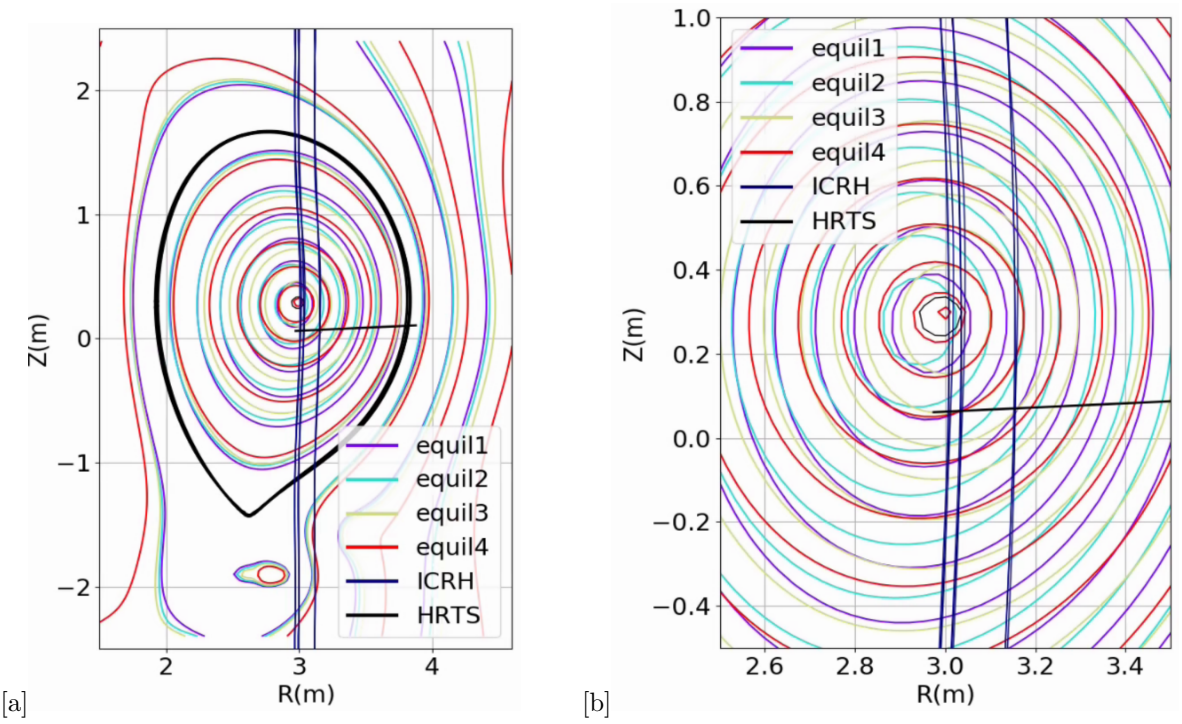

Figure 4.38: Contour plot of the flux surfaces for the four iterations of equilibrium reconstructions [a] and its zoom [b]. Name = a. Shot=90198, Runs_eq= 2012, 2014, 2042, 2058. Time=48.0.

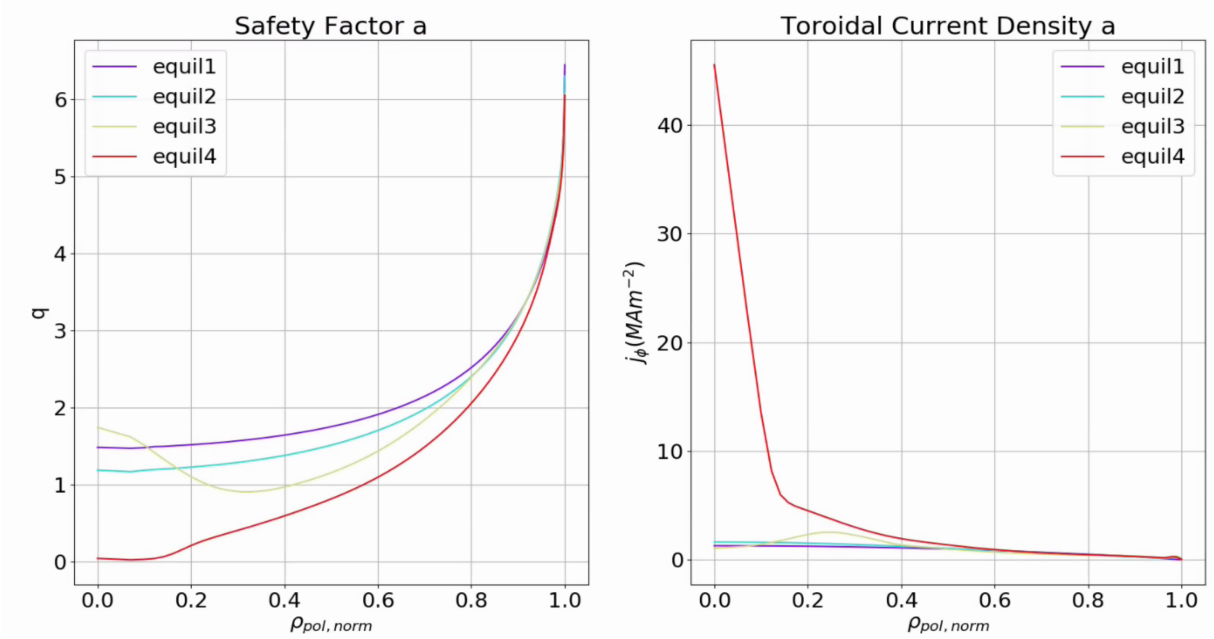

Figure 4.39: On the left: Safety factor profiles from the four reconstructions. On the right: Flux surface averaged toroidal current density profiles four the four reconstructions. Name = a. Shot=90198, Runs_eq= 2012, 2014, 2042, 2058. Time=48.0.

We can also see the differences in the shape of the safety factor profile, the first and second profiles have a similar shape (a decreasing function that does not cross $q = 1$ line) with different axis values (1.49

and 1.19) but as can be seen by Table 4.8, the second one has better error values for $q = 1.5$. For the other two reconstructions, the error values get progressively worse, and both cross the $q = 1.0$ line. Their shapes are different however, the third has an off-axis maximum and the fourth goes very close to zero for $\rho_{pol,norm} < 0.2$.

The error between the magnetic measurements and reconstructed values, in general, get worse from the first to the second reconstruction, then get better for the third reconstruction and worsen again for the fourth reconstruction.

B_ϕ	q error (2012)	q error (2014)	q error (2042)	q error (2058)
3.0436	12.3	1.2	29.1	26.7
3.0794	9.4	3.2	35.5	34.2
3.9189	12.7	5.9	20.0	31.5
3.9367	13.6	4.8	17.8	29.1

Table 4.8: EQUAL safety factor error value that corresponds to the $n = 2$ and $m = 3$ mode when compared to $q = 1.5$. Obtained according to section 3.10. Name = a. Shot = 90198. Runs_eq = 2012, 2014, 2042, 2058. Time = 48.0s.

For the 'b' version of the four iterations (the one where only the pedestal region of the thermal pressure profile is used in the second equilibrium reconstruction, and so, the part of the profile that would not be changed when adding the energetic particle pressure components) there are some differences to the 'a' version (all the points of the thermal profile used).

The difficulty in getting a pressure profile close to the total one for the third iteration is present and it also improved in the fourth iteration. Since the more inner values of the weights for thermal pressure were set to 0, the pressure profiles of the first and second iterations are more similar in the core region. The thermal pressure profiles made with the first, second and third equilibriums do not change as much as the 'a' and the shift of the flux surfaces is less pronounced, as can be seen in Figures 4.40 and 4.42.

The magnetic errors between the first and second iterations are closer. The safety factor and flux surface averaged toroidal current density for the third iteration are much better than for the 'a' version, with no off-axis maximums and minimums, although the safety factor profile still crosses the $q = 1$. The errors for $q = 1.5$ are not as bad, as can be seen in Figure 4.41 and Table 4.9. The fourth reconstruction profiles are not as physically awkward, but they are still very odd, with the safety factor approaching zero on the axis, the value of the flux surface averaged toroidal current density is still much larger but is half of the 'a' version.

B_ϕ	q error (2012)	q error (2015)	q error (2044)	q error (2060)
3.0436	12.3	4.5	13.9	37.9
3.0794	9.4	8.0	18.9	46.4
3.9189	12.7	6.5	10.6	37.9
3.9367	13.6	5.4	9.0	34.9

Table 4.9: EQUAL safety factor error value that corresponds to the $n = 2$ and $m = 3$ mode when compared to $q = 1.5$. Obtained according to section 3.10. Name = b. Shot = 90198. Runs_eq = 2012, 2019, 2044, 2060. Time = 48.0s.

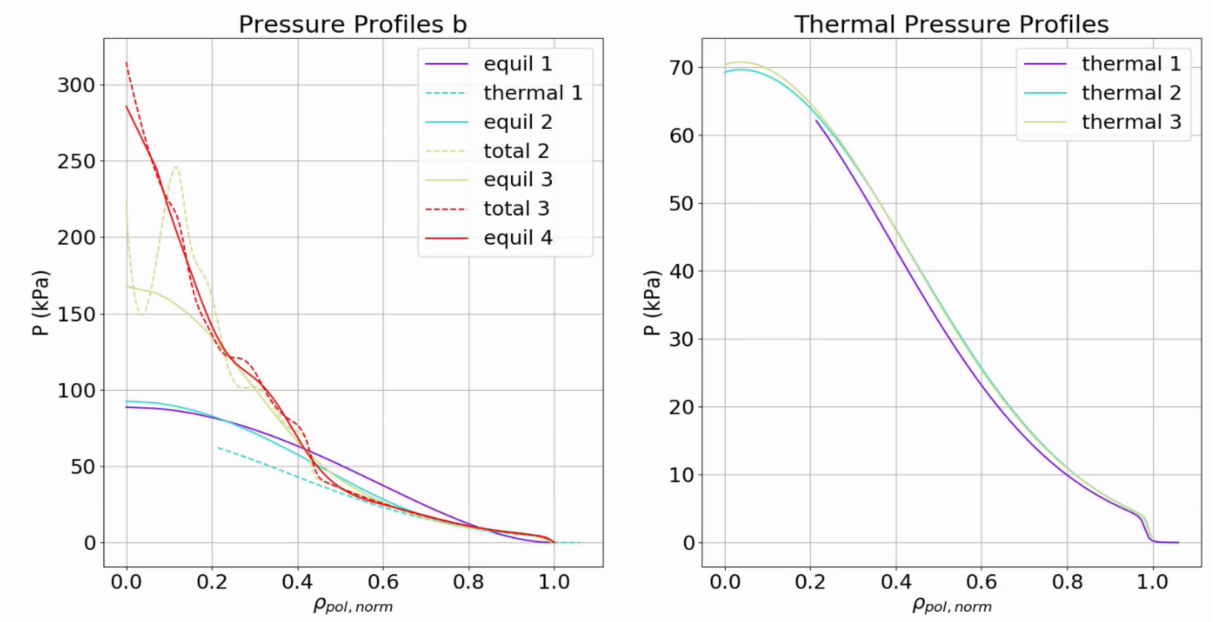

Figure 4.40: On the left: Pressure profiles from the equilibrium reconstructions and the profiles used as constraints. On the right: Thermal pressure profiles determined using the HRTS diagnostic and the first three reconstructions. Name = b. Shot=90198, Runs_eq= 2012, 2015, 2044, 2060. Runs_thermal= 2013, 2026, 2048. Runs_constraint = 2013, 2036, 2056. Time=48.0.

Comparing the second and first iteration of the total pressure profile, we find that the second tends to be more spiked than the first, the wave deposition happens closer to the magnetic axis, see Figures 4.35 and 4.36.

The result of heating and current drive workflow depends on the flux map and on the R where the resonance happens. This R does not change very much in each iteration, since the toroidal magnetic field does not change. We can see in Figures 4.38 and 4.42, that when calculating the total pressure for the first time (considering the second equilibrium), the R lines are to the right of the magnetic axis. When using the total pressure in the next equilibrium reconstruction, the pressure increases and so the flux surfaces would move to the right (due to a bigger Shafranov shift) and so the magnetic axis gets closer to the points of resonance. Therefore when calculating the new total pressure, the wave deposition is

closer to the magnetic axis allowing for the more spiked profiles, which lead to a bigger pressure in the equilibrium reconstruction, and so on. We would predict that the magnetic axis will tend toward the resonant R.

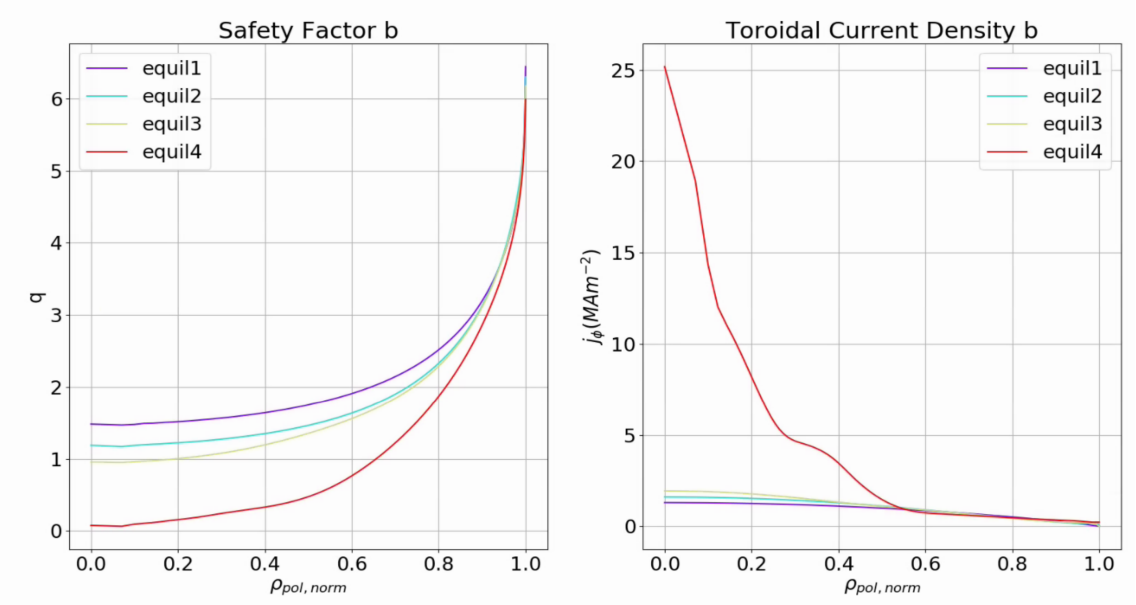

Figure 4.41: On the left: Safety factor profiles from the four reconstructions. On the right: Flux surface averaged toroidal current density profiles four the four reconstructions. Name = b. Shot=90198, Runs_eq= 2012, 2015, 2044, 2060. Time=48.0.

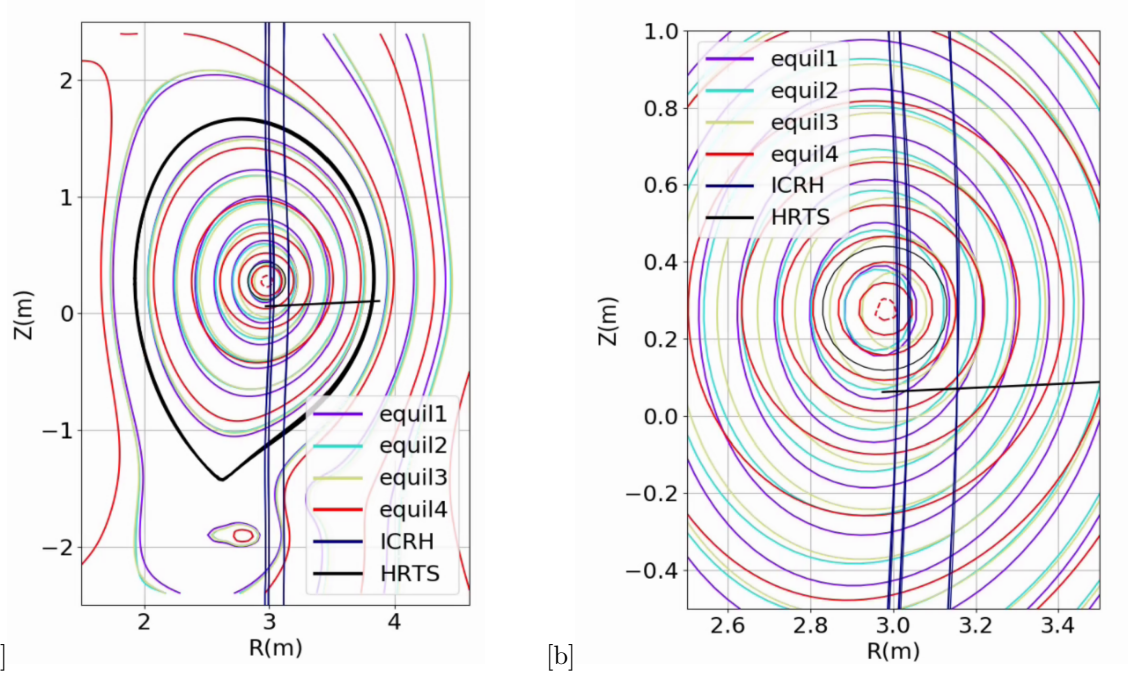

[a] [b]

Figure 4.42: Contour plot of the flux surfaces for the four iterations of equilibrium reconstructions [a] and its zoom [b]. Name = b. Shot=90198, Runs_eq= 2012, 2015, 2044, 2060. Time=48.0.

4.8 EQUAL testing with polarimetry and interferometry

In the results of a previous section (Section 4.5), it was concluded that when using the total pressure profile as a constraint in the equilibrium reconstruction, it is much more difficult to get an agreement between the reconstructed pressure profile and the target one, given that the ICRH heating contribution yields a significant energetic ion pressure at the deep core of the plasma ($\rho_{pol,norm} < 0.3$) where there is no additional information available to constraint the equilibrium calculation. When using only the total pressure profile, the FF' profile is free to change and so, the flux surface averaged toroidal current density and safety factor profile become hollow.

Thus, in this section, the data from the polarimetry and interferometry diagnostics, Faraday rotation angle and integrated density, were added to the previously done reconstructions. The channels used were the 3, 5 and 7 as mentioned in Section 3.9 in the Methods chapter.

First, they were added to the magnetic reconstruction with weights 0.1, 0.2 and 0.3, they were found to flatten the pressure and current density profiles (the core values were decreased and the values next to the pedestal slightly increased), the values of the safety factor also increased. When comparing the magnetic sensor errors they seem to become worse on average and the safety factor error values in the $m = 3$ and $n = 2$ mode position worsen. The 0.1 weights were found to be the best, the comparison between this reconstruction and the one without the Faraday rotation angle and integrated density can be seen in Figure 4.43 and the $q = 1.5$ error in Table 4.10. Then the 0.1 weight parameters were used to make the reconstruction from $46.0s$ to $52.0s$.

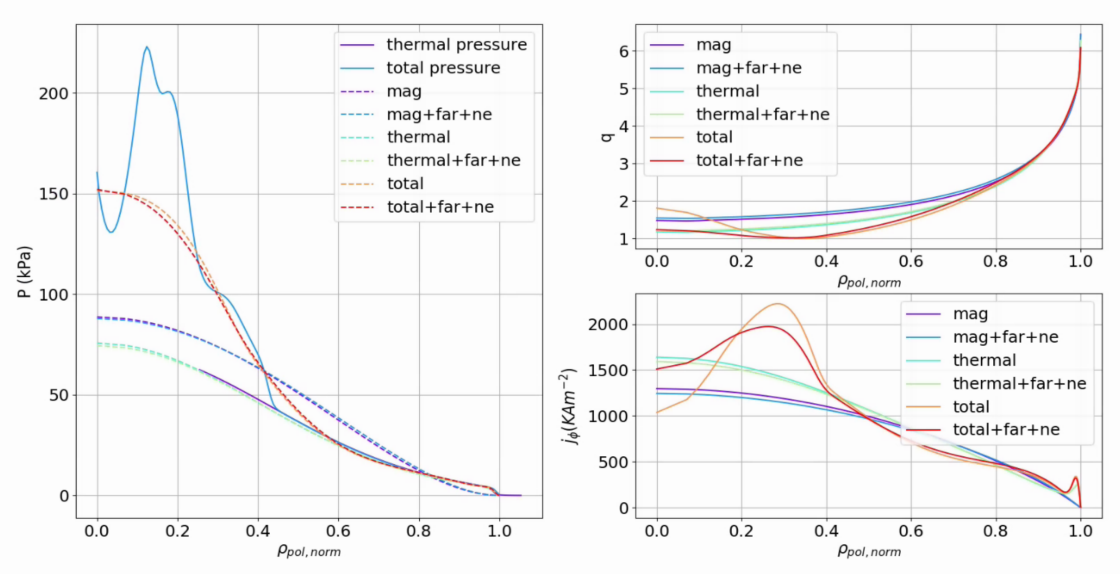

Figure 4.43: On the left: Total and equilibrium pressure profiles. On the top right: safety factor profile.On the bottom right: Flux surface averaged toroidal current density profile. Shot=90198, Runs_eq=2650, 2651, 2660, 2661, Time=48.0.

Then they were added to the kinetic reconstruction using the thermal pressure profile with weights 0.1, 0.2 and 0.3. The reconstruction using the 0.1 weights has profiles that are very similar to the one that does not have the Faraday rotation angle and integrated density as constraints, but the safety factor error values in the $m = 3$ and $n = 2$ mode position improve, as can be seen in Figure 4.43 and in Table

4.10. For the other reconstruction the pressure and flux surface averaged toroidal current density core values decrease and the safety factor increase, the magnetic error worsen and the $q = 1.5$ error values worsen as well.

The reconstruction using the thermal pressure profile from $t = 46.0s$ to $t = 52.0s$ with a time step of $0.1s$ was repeated with the addition of the Faraday rotation angle and integrated density with a 0.1 weight for the 3,5, and 7 channels.

It's hard to see any significant differences when looking at the time dependence of the profiles over $\rho_{pol,norm}$. Since the main differences found for the $48.0s$ time slice were observed in the core region, in Figures 4.44, 4.45, 4.46 and 4.47 the values at $\rho_{pol,norm} = 0$ are plotted in time along with some global variables. As can be seen, the biggest differences are seen in the flux surface averaged toroidal current density and safety factor values at the core, as expected, which decrease and increase respectively. The core pressure values do not change much and the stored energy increases slightly when these diagnostics are added to the magnetic reconstruction but not when added to the kinetic reconstruction.

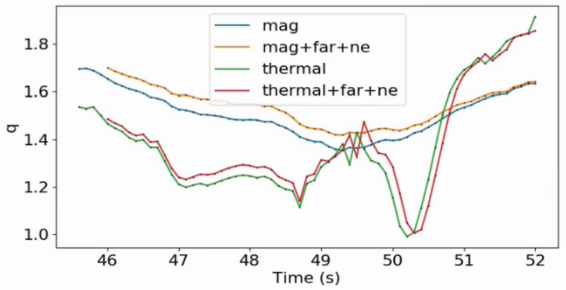

Figure 4.44: Safety factor at $\rho_{pol,norm} = 0$ in function of time. Shot = 90198, Run_eq = 2001, 2675, 2003, 2670.

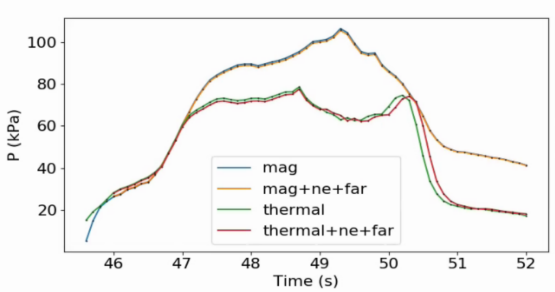

Figure 4.45: Pressure at $\rho_{pol,norm} = 0$ in function of time. Shot = 90198, Run_eq = 2001, 2675, 2003, 2670.

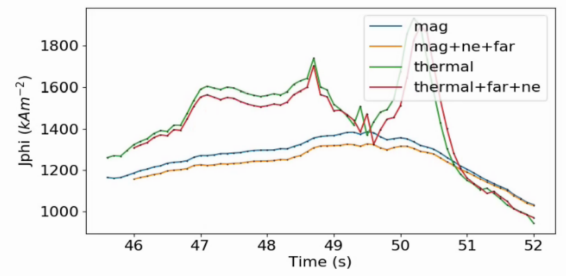

Figure 4.46: Flux surface averaged toroidal current density at $\rho_{pol,norm} = 0$ in function of time. Shot = 90198, Run_eq = 2001, 2675, 2003, 2670.

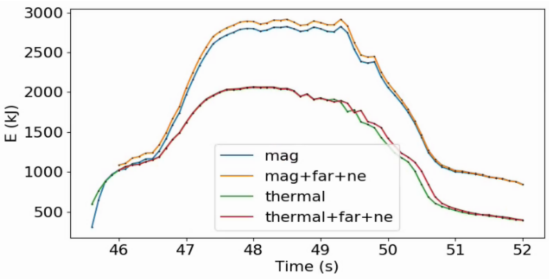

Figure 4.47: Stored energy ($w_{mhd} = \frac{3}{2}\int pdV$) in function of time. Shot = 90198, Run_eq = 2001, 2675, 2003, 2670

The last test was to add the diagnostics to the reconstruction that uses the total pressure profile.

The weights tested were 0.1 and 0.2. It was found that for the 0.1 weight the pressure profile remains the same, the safety factor profile still does not cross the $q = 1$ line and that in spite of still having the minimum off the axis, the shape is closer to the expected than when not using these diagnostics, and so is the shape of the flux surface averaged toroidal current density (as can be seen in Figures 4.43). The safety factor error values in the $m = 3$ and $n = 2$ mode position become better when these diagnostics are added, as can be seen in Table 4.10 but are still worse than for the reconstruction using only the thermal reconstruction. Some of the magnetic errors improve while others worsen.

B_ϕ	mag	mag+ne+far	thermal	thermal+far+ne	total	total+far+ne
3.0436	12.3	16.8	0.4	2.2	24.7	16.8
3.0794	9.4	13.8	4.0	2.1	30.8	24.1
3.9189	12.7	17.3	5.8	3.8	18.0	12.5
3.9367	13.7	18.2	4.6	2.7	15.9	10.4

Table 4.10: EQUAL safety factor error value that corresponds to the $n = 2$ and $m = 3$ mode when compared to $q = 1.5$. Obtained according to section 3.10. Shot = 90198. Runs_eq = 2660, 2661, 2011, 2672. Time = 48.0s.

Chapter 5

Discussion and concluding remarks

This work's main objective was to model the plasma equilibrium of an NBI ($9MW$) + ICRH ($6MW$) heated discharge on JET with increasing levels of information both from diagnostics and numerical codes within the WPCD framework, with the hope of improving the equilibrium reconstruction.

In order to attempt it, the EQUAL equilibrium reconstruction code along with the EQSTABIL RECONSTRUCT AND REFINE workflows were used to make equilibrium reconstructions. First, using only magnetic diagnostics, then adding the thermal pressure, then adding the pressure due to the energetic particles (caused by the ICRH) and then the polarimetry and interferometry diagnostics. This was done for several time slices within the time interval where the ICRH is being used. The thermal pressure was determined using the Thomson scattering diagnostics (HRTS), which gives the electron temperature and density (n_e and T_e), the ion and electron thermal temperatures were assumed to be equal ($T_i = T_e$). The energetic particle components of the pressure were calculated using the CYRANO and StixReDist codes within the Heating and current drive workflow. Only the ICRH's components were considered, since they were found to be much larger than the NBI's. The $(3, 2)$ MHD mode position was used as a way of validating the reconstruction. The energetic ions driven by the ICRH proved to be a major challenge in this thesis, considering the very significant surplus of pressure/energy involved.

The following paragraphs highlight the most significant observations.

The addition of the thermal pressure as a constraint in the equilibrium reconstruction leads to the appearance of a pedestal at $\rho_{pol,norm} = 0.97$ in both the flux surface averaged toroidal current density and pressure reconstructed profiles, which is a characteristic of H-mode. It also leads to better values for the MHD markers but to worse values for the error between the magnetic measurements and their equivalent reconstructed values.

When looking at the time evolution of the equilibrium reconstruction, it can be seen that the reconstruction has a better agreement with the raw data obtained by the HRTS and ECE diagnostics and that the evolution of core pressure matches the evolution of the NBI and ICRH power, when adding the thermal profile as a constraint.

For the time slice $48.0s$, the calculated energetic particle components of the pressure due to the ICRH is concentrated at the core of the plasma for $\rho_{pol,norm} < 0.4$, the energetic deuterium component of the

pressure is concentrated closer to the magnetic axis ($\rho_{pol,norm} < 0.2$) and has a maximum ($110kPa$) higher than for the hydrogen component ($70kPa$). When adding the energetic particle pressures to the thermal pressure (which has a maximum of $70kPa$), the pressure maximum triples (becoming $220kPa$). This maximum is not located at the axis but at $\rho_{pol,norm} = 0.12$.

When looking at the time evolution of the total pressure, we can see that the observations can be generalized. The energetic particle pressures are in the core, and their maximums correspond to the maximum position of the deuterium pressure component and are at $\rho_{pol,norm} = 0.12$, off-axis. When the ICRH power is at a maximum, the pressure triples, but at $46.7s$ time slice (when the pedestal is formed and the ICRH power is at $\sim 2MW$ so at 33% of the maximum power), the addition of the energetic particle pressures still doubles the maximum value.

For the $48.0s$ time slice, using the total pressure profile as a constraint in an equilibrium reconstruction and getting a pressure profile that matches it, proved to be complicated. The addition of the total pressure profile to the reconstruction leads to an increase of the maximum of the reconstructed pressure profile by a factor of 2 when compared to the reconstruction that uses the thermal pressure. It also leads to safety factor and flux surface averaged toroidal current density profiles that have their minimum and maximum respectively off the axis along with a decrease and increase of their values. It is also found that, in general, the magnetic errors get better. The MHD marker error becomes worse. For the other time slices, when the total pressure is smaller, the safety factor is a monotonic function, all other observations are still valid.

It was also found that, using different kinetic reconstructions as the input of the heating and current drive workflow, results in different total pressure profiles.

Using the heating and current drive workflow with the equilibrium that uses the total (thermal and energetic particle components) pressure profile as a constraint, generally leads to pressure profiles with the maximums at the axis with values around $300kPa$, four times larger than the thermal pressure, mostly due to the changes of the pressure component of the energetic deuterium ions. The pressure component of the energetic hydrogen ions and the thermal pressure are similar in both iterations.

When using these total pressure profiles in an equilibrium reconstruction, it is far easier to get a reconstructed pressure profile with the same shape as the total profile, however, it leads to flux surface averaged current density and safety factor core values much higher/lower than expected. The MHD marker errors worsen and so do the magnetic diagnostic errors.

The addition of the Faraday rotation angle and integrated density into the magnetic reconstruction leads to small changes in the core of the profiles and worsens both the (3,2) MHD mode and magnetic errors. Their addition to the kinetic reconstruction that uses the thermal pressure profile, again, leads to small changes in the core of the profiles, but it improves the (3,2) mode errors.

When added to the reconstruction using the total pressure profile, they do not improve the fit of the reconstructed pressure profile to the total pressure, but they soften the curvature of the safety factor and flux surface averaged toroidal current density profiles, improve the MHD marker errors and worsen the magnetic errors.

Zhen Zheng et al. [63] show reconstructions made for a discharge using $3.2MW$ of NBI and $1.8MW$ of

LH wave power injection, $0.4MW$ of ICRH wave power injection and $0.4MW$ of ECRH power injection. Their total pressure was calculated using $P(x) = n_e T_e + (n_i + n_Z)T_i + P_{fast}$, where the electron density and temperature are measured using the TS diagnostic, the ion temperature is obtained using charge exchange recombination spectroscopy and x-ray imaging crystal spectrometer, the ion and impurity densities are determined using the effective charge from bremsstrahlung and quasi-neutrality condition, and the energetic particle pressure is "measured" using the NUBEAM, TORIC and TRANSP codes (only the NBI and ICRH were simulated using the codes). The reconstruction itself was made using the EFIT code.

They seem to use only two iterations of the equilibrium reconstruction, instead of the three used in this work. One magnetic reconstruction, and another with the total pressure, the magnetic equilibrium is the one used in the heating and current drive simulation codes.

Their total pressure profiles don't have off-axis maximums, and their energetic ion pressure is around $\sim 30\%$ of the total pressure at the core (for the time slice that uses the ICRH) instead of the $\sim 53 - 68\%$ of the tests made here, for the $48.0s$ time slice. Since the shape of the total pressure is so different from the thermal pressure, to get the percentage interval, the shapes were assumed to be similar with the maximum value equal to the axis value, for the lower end ($150kPa$ and so 52%) or equal to the maximum value, for the upper end ($220kPa$ and so 68%).

Their kinetic reconstructions result in pressure profiles much closer to the total pressure profiles obtained using numerical codes and diagnostics. They have the pedestal as expected for an H-mode plasma and the maximum pressure (at the axis) is smaller than the "measured" total pressure (by about 10%, $45kPa$ instead of $50Pa$) and the safety factor and current density profiles have the expected shapes (no off-axis maximums and minimums). They also found that the error of the reconstruction increases when the pressure profiles are added.

These differences can be explained by the vast differences in heating power and so the different total pressure profiles.

In order to improve the results, some things might be tried, such as:

Increasing the number of magnetic sensors (~ 250 [1]) would allow a better fit to the sensor data and more accurate magnetic flux surfaces into which to map the HRTS data (the shifts of the mapped profiles would not be necessary).

Still, about the calculation of the thermal pressure, in this work, the ion and electron temperatures were considered to be the same. This is an approximation, which could not be true for several reasons. The external heating methods, NBI and ICRH, heat preferentially the thermal ions and the thermal electrons respectively due to the differences in the energy of the energetic ions created (above a certain critical energy the energetic ion energy is transferred to the electrons by collisions and bellow to the ions), which leads to different temperatures between the thermal electrons and ions. Another reason is the existence of impurities in the plasma (hydrogen ions being one of them, as mentioned in this work), which leads to differences between the deuterium density and the electron density. So other diagnostics could be used to measure the ion temperatures, densities and impurities present in the plasma (as mentioned in Section

[1] From recent information from the magnetics and EFIT++ RO at JET, there is now the possibility to use ~ 250 magnetic sensors instead of the legacy ~ 100 that were routinely used and made available for EFIT and other reconstruction codes.

1.3.8), to get a more accurate thermal pressure profile.

When using the Faraday rotation in the reconstruction, the density profile is needed. In the EQUAL code, this profile is inferred assuming that the basis functions are polynomials and by fitting it to the interferometry measurements (with are the integrated density along lines of sight, not the density in function of the position), with a cost function. Therefore this density profile wouldn't generally match the density profile from HRTS, if it did it might help the results of the reconstruction using the Faraday rotation angle. In the EFIT++ code, the HRTS profile is used for the fit of the density profile.

That being said, the majority of the problems when attempting to make the equilibrium reconstruction with the portion of the pressure due to the energetic particles created by ICRH are present for all the tried total profiles (using different kinetic equilibrium's, time slices, etc) which could be due to the simplifications used that are not appropriate for such high energetic particle pressures. A more accurate analysis of the heating should be made e.g. one that would take into account the time evolution of the density and temperature profiles including not only the heating sources but also the redistribution (diffusion and convection) and energy losses, consistent with various times scales and transport. The workflow used now, the Heating and current drive, only takes into account the sources. The EFIT++ team uses the TRANSP code [64] and adjust the results to experimental measurements such as neutron flux, integrated line densities, fast stored energy,... Within the WPCD framework, a workflow that joined the EQRECONSTRCUT (makes the equilibrium reconstructions) and the ETS (European Transport Simulator) [65] would be a solution.

Another improvement to the work would be adding the TAE (Toroidal Alfvén Eigenmodes) as MHD spectroscopy markers for the validation of the equilibrium reconstruction, along with the NTM (Neoclassical Tearing Modes) and the sawtooth crashes (the inversion radius of the temperature would give the location of the $q = 1$), these were mentioned in Section 1.3.6.

Bibliography

[1] Eia projects nearly 50% increase in world energy usage by 2050, led by growth in asia - today in energy - u.s. energy information administration (eia). `https://www.eia.gov/todayinenergy/detail.php?id=41433`. (Accessed on 07/15/2020).

[2] Hannah Ritchie. Energy. *Our World in Data*, 2014. https://ourworldindata.org/energy.

[3] Shifeng Wang and Sicong Wang. Impacts of wind energy on environment: A review. *Renewable and Sustainable Energy Reviews*, 49:437–443, 2015.

[4] Jeffrey P Freidberg. *Plasma physics and fusion energy*. Cambridge university press, 2008.

[5] G Federici, W Biel, MR Gilbert, R Kemp, N Taylor, and R Wenninger. European demo design strategy and consequences for materials. *Nuclear Fusion*, 57(9):092002, 2017.

[6] Tokamak principle- eurofusion. `https://www.euro-fusion.org/news/detail/detail/News/tokamak-principle/`. (Accessed on 12/24/2019).

[7] Jan Willem Coenen. *The influence of the Dynamic Ergodic Divertor on the radial electric field at the Tokamak TEXTOR*, volume 39. Forschungszentrum Jülich, 2009.

[8] J Havlicek and J Urban. A magnetic equilibrium reconstruction in tokamak. *WDS'07 Proceedings of Contributed Papers Part II—Physics of Plasmas and Ionized Media*, pages 234–239, 2007.

[9] John Wesson and David J Campbell. *Tokamaks*, volume 149. Oxford university press, 2011.

[10] F Porcelli, D Boucher, and MN Rosenbluth. Model for the sawtooth period and amplitude. *Plasma Physics and Controlled Fusion*, 38(12):2163, 1996.

[11] RJ La Haye. Neoclassical tearing modes and their control. *Physics of Plasmas*, 13(5):055501, 2006.

[12] RJ Buttery, TC Hender, DF Howell, RJ La Haye, O Sauter, D Testa, et al. Onset of neoclassical tearing modes on jet. *Nuclear fusion*, 43(2):69, 2003.

[13] WW Heidbrink. Basic physics of alfvén instabilities driven by energetic particles in toroidally confined plasmas. *Physics of Plasmas*, 15(5):055501, 2008.

[14] William P Wehner. *Strategies for Optimal Control of the Current and Rotation Profiles in the DIII-D Tokamak*. PhD thesis, Theses and Dissertations. 2971. https://preserve.lehigh.edu/etd/2971, 2017.

[15] Ian H Hutchinson. Principles of plasma diagnostics. *Plasma Physics and Controlled Fusion*, 44(12):2603, 2002.

[16] GQ Li, QL Ren, JP Qian, LL Lao, SY Ding, YJ Chen, ZX Liu, B Lu, and Q Zang. Kinetic equilibrium reconstruction on east tokamak. *Plasma Physics and Controlled Fusion*, 55(12):125008, 2013.

[17] LL Lao, HE St John, Q Peng, JR Ferron, EJ Strait, TS Taylor, WH Meyer, C Zhang, and KI You. Mhd equilibrium reconstruction in the diii-d tokamak. *Fusion science and technology*, 48(2):968–977, 2005.

[18] DM Thomas. Poloidal magnetic field measurements and analysis with the diii-d libeam system. *Review of scientific instruments*, 74(3):1541–1546, 2003.

[19] Robert C Wolf, A Bock, OP Ford, R Reimer, A Burckhart, A Dinklage, J Hobirk, J Howard, M Reich, and J Stober. Motional stark effect measurements of the local magnetic field in high temperature fusion plasmas. *Journal of Instrumentation*, 10(10):P10008, 2015.

[20] R Boivin. Diagnostics for magnetic fusion power plants. In *Magnetic Fusion Energy*, pages 549–575. Elsevier, 2016.

[21] SL Prunty. A primer on the theory of thomson scattering for high-temperature fusion plasmas. *Physica Scripta*, 89(12):128001, 2014.

[22] RC Isler. A review of charge-exchange spectroscopy and applications to fusion plasmas. *Physica Scripta*, 35(5):650, 1987.

[23] M Bornatici, R Cano, O De Barbieri, and F Engelmann. Electron cyclotron emission and absorption in fusion plasmas. *Nuclear Fusion*, 23(9):1153, 1983.

[24] Wolfgang Zwingmann. Equilibrium analysis of steady state tokamak discharges. *Nuclear fusion*, 43(9):842, 2003.

[25] PJ Mc Carthy, CB Forest, M Foley, L Giannone, O Gruber, J Hobirk, LD Horton, K Lackner, P Martin, M Reich, et al. Plasma geometry and current profile identification on asdex upgrade using an integrated equilibrium generation and interpretation system. In *The 21st IAEA Fusion Energy Conference*, 2006.

[26] Didier Mazon, Jacques Blum, Cedric Boulbe, Blaise Faugeras, M Baruzzo, A Boboc, S Bremond, M Brix, P De Vries, S Sharapov, et al. Equinox: A real-time equilibrium code and its validation at jet. In *From physics to control through an emergent view*, pages 327–332. World Scientific, 2010.

[27] P Hertout, Cédric Boulbe, Eric Nardon, J Blum, Sylvain Brémond, Jérome Bucalossi, Blaise Faugeras, Virginie Grandgirard, and P Moreau. The cedres++ equilibrium code and its application to iter, jt-60sa and tore supra. *Fusion Engineering and Design*, 86(6-8):1045–1048, 2011.

[28] Blaise Faugeras, Francesco Orsitto, and JET Contributors. Equilibrium reconstruction at jet using stokes model for polarimetry. *Nuclear Fusion*, 58(10):106032, 2018.

[29] Filippo Sartori, A Cenedese, and F Milani. Jet real-time object-oriented code for plasma boundary reconstruction. *Fusion Engineering and Design*, 66:735–739, 2003.

[30] W Zwingmann, R Coelho, V Drozdov, LG Eriksson, B Guillerminet, P Huynh, GTA Huysmans, C Konz, F Imbeaux, DC McDonald, et al. Validation procedure of the tokamak equilibrium reconstruction code equal with a scientific workflow system. In *P4-180, 37th EPS Conference on Plasma Physics, Dublin*, 2010.

[31] Hinrich Lütjens, A Bondeson, and A Roy. Axisymmetric mhd equilibrium solver with bicubic hermite elements. *Computer physics communications*, 69(2-3):287–298, 1992.

[32] G Poulipoulis, GN Throumoulopoulos, C Konz, and EFDA ITM-TF Contributors. Extending helena to equilibria with incompressible parallel plasma rotation. In *39th EPS Conference on Plasma Physics and 16th International Congress on Plasma Physics*. European Physical Society, 2012.

[33] R Fischer, A Bock, M Dunne, JC Fuchs, L Giannone, K Lackner, PJ McCarthy, E Poli, R Preuss, M Rampp, et al. Coupling of the flux diffusion equation with the equilibrium reconstruction at asdex upgrade. *Fusion Science and Technology*, 69(2):526–536, 2016.

[34] Jakob Svensson, O Ford, A Werner, Gregory Von Nessi, Matthew Hole, DC McDonald, L Appel, M Beurskens, A Boboc, M Brix, et al. Connecting physics models and diagnostic data using bayesian graphical models. In *37th EPS Conference on Plasma Physics*, volume 4, page 117. European Physical Society, 2010.

[35] Luo Jia-rong. Review of the equilibrium fitting for non-circular tokamak. *Plasma Science and Technology*, 4(2):1183, 2002.

[36] L.L. Lao. Tokamak and iter equilibrium reconstruction. Present at Workshop on ITER Simulation, Beijing, China, 2006.

[37] DW Swain and GH Neilson. An efficient technique for magnetic analysis of non-circular, high-beta tokamak equilibria. *Nuclear Fusion*, 22(8):1015, 1982.

[38] JL Luxon and BB Brown. Magnetic analysis of non-circular cross-section tokamaks. *Nuclear Fusion*, 22(6):813, 1982.

[39] LL Lao, H St John, RD Stambaugh, AG Kellman, and W Pfeiffer. Reconstruction of current profile parameters and plasma shapes in tokamaks. *Nuclear fusion*, 25(11):1611, 1985.

[40] D Wroblewski and LL Lao. Polarimetry of motional stark effect and determination of current profiles in diii-d. *Review of scientific instruments*, 63(10):5140–5147, 1992.

[41] DP O'Brien, LL Lao, ER Solano, M Garribba, TS Taylor, JG Cordey, and JJ Ellis. Equilibrium analysis of iron core tokamaks using a full domain method. *Nuclear fusion*, 32(8):1351, 1992.

[42] JR Ferron, ML Walker, LL Lao, HE St John, DA Humphreys, and JA Leuer. Real time equilibrium reconstruction for tokamak discharge control. *Nuclear Fusion*, 38(7):1055, 1998.

[43] K Tritz, D Stutman, LF Delgado-Aparicio, M Finkenthal, D Pacella, R Kaita, B Stratton, and S Sabbagh. Current profile reconstruction using electron temperature imaging diagnostics. *Review of scientific instruments*, 75(10):4033–4036, 2004.

[44] DM Thomas, AW Leonard, and HW Mueller. Calculation of edge toroidal current density distributions from diii-d lithium beam measurements using ampere's law. *Review of scientific instruments*, 75(10):4109–4111, 2004.

[45] LC Appel, MJ Hole, Jakob Svensson, Gregory Von Nessi, et al. Bayesian inference applied to magnetic equilibrium on mast. In *Europhysics Conference Abstracts (Dublin, Ireland, 2010)*, 2010.

[46] P.U. Lamalle. *Nonlocal theoretical generalisation and tridimensional numerical study of the coupling of an ICRH antenna to a tokamak plasma.* PhD thesis, Université de Mons, LPP-ERM/KMS Report nr. 101., 1994.

[47] Marco Brambilla. Numerical simulation of ion cyclotron waves in tokamak plasmas. *Plasma Physics and Controlled Fusion*, 41(1):1, 1999.

[48] RJ Dumont. Variational approach to radiofrequency waves in magnetic fusion devices. *Nuclear Fusion*, 49(7):075033, 2009.

[49] Laurent Villard, Stephan Brunner, and Jan Vaclavik. Global marginal stability of taes in the presence of fast ions. *Nuclear Fusion*, 35(10):1173, 1995.

[50] E Poli, AG Peeters, and GV Pereverzev. Torbeam, a beam tracing code for electron-cyclotron waves in tokamak plasmas. *Computer Physics Communications*, 136(1-2):90–104, 2001.

[51] Thomas Johnson, Antti Salmi, G Steinbrecher, L-G Eriksson, T Hellsten, LJ Höök, M Schneider, and ITM-TF Contributors. Library for rf interactions in orbit following codes. In *AIP Conference Proceedings*, volume 1406, pages 373–376. American Institute of Physics, 2011.

[52] Dirk Van Eester and Ernesto Lerche. Simple 1d fokker–planck modelling of ion cyclotron resonance frequency heating at arbitrary cyclotron harmonics accounting for coulomb relaxation on non-maxwellian populations. *Plasma Physics and Controlled Fusion*, 53(9):092001, 2011.

[53] Otto Asunta, J Govenius, Robert Budny, M Gorelenkova, Giovanni Tardini, Taina Kurki-Suonio, Antti Salmi, Seppo Sipilä, et al. Modelling neutral beams in fusion devices: Beamlet-based model for fast particle simulations. *Computer Physics Communications*, 188:33–46, 2015.

[54] M Schneider, L-G Eriksson, I Jenkins, JF Artaud, V Basiuk, F Imbeaux, T Oikawa, JET-EFDA contributors, et al. Simulation of the neutral beam deposition within integrated tokamak modelling frameworks. *Nuclear Fusion*, 51(6):063019, 2011.

[55] M Schneider, L-G Eriksson, Tomas Johnson, R Futtersack, JF Artaud, R Dumont, B Wolle, and ITM-TF Contributors. A rapid fast ion fokker–planck solver for integrated modelling of tokamaks. *Nuclear Fusion*, 55(1):013003, 2014.

[56] Introduction to the eurofusion project code development for integrated modelling — eurofusion integrated modelling workflows 3.0 documentation. `https://wpcd-workflows.github.io/introduction.html`. (Accessed on 01/02/2020).

[57] JF Artaud, V Basiuk, F Imbeaux, Martin Schneider, J Garcia, G Giruzzi, P Huynh, T Aniel, F Albajar, JM Ané, et al. The cronos suite of codes for integrated tokamak modelling. *Nuclear Fusion*, 50(4):043001, 2010.

[58] O Meneghini, SP Smith, LL Lao, O Izacard, Q Ren, JM Park, J Candy, Z Wang, CJ Luna, VA Izzo, et al. Integrated modeling applications for tokamak experiments with omfit. *Nuclear Fusion*, 55(8):083008, 2015.

[59] Schema documentation for phase4top.xsd. `https://wpcd-workflows.github.io/_static/Phase4.10b.10_HTML/Phase4TOP.html`. (Accessed on 10/15/2020).

[60] The kepler project — kepler. `https://kepler-project.org/`. (Accessed on 11/04/2020).

[61] Jet- eurofusion. `https://www.euro-fusion.org/devices/jet/`. (Accessed on 10/15/2020).

[62] Paulo Rodrigues and Francesca Cella. High-order geodesic coupling of shear-alfv\'{e} n and acoustic continua in tokamaks. *arXiv preprint arXiv:2008.12753*, 2020.

[63] Zhen Zheng, Nong Xiang, CHEN Jiale, DING Siye, DU Hongfei, LI Guoqiang, WANG Yifeng, LIU Haiqing, LI Yingying, LYU Bo, et al. Kinetic equilibrium reconstruction for the nbi-and icrh-heated h-mode plasma on east tokamak. *Plasma Science and Technology*, 20(6):065103, 2018.

[64] Transp. `https://transp.pppl.gov/`. (Accessed on 06/07/2021).

[65] European transport simulator (ets) — eurofusion integrated modelling workflows 3.0 documentation. `https://wpcd-workflows.github.io/ets.html`. (Accessed on 06/07/2021).

Appendix A

EQUAL parameters

A.1 EQUAL Parameters using only the magnetic diagnostics

grid	
nz	97
nr	97

fitting	
verbose	0
error_it	1.0e-5
maxit	80
min_plasma_current	100000.0
show_signal	2

weight	
ip	0.1
diamag	1.0e-8
flux	1.0e-0 0.0 1.0e-0 0.0 1.0e-0 1.0e-0 1.0e-0 1.0e-0 1.0e-0 1.0e-0 1.0e-0 1.0e-0 1.0e-0 1.0e-0 1.0e-0 1.0e-0 1.0e-0 1.0e-0 1.0e-0 1.0e-0 1.0e-0 0.0 1.0e-0 1.0e-0 1.0e-0 1.0e-0 1.0e-0 1.0e-0 0.0 0.0 1.0e-0 1.0e-0 1.0e-0 1.0e-0 0.0e-0 0.0
bpol	1.0 1.0 1.0 1.0 1.0 1.0 1.0 1.0 1.0 1.0 1.0 1.0 1.0 1.0 1.0 1.0 1.0 1.0 1.0 1.0 1.0 1.0 0.0 1.0 0.0 1.0 0.0 0.0 1.0 1.0 1.0 1.0 1.0 0.0 0.0 0.0 0.0 0.0 1.0 1.0 0.0 1.0 1.0 0.0 1.0 0.0 0.0 0.0 0.0 0.0 0.0 0.0 0.0 0.0 0.0 1.0 1.0 0.0 0.0 0.0 0.0 0.0 0.0 0.0 0.0 0.0 0.0 0.0 0.0 0.0 0.0
pfcoil	1.0e-0 1.0e-0 1.0e-0 1.0e-0 1.0e-0 1.0e-0 1.0e-0 1.0e-0 1.0e-0 1.0e-0 1.0e-0 1.0e-0 1.0e-0 1.0e-0 1.0e-0 1.0e-0
iron	0.5 0.5 0.5 0.5 0.5 0.5 0.5 0.5 0.5 0.50.5 0.5 0.5 0.5 0.5 0.5 0.5 0.5 0.5 0.5 0.5 0.5 0.5 0.5 0.5 0.5 0.5 0.5 0.5 0.5 0.5 0.5 0.5 0.5 0.5 0.5 0.5 0.5 0.5 0.5 0.5 0.5 0.5 0.5 0.5 0.5 0.5 0.5 0.5 0.5 0.5 0.50.5 0.5 0.5 0.5 0.5 0.5 0.5 0.5 0.5 0.5 0.5 0.5
mse	1.0e-8 1.0e-8 1.0e-8 1.0e-8 1.0e-81.0e-8 1.0e-8 1.0e-8 1.0e-8 1.0e-8 1.0e-8 1.0e-8 1.0e-8 1.0e-8 1.0e-8 1.0e-8 1.0e-8 1.0e-8 1.0e-8 1.0e-8 1.0e-8 1.0e-8 1.0e-8 1.0e-8 1.0e-8
faraday	
ne	
pressure	
flux_in_weber	.true.

profile	
npprime	5
pprime_type	B
pprime_zerobound	.false.
pprime_wbound	0.5
pp_knot	0.2 0.6 0.8 0.9 0.95
pp_knot_tune_reg	0.050 0.050 0.020 0.010 0.050 0.050 0.050
nffprime	5
ffprime_\type	B
ffprime_zerobound	.false.
ffprime_wbound	0.5
ff_knot	0.2 0.6 0.8 0.9 0.95
ff_knot_tune_reg	0.010 0.010 0.010 0.002 0.001 0.001 0.001
nstab	1
constraint_type	lang_lao
constraint_weight	0.005
constraint_tuneff	1.0

A.2 EQUAL Parameters using magnetic diagnostics and thermal pressure

grid	
nz	97
nr	97

fitting	
verbose	0
error_it	1.0e-3
maxit	80
min_plasma_current	100000.0
show_signal	2

weight	
ip	0.1
diamag	1.0e-8
flux	1.0e-0 0.0 1.0e-0 0.0 1.0e-0 1.0e-01.0e-0 1.0e-0 1.0e-0 1.0e-0 1.0e-0 1.0e-0 1.0e-0 1.0e-0 1.0e-0 1.0e-0 1.0e-0 1.0e-0 1.0e-0 1.0e-0 1.0e-0 0.0 1.0e-0 1.0e-0 1.0e-0 1.0e-0 1.0e-0 1.0e-0 0.0 0.0 1.0e-0 1.0e-0 1.0e-0 1.0e-0 0.0e-0 0.0
bpol	1.0 1.0 1.0 1.0 1.0 1.0 1.0 1.0 1.0 1.01.0 1.0 1.0 1.0 1.0 1.0 1.0 1.0 1.0 1.0 1.0 1.0 0.0 1.0 0.0 1.0 0.0 0.0 1.0 1.01.0 1.0 1.0 0.0 0.0 0.0 0.0 0.0 1.0 1.0 0.0 1.0 1.0 0.0 1.0 0.0 0.0 0.0 0.0 0.00.0 0.0 0.0 0.0 0.0 1.0 1.0 0.0 0.0 0.0 0.0 0.0 0.0 0.0 0.0 0.0 0.0 0.0 0.0 0.00.0
pfcoil	1.0e-0 1.0e-0 1.0e-0 1.0e-0 1.0e-01.0e-0 1.0e-0 1.0e-0 1.0e-0 1.0e-01.0e-0 1.0e-0 1.0e-0 1.0e-0 1.0e-0 1.0e-0
iron	0.5 0.5 0.5 0.5 0.5 0.5 0.5 0.5 0.5 0.50.5 0.5 0.5 0.5 0.5 0.5 0.5 0.5 0.5 0.5 0.5 0.5 0.5 0.5 0.5 0.5 0.5 0.5 0.5 0.5 0.5 0.5 0.5 0.5 0.5 0.5 0.5 0.5 0.5 0.5 0.5 0.5 0.5 0.5 0.5 0.5 0.5 0.5 0.5 0.5 0.5 0.5 0.5 0.5 0.5 0.5 0.5 0.5 0.5 0.5 0.5 0.5 0.5 0.5 0.5 0.5 0.5
mse	1.0e-8 1.0e-8
faraday	
ne	
pressure	0.95 0.95 0.95 0.95 0.95 0.95 0.95 0.95 0.95 0.95 0.95 0.95 0.95 0.95 0.95 0.95 0.95 0.95 0.95 0.95 0.95 0.95 0.95 0.95 0.95 0.95 0.95 0.95 0.95 0.95 0.95 0.95 0.95 0.95 0.95 0.95 0.95 0.95 0.95 0.95 0.95 0.95 0.95 0.95 0.95 0.95 0.95 0.95 0.95 0.95 0.95 0.95 0.95 0.95 0.95 0.95 0.95 0.95 0.95 0.95 0.95 0.95 0.95 0.95 0.95 0.95 0.95 0.95 0.95 0.95 0.95 0.95 0.95 0.95 0.95 0.95 0.95 0.95 0.95 0.95 0.95 0.95 0.95 0.95 0.95 0.95 0.95 0.95 0.95 0.95 0.95 0.95 0.95 0.95 0.95 0.95 0.95 0.95 0.95 0.95
flux_in_weber	.true.

profile	
npprime	6
pprime_type	B
pprime_zerobound	.false.
pprime_wbound	0.1
pp_knot	0.022 0.2 0.64 0.90 0.95 0.98
pp_knot_tune_reg	0.0090 0.0050 0.0035 0.0025 0.0015 0.0009 0.0005 0.0001
nffprime	6
ffprime_\type	B
ffprime_zerobound	.false.
ffprime_wbound	0.1
ff_knot	0.022 0.2 0.64 0.90 0.95 0.98
ff_knot_tune_reg	0.010 0.010 0.010 0.009 0.008 0.006 0.005 0.005
nstab	1
constraint_type	lang_lao
constraint_weight	0.002
constraint_tuneff	1.0

A.3 EQUAL Parameters using magnetic diagnostics and total pressure

grid	
nz	129
nr	129

farad	
verbose	0

fitting	
cocos$_i n$	13
verbose	1
error_it	1.0e-5
maxit	80
min_plasma_current	100000.0
show_signal	2

weight	
ip	0.1
diamag	1.0e-8
flux	1.0 0.0 1.0 0.0 1.0 1.0 1.0 1.0 1.0 1.0 1.0 1.0 1.0 1.0 1.0 1.0 1.0 1.0 1.0 1.0 1.0 0.0 1.0 1.0 1.0 1.0 1.0 1.0 0.0 0.0 1.0 1.0 1.0 1.0 0.0 0.0
bpol	1.0 1.0 1.0 1.0 1.0 1.0 1.0 1.0 1.0 1.0 1.0 1.0 1.0 1.0 1.0 1.0 1.0 1.0 1.0 1.0 1.0 1.0 0.0 1.0 0.0 1.0 0.0 0.0 1.0 1.0 1.0 1.0 1.0 0.0 0.0 0.0 0.0 0.0 1.0 1.0 0.0 1.0 1.0 0.0 1.0 0.0 0.0 0.0 0.0 0.0 0.0 0.0 0.0 0.0 0.0 1.0 1.0 0.0 0.0 0.0 0.0 0.0 0.0 0.0 0.0 0.0 0.0 0.0 0.0 0.0 0.0
pfcoil	1.0 1.0 1.0 1.0 1.0 1.0 1.0 1.0 1.0 1.0 1.0 1.0 1.0 1.0 1.0 1.0
iron	0.5 0.5 0.5 0.5 0.5 0.5 0.5 0.5 0.5 0.50.5 0.5 0.5 0.5 0.5 0.5 0.5 0.5 0.5 0.5 0.5 0.5 0.5 0.5 0.5 0.5 0.5 0.5 0.5 0.5 0.5 0.5 0.5 0.5 0.5 0.5 0.5 0.5 0.5 0.5 0.5 0.5 0.5 0.5 0.5 0.5 0.5 0.5 0.5 0.5 0.5 0.5 0.5 0.5 0.5 0.5 0.5 0.5 0.5 0.5 0.5 0.5
mse	1.0e-8 1.0e-8
faraday	
ne	
pressure	1.00 1.00 1.00 1.00 1.00 1.00 1.00 1.00 1.00 1.00 1.00 1.00 1.00 1.00 1.00 1.00 1.00 1.00 0.30 1.00 1.00 1.00 1.00 1.00 1.00 1.00 1.00 1.00 1.00 1.00 1.00 1.00 1.00 1.00 1.00 1.00 1.00 1.00 1.00 1.00 1.00 1.00 1.00 1.00 1.00 1.00 1.00 1.00 1.00 1.00 1.00 1.00 1.00 1.00 1.00 1.00 1.00 1.00
pressure_abserr	1000.0
pressure_relerr	0.1
pressure_data_format	1
pressure_data_type	total
flux_in_weber	.true.

profile	
npprime	11
pprime_type	B
pprime_zerobound	.false.
pprime_wbound	0.2
pp_knot	0.0101 0.0188 0.0288 0.0475 0.0885 0.1263 0.1523 0.1794 0.90 0.9581 0.9816
pp_knot_tune_reg	0.0007 0.0018 0.0008 0.0008 0.0013 0.0008 0.0008 0.0007 0.0008 0.0007 0.0008 0.0008 0.0008
nffprime	11
ffprime_\type	B
ffprime_zerobound	.false.
ffprime_wbound	0.2
ff_knot	0.0101 0.0188 0.0288 0.0475 0.0885 0.1263 0.1523 0.1794 0.90 0.9581 0.9816
ff_knot_tune_reg	0.009 0.009 0.009 0.009 0.009 0.009 0.009 0.002 0.002 0.002 0.002 0.009 0.009 0.009
nstab	1
constraint_type	lang_lao
constraint_weight	0.00086
constraint_tuneff	0.5

output	
nprof	201
$\text{cocos}_o ut$	13

least_squares	
verbose	0

plasma_boundary	
verbose	0

A.4 EQUAL Parameters using magnetic diagnostics and different thermal profiles

Only the pressure weights, other are similar to appendix A.2.

pressure	a	all are 1.00
pressure	b	0.00 0.00 0.00 0.00 0.00 0.00 0.00 0.00 0.00 0.00 0.00 0.00 0.00 0.00 0.00 0.00 0.00 0.00 0.00 0.00 0.00 0.00 0.00 0.00 0.00 0.00 0.00 0.00 0.00 0.00 0.00 0.00 0.00 0.00 0.00 0.00 0.00 0.00 0.00 0.00 0.00 0.00 0.00 0.00 0.00 0.00 0.00 0.00 0.00 0.00 0.00 0.00 0.00 0.00 0.00 0.00 0.00 0.00 0.00 1.00 1.00 1.00 1.00 1.00 1.00 1.00 1.00 1.00 1.00 1.00 1.00 1.00 1.00 1.00 1.00 1.00 1.00 1.00 1.00 1.00 1.00 1.00 1.00 1.00 1.00 1.00 1.001.00 1.00 1.00 1.00 1.00 1.00 1.00 1.00 1.00
pressure	c	0.00 0.00 0.00 0.00 0.00 0.00 0.00 0.00 0.00 0.00 0.00 0.00 0.00 0.00 0.00 0.00 0.00 0.00 0.00 0.00 0.00 0.00 0.00 0.00 0.00 0.00 0.00 0.00 0.00 0.00 0.00 0.00 0.00 0.00 0.00 0.00 0.00 0.00 0.00 0.00 0.00 0.00 0.00 0.00 0.00 0.00 0.00 0.00 0.00 0.00 0.00 0.00 0.00 0.00 0.00 0.00 0.00 0.00 0.00 0.00 0.00 0.00 0.00 0.00 1.00 1.00 1.00 1.00 1.00 1.00 1.00 1.00 1.00 1.00 1.00 1.00 1.00 1.00 1.00 1.00 1.00 1.00 1.00 1.00 1.00 1.00 1.00 1.00 1.00 1.00 1.00 1.00 1.00 1.00 1.00 1.00
pressure	d	0.00 0.00 0.00 0.00 0.00 0.00 0.00 0.00 0.00 0.00 0.00 0.00 0.00 0.00 0.00 0.00 0.00 0.00 0.00 0.00 0.00 0.00 0.00 0.00 0.00 0.00 0.00 0.00 0.00 0.00 0.00 0.00 0.00 0.00 0.00 0.00 0.00 0.00 0.00 0.00 0.00 0.00 0.00 0.00 0.00 0.00 0.00 0.00 0.00 0.00 0.00 0.00 0.00 0.00 0.00 0.00 0.00 0.00 0.00 0.00 0.00 0.00 0.00 0.00 0.00 0.00 0.00 0.00 0.00 0.00 0.00 0.00 0.00 0.00 0.00 1.00 1.00 1.00 1.00 1.00 1.00 1.00 1.00 1.00 1.00 1.00 1.00 1.00 1.00 1.00 1.00 1.00 1.00 1.00
pressure	e	0.00 0.00 0.00 0.00 0.00 0.00 0.00 0.00 0.00 0.00 0.00 0.00 0.00 0.00 0.00 0.00 0.00 0.00 0.00 0.00 0.00 0.00 0.00 0.00 0.00 0.00 0.00 0.00 0.00 0.00 0.00 0.00 0.00 0.00 0.00 0.00 0.00 0.00 0.00 0.00 0.00 0.00 0.00 0.00 0.00 0.00 0.00 0.00 0.00 0.00 0.00 0.00 0.00 0.00 0.00 0.00 0.000.00 0.00 0.00 0.00 0.00 0.00 0.00 0.00 0.00 0.00 0.00 0.00 0.00 0.00 0.00 0.00 0.00 0.00 0.00 0.00 0.00 0.00 0.00 0.00 0.00 1.00 1.00 1.00 1.001.00 1.00 1.00 1.00 1.00 1.00 1.00 1.00 1.00
pressure	f	0.00 0.00 0.00 0.00 0.00 0.00 0.00 0.00 0.00 0.000.00 0.00 0.00 0.00 0.00 0.00 0.00 0.00 0.00 0.00 0.00 0.00 0.00 0.00 0.00 0.00 0.00 0.00 0.00 0.00 0.00 0.00 0.00 0.00 0.00 0.00 0.00 0.00 0.00 0.00 0.00 0.00 0.00 0.00 0.00 0.00 0.00 0.00 0.00 0.00 0.00 0.00 0.00 0.00 0.00 0.00 0.00 0.00 0.00 0.00 0.00 0.00 0.00 0.00 0.00 0.00 0.00 0.00 0.00 0.00 0.00 0.00 0.00 0.00 0.00 0.00 0.000.00 0.00 0.00 0.00 0.00 0.00 0.00 1.00 1.00 1.00 1.00 1.00 1.00 1.00 1.00 1.00 1.00 1.00 1.00 1.00
pressure	g	all are 0.00

A.5 EQUAL Parameters using magnetic diagnostics and total pressure for different thermal pressure profiles

A.5.1 Parameters for equilibrium reconstruction a (Run=2042)

Only the pressure weights, other are similar to appendix C.

pressure	1.00 1.00 1.00 1.00 1.00 1.00 1.00 1.00 1.00 1.00 1.00 1.00 1.00 1.00 1.00 1.00 1.00 1.00 1.00 1.00 1.00 1.00 1.00 1.00 1.00 1.00 1.00 1.00 1.00 1.00 1.00 1.00 1.00 1.00 1.00 1.00 1.00 1.00 1.00 1.00 1.00 1.00 1.00 1.00 1.00 1.00 1.00 1.00 1.00 1.00 1.00 1.00 1.00 1.00 1.00 1.00 1.00 1.00 1.00 1.00 0.30 1.00 1.00 1.00 1.00 1.00 1.00 1.00 1.00 1.00 1.00 1.00 1.00 1.00 1.00 1.00 1.00 1.00 1.00 1.00 1.00 1.00 1.00 1.00 1.00 1.00 1.00 1.00 1.00 1.00 1.00 1.00 1.00 1.00 1.00

profile	
npprime	11
pprime_type	B
pprime_zerobound	.false.
pprime_wbound	0.2
pp_knot	0.0001 0.002 0.0114 0.0482 0.0900 0.120 0.150 0.180 0.4 0.958 0.983
pp_knot_tune_reg	0.00005 0.0001 0.0001 0.0001 0.0001 0.005 0.005 0.005 0.005 0.005 0.005 0.001 0.001
nffprime	11
ffprime_\type	B
ffprime_zerobound	.false.
ffprime_wbound	0.2
ff_knot	0.001 0.002 0.0114 0.0482 0.0900 0.120 0.150 0.180 0.4 0.958 0.983
ff_knot_tune_reg	0.0001 0.0001 0.0001 0.001 0.0001 0.001 0.001 0.001 0.001 0.001 0.009 0.009 0.009
nstab	1
constraint_type	lang_lao
constraint_weight	0.001
constraint_tuneff	0.5

A.5.2 Parameters for equilibrium reconstruction b (Run=2044)

Only the pressure weights, other are similar to appendix A.3.

pressure	1.00 1.00 1.00 1.00 1.00 1.00 1.00 1.00 1.00 1.00 1.00 1.00 1.00 0.30 1.00 1.00 1.00 1.00 1.00 1.00 1.00 1.00 1.00 1.00 1.00 1.00 1.00 1.00 1.00 1.00 1.00 1.00 1.00 1.00 1.00 1.00 1.00 1.00 1.00 1.00 1.00 1.00 1.00 1.00 1.00 1.00 1.00 1.00 1.00 1.00 1.00 1.00 1.00

profile	
npprime	11
pprime_type	B
pprime_zerobound	.false.
pprime_wbound	0.2
pp_knot	0.0062 0.0184 0.0316 0.0478 0.0807 0.117 0.160 0.190 0.4 0.951 0.980
pp_knot_tune_reg	0.00005 0.00005 0.0001 0.001 0.0005 0.001 0.001 0.001 0.0005 0.005 0.0001 0.0001
nffprime	11
ffprime_\type	B
ffprime_zerobound	.false.
ffprime_wbound	0.2
ff_knot	0.0062 0.0184 0.0316 0.0478 0.0807 0.117 0.160 0.190 0.4 0.951 0.980
ff_knot_tune_reg	0.001 0.001 0.001 0.001 0.001 0.001 0.001 0.001 0.0001 0.001 0.009 0.009 0.009
nstab	1
constraint_type	lang_lao
constraint_weight	0.0096
constraint_tuneff	0.5

A.5.3 Parameters for equilibrium reconstruction d (Run=2043)

Only the pressure weights, other are similar to appendix A.3.

pressure	1.00 1.00 1.00 1.00 1.00 1.00 1.00 1.00 1.00 1.00 1.00 1.00 1.00 1.00 1.00 1.00 1.00 1.00 1.00 1.00 1.00 1.00 1.00 1.00 1.00 1.00 1.00 1.00 1.00 1.00 1.00 1.00 1.00 1.00 0.50 0.50 0.50 0.50 0.50 0.50 0.50 0.50 0.50 0.50 0.50 0.50 0.50 0.50 0.50 0.50 0.30 1.00 1.00 1.00 1.00 1.00 1.00 1.00 1.00 1.00 1.00 1.00 1.00 1.00 1.00 1.00 1.00 1.00 1.00 1.00 1.00 1.00 1.00 1.00 1.00 1.00 1.00 1.00 1.00 1.00 1.00 1.00 1.00 1.00 1.00

profile	
npprime	11
pprime_type	B
pprime_zerobound	.false.
pprime_wbound	0.2
pp_knot	0.0048 0.0178 0.0316 0.0407 0.0651 0.0943 0.128 0.149 0.4 0.949 0.978
pp_knot_tune_reg	0.00001 0.00001 0.00005 0.0005 0.001 0.001 0.001 0.001 0.001 0.0001 0.005 0.0001 0.0001
nffprime	11
ffprime_\type	B
ffprime_zerobound	.false.
ffprime_wbound	0.2
ff_knot	0.0048 0.0178 0.0316 0.0407 0.0651 0.0943 0.128 0.149 0.4 0.949 0.978
ff_knot_tune_reg	0.0001 0.0001 0.0001 0.001 0.001 0.001 0.001 0.001 0.001 0.001 0.009 0.009 0.009
nstab	1
constraint_type	lang_lao
constraint_weight	0.00304
constraint_tuneff	0.5

A.5.4 Parameters for equilibrium reconstruction g (Run=2045)

Only the pressure weights, other are similar to appendix A.3.

pressure	1.00 1.00 1.00 1.00 1.00 1.00 1.00 1.00 0.50 0.50 0.50 0.50 0.50 0.50 0.50 0.50 0.50 0.50 0.30 1.00 1.00 1.00 1.00 1.00 1.00 1.00 1.00 1.00 1.00 1.00 1.00 1.00 1.00 1.00 1.00 1.00 1.00 1.00 1.00 1.00 1.00 1.00 1.00 1.00 1.00 1.00 1.00 1.00 1.00 1.00 1.00 1.00 1.00 1.00 1.00 1.00 1.00 1.00

profile	
npprime	7
pprime_type	B
pprime_zerobound	.false.
pprime_wbound	0.2
pp_knot	0.0105 0.0210 0.0380 0.0575 0.4 0.898 0.960
pp_knot_tune_reg	0.00001 0.00001 0.00001 0.0005 0.0005 0.005 0.005 0.0001 0.0001
nffprime	7
ffprime_\type	B
ffprime_zerobound	.false.
ffprime_wbound	0.2
ff_knot	0.0105 0.0210 0.0380 0.0575 0.4 0.898 0.960
ff_knot_tune_reg	0.001 0.001 0.001 0.001 0.0001 0.001 0.009 0.009 0.009
nstab	1
constraint_type	lang_lao
constraint_weight	0.0065
constraint_tuneff	0.5

A.6 Parameters for fourth equilibrium reconstruction a (Run=2058)

Only the pressure weights, other are similar to appendix A.3.

pressure	2.00 2.00 2.00 2.00 2.00 2.00 2.00 2.00 2.00 2.00 2.00 2.00 2.00 2.00 2.00 2.00 2.00 2.00 2.00 2.00 1.00 1.00 1.00 1.00 1.00 1.00 1.00 1.00 1.00 1.00 1.00 1.00 1.00 1.00 1.00 1.00 1.00 1.00 1.00 1.00 0.50 1.00 1.00 1.00 1.00 1.00 1.00 1.00 1.00 1.00 1.00 1.00 1.00 1.00 1.00 1.00 1.00 1.00 1.00 1.00 1.00 1.00 1.00 1.00 1.00 1.00 1.00 1.00 1.00 1.00 1.00 1.00 1.00

profile	
npprime	10
pprime_type	B
pprime_zerobound	.false.
pprime_wbound	0.2
pp_knot	0.00006 0.0053 0.011 0.023 0.033 0.208 0.4 0.9 0.931 0.973
pp_knot_tune_reg	0.00001 0.00001 0.0001 0.0001 0.0005 0.0005 0.0005 0.0005 0.0005 0.0001 0.0001
nffprime	10
ffprime_\type	B
ffprime_zerobound	.false.
ffprime_wbound	0.2
ff_knot	0.00006 0.0053 0.011 0.023 0.033 0.208 0.4 0.9 0.931 0.973
ff_knot_tune_reg	0.0001 0.0001 0.001 0.001 0.001 0.001 0.001 0.001 0.009 0.009 0.009 0.009
nstab	1
constraint_type	lang_lao
constraint_weight	0.00026
constraint_tuneff	0.5

A.7 Parameters for equilibrium reconstruction b (Run=2060)

Only the pressure weights, other are similar to appendix C.

pressure	1.00 1.00

profile	
npprime	11
pprime_type	B
pprime_zerobound	.false.
pprime_wbound	0.2
pp_knot	0.0008 0.0107 0.0194 0.0636 0.1017 0.1480 0.1871 0.4 0.8 0.927 0.979
pp_knot_tune_reg	0.00008 0.0001 0.0001 0.005 0.001 0.0050.005 0.0001 0.001 0.001 0.0001 0.0001
nffprime	11
ffprime_\type	B
ffprime_zerobound	.false.
ffprime_wbound	0.2
ff_knot	0.0008 0.0107 0.0194 0.0636 0.1017 0.1480 0.1871 0.4 0.8 0.927 0.979
ff_knot_tune_reg	0.001 0.001 0.001 0.001 0.001 0.0010.001 0.001 0.009 0.009 0.009 0.009
nstab	1
constraint_type	lang_lao
constraint_weight	0.00013
constraint_tuneff	0.5